



Institut für Physik und Astronomie

in Kooperation mit dem

Leibniz-Institut für Astrophysik Potsdam

# Electron kinetic processes in the solar corona and wind

Habilitationsschrift

zur Erlangung des akademischen Grades

doctor rerum naturalium habilitatus
(Dr. rer. nat. habil.)

der Mathematisch-Naturwissenschaftlichen Fakultät
der Universität Potsdam

vorgelegt von

Dr. Christian Vocks

Potsdam, im Mai 2012

This work is licensed under a Creative Commons License:
Attribution - Noncommercial - Share Alike 3.0 Germany
To view a copy of this license visit
http://creativecommons.org/licenses/by-nc-sa/3.0/de/

Published online at the
Institutional Repository of the University of Potsdam:
URL http://opus.kobv.de/ubp/volltexte/2013/6525/
URN urn:nbn:de:kobv:517-opus-65259
http://nbn-resolving.de/urn:nbn:de:kobv:517-opus-65259

**Thesen zur Habilitationsschrift**

*Electron kinetic processes in the solar corona and wind*

**vorgelegt von Dr. Christian Vocks**

- The plasma in the solar corona and wind is characterized by states far away from thermal equilibrium. Solar wind electron velocity distribution functions (VDFs) deviate from simple Maxwellian ones. They show a thermal core, an isotropic halo that can be fitted by power laws, like kappa distributions, and an anti-sunward beam or "strahl".

- A plasma with non-Maxwellian VDFs cannot be described by fluid models. Kinetic models, that provide information on electron VDFs, are necessary.

- Kinetic solar wind models show that some pitch-angle scattering of electrons must occur in order to compensate for the focusing effect of the mirror force due to the interplanetary magnetic field geometry. Otherwise, an extremely narrow strahl would form, that is not supported by the finite strahl widths being observed, e.g. by the Helios satellites or the 3DPlasma/WIND instrument.

- Resonant interaction with whistler waves provides sufficient solar wind electron pitch-angle scattering, based on a wave spectrum in agreement with observed power spectra of interplanetary magnetic field fluctuations.

- A kinetic solar wind model, that includes the effects of Coulomb collisions and whistler waves, is found to reproduce the observed features of solar wind electron VDFs, i.e. core, halo, and strahl.

- Whistler wave scattering is also expected to delay the propagation of solar flare-generated energetic electrons. But velocity-dispersion analyses of energetic electron data from satellites work well under the assumption of free electron propagation.

- The late arrival of flare electrons at Earth due to pitch-angle scattering and the apparent early arrival due to diffusion to lower electron energies just compensate each other.

- The effect of whistler waves on electron VDFs is pitch-angle diffusion in the reference frame of the waves. In a plasma environment with high wave phase speeds, like in the solar corona, whistler waves can lead to electron energy gain, i.e. acceleration.

- Numerical simulations of coronal loop electrons, and a whistler wave spectrum that is the high-frequency tail of a wave spectrum discussed for coronal heating, reveal the formation of power-law suprathermal tails of electron VDFs in the keV energy range.

- This result demonstrates that the processes of coronal heating, solar wind acceleration, and suprathermal electron production are based on a common mechanism.

- Suprathermal electron production can be expected in the atmosphere of any star with a hot corona, and is therefore an important process with respect to solar-stellar connections.

- Electron VDFs derived from observations or kinetic models can be investigated for plasma instabilities by solving the complex dispersion relation.

- The quiet solar corona is capable of emitting whistler waves through the cyclotron maser mechanism, but these waves are absorbed higher up in the solar atmosphere.
- Energetic electrons in a flaring coronal loop can produce whistler waves that are observable from Earth as so-called fiber bursts.

**Populärwissenschaftliches Abstract zur Habilitationsschrift**
*Electron kinetic processes in the solar corona and wind*
**vorgelegt von Dr. Christian Vocks**

Die Sonne ist von einer $10^6$ K heißen Atmosphäre, der Korona, umgeben. Sie ist ebenso wie der Sonnenwind vollständig ionisiert, also ein *Plasma*. Magnetfelder spielen in einem Plasma eine wichtige Rolle, da sie elektrisch geladene Teilchen an ihre Feldlinien binden. EUV-Spektroskope, wie SUMER auf der Raumsonde SOHO, zeigen eine bevorzugte Heizung koronaler Ionen sowie starke Temperaturanisotropien. Geschwindigkeitsverteilung von Elektronen können im Sonnenwind direkt gemessen werden, z.B. mit dem 3DPlasma Instrument auf dem Satelliten WIND. Sie weisen einen thermischen Kern, einen isotropen suprathermischen Halo, sowie einen anti-solaren, magnetfeldparallelen Strahl auf.

Zum Verständnis der physikalischen Prozesse in der Korona wird eine geeignete Beschreibung des Plasms benötigt. Die *Magnetohydrodynamik* (MHD) betrachtet das Plasma einfach als elektrisch leitfähige Flüssigkeit. Mehrflüssigkeitsmodelle behandeln z.B. Protonen und Elektronen als getrennte Fluide. Damit lassen sich viele makroskopische Vorgänge beschreiben. Fluidmodelle basieren aber auf der Annahme eines Plasmas nahe am thermodynamischen Gleichgewicht. Doch die Korona ist weit davon entfernt. Ferner ist es mit Fluidmodellen nicht möglich, Prozesse wie die Wechselwirkung mit elektromagnetischen Wellen mikroskopisch zu beschreiben.

Kinetische Modelle, die Geschwindigkeitsverteilungen beschreiben, haben diese Einschränkungen nicht und sind deshalb geeignet, die oben genannten Messungen zu erklären. Bei den einfachsten Modellen bündelt die Spiegelkraft im interplanetaren Magnetfeld die Elektronen des Sonnenwinds in einen extrem engen Strahl, im Widerspruch zur Beobachtung. Daher muss es einen Streuprozess geben, der dem entgegenwirkt. In der vorliegenden Arbeit wird ein kinetisches Modell für Elektronen in der Korona und im Sonnenwind präsentiert, bei dem die Elektronen durch resonante Wechselwirkung mit Whistler-Wellen gestreut werden.

Das kinetische Modell reproduziert die beobachteten Bestandteile von Elektronenverteilungen im Sonnenwind, d.h. Kern, Halo, und einen Strahl endlicher Breite. Doch es ist nicht nur auf die ruhige Sonne anwendbar. Die Ausbreitung energetischer Elektronen eines solaren Flares wird untersucht und dabei festgestellt, dass Streuung in Ausbreitungsrichtung und Diffusion in Energie die Ankunftszeiten von Flare-Elektronen bei der Erde in etwa gleichem Maße beeinflussen.

Die Wechselwirkung von Elektronen mit Whistlern führt in der Korona nicht nur zu Streuung, sondern auch zur Erzeugung eines suprathermischen Halos, wie er im interplanetaren Raum gemessen wird. Dieser Effekt wird sowohl im Sonnenwind als auch in einem geschlossenen koronalen Magnetfeldbogen untersucht.

**Das Ergebnis ist von fundamentaler Bedeutung für *solar-stellare Beziehungen*. Die ruhige Korona erzeugt stets suprathermische Elektronen. Dieser Prozeß ist eng mit der Koronaheizung verbunden, und daher in jeder heißen stellaren Korona zu erwarten.**

Im zweiten Teil der Arbeit wird beschrieben, wie sich aus der Geschwindigkeitsverteilung der Elektronen die Dämpfung oder Anregung von Plasmawellen berechnen lässt. Die Erzeugung und Ausbreitung von Elektronenzyklotronwellen in der ruhigen Korona und von Whistlern während solarer Flares wird untersucht. Letztere sind als sogenannte *fiber bursts* in dynamischen Radiospektren beobachtbar, und die Ergebnisse stimmen gut mit beobachteten Bursts überein.

# Contents

# Part I

# Kinetic plasma theory

# Chapter 1

# Introduction: Why kinetic models?

## 1.1 The solar atmosphere

The Sun is surrounded by the *corona*, a hot and tenuous atmosphere. The corona is visible during solar eclipses in white light that originates from the Sun's visible surface, the *photosphere*, and is scattered on coronal electrons and dust particles. Due to its high temperature of the order $10^6$ K the coronal emission is mainly in extreme ultraviolet (EUV) light and in soft X-rays. Figure 1.1 shows an image of the solar corona taken by NASA's *Solar Dynamics Observatory* (SDO) in the Fe IX line at 171 Å. A lot of structure is visible, showing density variations that are related to different magnetic field geometries. Both closed loops and "coronal holes" are visible, the latter being regions with lower density where magnetic field lines extend far into interplanetary space.

With this hot corona, the solar atmosphere shows a remarkable thermal structure. The Sun's visible surface, the *photosphere*, has a temperature of 5800 K. The temperature decreases with height within the 500 km thick photosphere and reaches a minimum of about 4000 K that marks the border to the next higher atmospheric layer, the *chromosphere*. The temperature gradually rises inside the 2000 km thick chromosphere up to 8000 K. But then the temperature jumps to the $10^6$ K coronal level across a 100 km thin and highly dynamic transition region.

If one calculates the decrease of coronal pressure with height under the assumption of hydrostatic equilibrium, then this results in the limit of infinite solar distance in a finite pressure, that is several orders of magnitude higher than observed pressures of the interstellar medium. The conclusion is that the solar corona cannot be static. The Sun must drive a continuous flow of plasma, the *solar wind* (Parker, 1958).

The Sun is not as quiet as it appears to be to the unaided eye. Simple white light observations of the Sun already show sunspots. These are regions that appear darker than the surrounding photosphere since strong magnetic fields inhibit the convection of hot gas to the photospheric level. The number of sunspots follows an 11-year cycle with a maximum and a minimum. The magnetic fields that form sunspots extend from the interior of the Sun into the corona. The coronal magnetic field can build up complex structures due to the convective motion of the granulation and supergranulation, especially in the vicinity of complex sunspot groups. Such areas are called *active regions*.

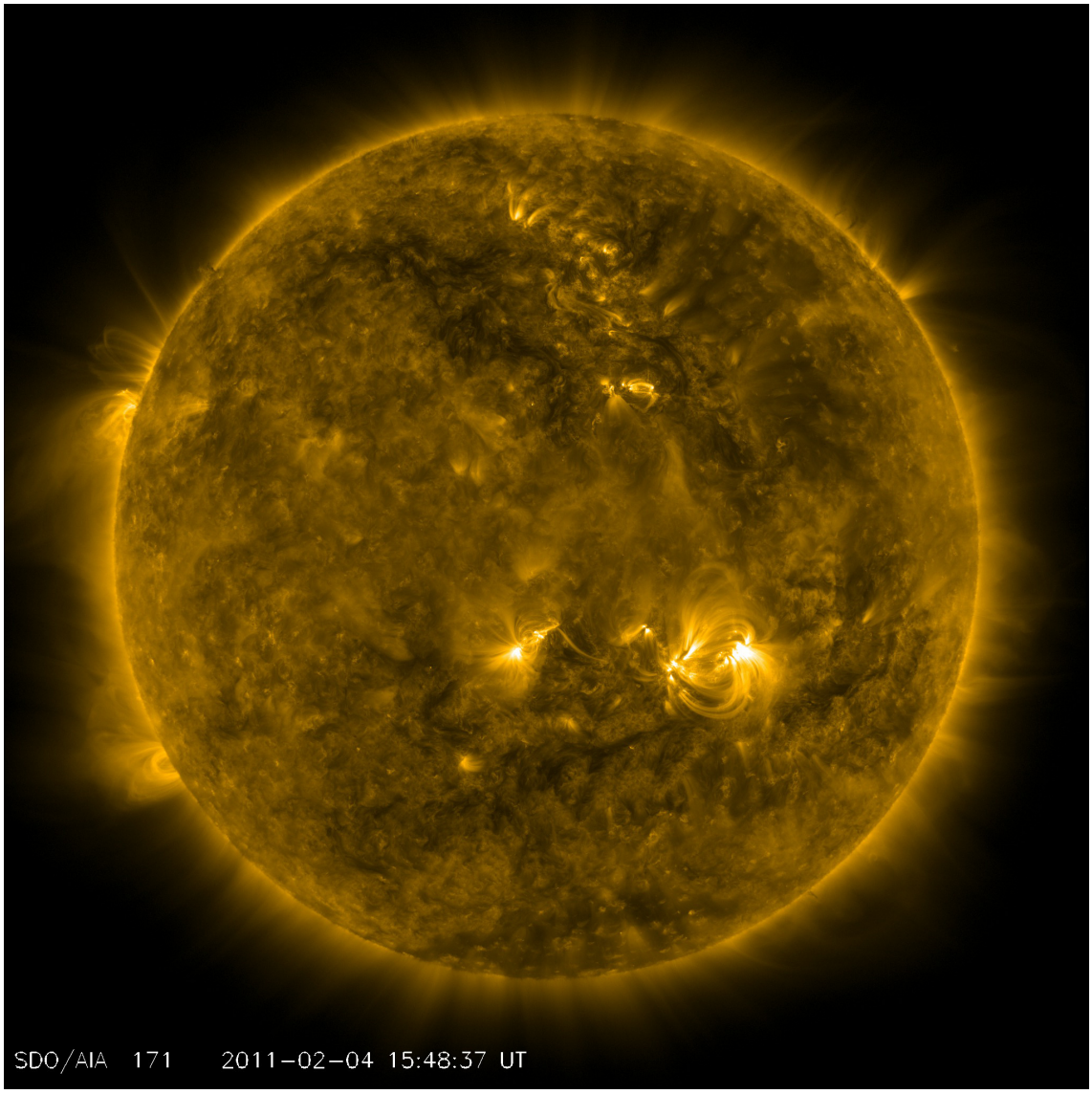


Figure 1.1: The solar corona in the light of the 171 Å Fe IX line as observed by NASA's SDO satellite on 4 February 2011.

In the solar corona, complex magnetic field geometries can become unstable, and *magnetic reconnection* can trigger a reconfiguration of the magnetic field in the corona. This leads to the release of energy stored in the magnetic field. *Flares* and *Coronal Mass Ejections* (CMEs) are both phenomena of such large-scale instabilities in the corona.

Figure 1.2 shows an image of a solar flare in EUV light. Flares extend over a relatively small spatial region and are capable of accelerating electrons and ions to high energies, thus leading to the emission of X- and $\gamma$-rays as well as non-thermal radio radiation (Karlický et al., 2004). CMEs are formed by the release of a large bubble of coronal material into interplanetary space, see (Schwenn, 1986) and (Aurass, 1996) for reviews. Since the coronal magnetic field is frozen into the CME plasma, some magnetic reconnection at the footpoints of the CME is necessary in order to separate the cloud from the Sun.

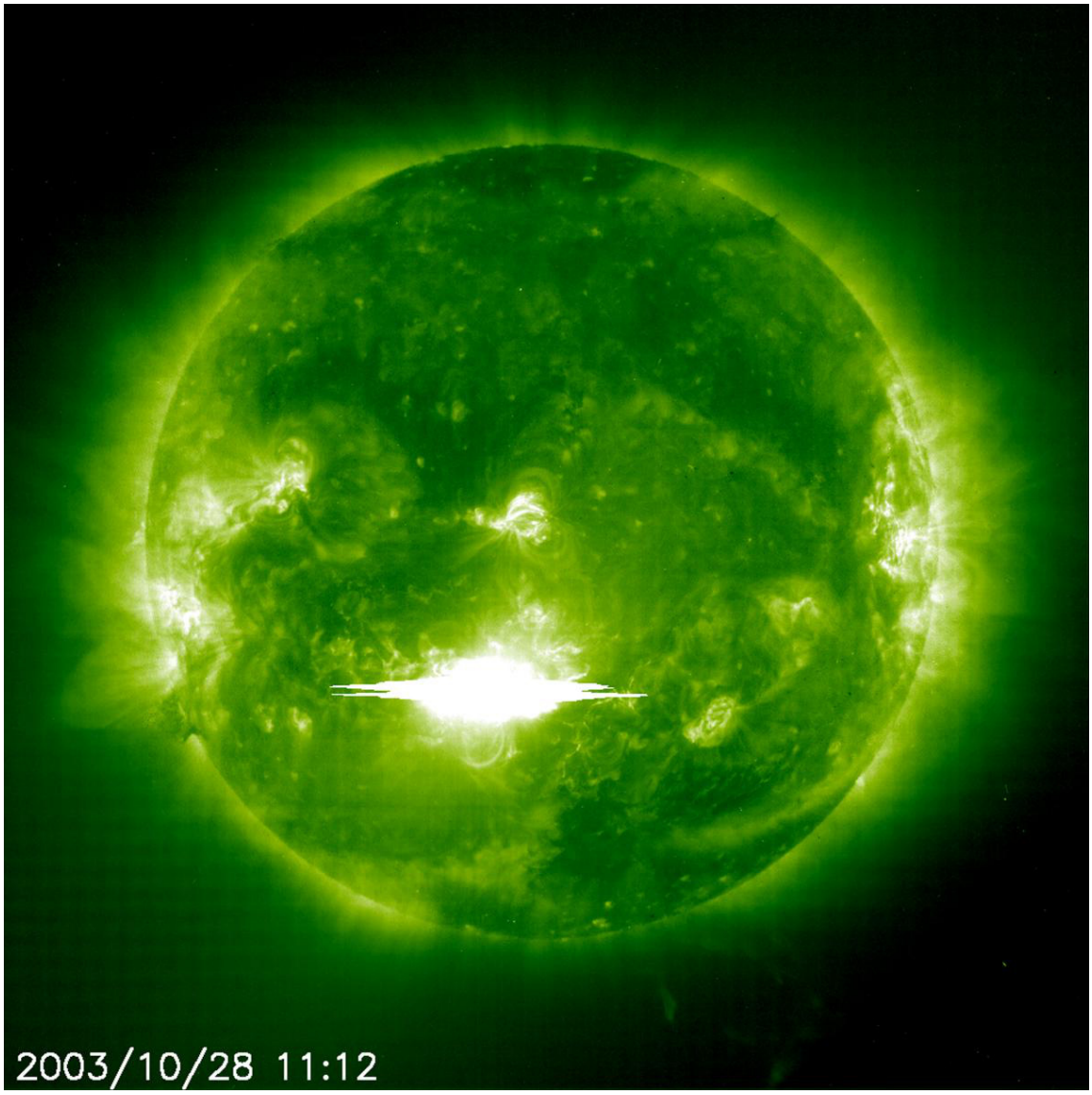


Figure 1.2: Solar flare of 29 October 2003 as observed by the EIT instrument onboard the SOHO satellite in the light of the 195 Å line of Fe XII. (ESA/NASA)

The non-thermal solar radio radiation is classified phenomenologically into different types, with different underlying physical processes, see e.g. (Warmuth & Mann, 2004) as a review. For instance, type II radio radiation is caused by electrons that have been accelerated at shocks (see e.g. (Nelson & Melrose, 1985) and (Mann et al., 1995) as a review), and type III radio bursts by beams of energetic electrons traveling along open magnetic field lines through the corona and, sometimes, penetrating into interplanetary space (see (Suziki & Dulk, 1985) for a review as well as (Lin et al., 1986) for further information).

How can these processes, like coronal heating and solar wind acceleration, or acceleration and propagation of energetic particles, be described? Or, more generally: How to model the physical processes in the solar corona and in interplanetary space? This thesis addresses these question especially for electrons. Both electrons and ions are observed in interplanetary space, but it is energetic electrons that lead to the emission of X-rays and radio waves in the corona and enable

studies of their properties in a remote stellar atmosphere.

The solar corona is fully ionized due to its $10^6$ K temperature. Such a medium is called a *plasma*. The individual particles are coupled through electromagnetic forces. There is a wide variety of plasma models with different degrees of simplification and detail. They can be broadly classified as fluid and kinetic models.

## 1.2 Fluid models for space plasmas

The simplest way to model a plasma is to treat it as an electrically conducting fluid. This approach is called *Magnetohydrodynamics* (MHD). The basic equations of MHD are the continuity equation

$$\frac{\partial n}{\partial t} + \nabla \cdot (n\vec{v}) = 0 \tag{1.1}$$

with full particle density, $n$, and flow speed, $\vec{v}$. It basically states that no particles are created or annihilated. The next equation is the momentum equation

$$nm\frac{\partial \vec{v}}{\partial t} + nm(\vec{v} \cdot \nabla)\vec{v} = -\nabla p + \vec{j} \times \vec{B} + \vec{F} \tag{1.2}$$

with average particle mass $m$ and pressure $p$, current density $\vec{j}$, and magnetic field $\vec{B}$. $\vec{F}$ represents external forces, e.g. gravity. The third equation is the energy equation

$$\frac{\partial p}{\partial t} + (\vec{v} \cdot \nabla)p + \nabla \cdot \left(\frac{5}{3}p\vec{v} + \frac{2}{3}\vec{q}\right) = Q \tag{1.3}$$

with heat flux $\vec{q}$, and a heating term $Q$. It is noteworthy that the continuity equation for the density $n$ introduces the flow speed $\vec{v}$. The momentum equation for $\vec{v}$ introduces the pressure $p$, and the energy equation for $p$ requires the heat flux $\vec{q}$. In order to stop this series of equations, a closure relation has to be introduced. This can be done e.g. by the classical Spitzer-Härm thermal conductivity (Spitzer & Härm, 1953). It is important to note that at this point an assumption enters the fluid description of the plasma:

$$\vec{q} = -\kappa_0 T^{5/2} \nabla T, \qquad \kappa_0 = 10^{-11}\,\mathrm{kg\,m\,s^{-3}\,K^{-7/2}} \tag{1.4}$$

But it is not necessary to describe the plasma as a single fluid. Multi-fluid models treat the different particle species the plasma is composed of, e.g. protons and electrons, as separate fluids with their own densities, velocities, and temperatures. Thus characteristic particle properties, like gyrofrequencies in a magnetic field, can be considered.

Such fluid descriptions of plasmas are widely used for studies of the origin of the solar wind and the physical processes in the solar corona and in interplanetary space. Many models do exist so far, with different degrees of complexity. Examples are two-fluid models, i.e. for protons and electrons, of coronal heating and solar wind acceleration for a given heating function, e.g. (Hansteen & Leer, 1995), three fluid models adding a heavy ion species, $He^{2+}$ or $O^{5+}$, and heating by Alfvén waves (Ofman, 2004), or four-fluid models for both minor ion species and a given

turbulence spectrum (Hu et al., 2000). These models describe the solar wind acceleration from the corona up into interplanetary space. The solar wind origin is also investigated by models that focus on the plasma in coronal funnels, e.g. (Hackenberg et al., 2000; He et al., 2008).

Describing the plasma or its constituent particle species as a fluid is based on the assumption that the electrons or ions show a collective behavior and thus are effectively coupled. Then the whole plasma state is not far away from local thermodynamic equilibrium (LTE), and the velocity distribution functions (VDFs) of all particle species, $j$, are close to Maxwellian ones,

$$f_j(\vec{v}) = \frac{N_j}{(2\pi v_{\mathrm{th},j}^2)^{3/2}} \exp\left(-\frac{|\vec{v} - \vec{v}_{\mathrm{D},j}|^2}{2v_{\mathrm{th},j}^2}\right) \tag{1.5}$$

with particle densities $N_j$, drift speed $\vec{v}_{\mathrm{D},j}$, mass $m_j$ and temperature $T_j$ that leads to a thermal speed $v_{\mathrm{th},j} = \sqrt{k_\mathrm{B} T_j / m_j}$. But are these near-LTE assumptions met for electrons in the solar corona and wind?

| | **Coronal loop** | **Coronal hole** | **Solar wind** |
|---|---|---|---|
| Density | $10^{15}\,\mathrm{m}^{-3}$ | $10^{13}\,\mathrm{m}^{-3}$ | $5 \cdot 10^{6}\,\mathrm{m}^{-3}$ |
| Temperature | $1.4 \cdot 10^{6}\,\mathrm{K}$ | $1.4 \cdot 10^{6}\,\mathrm{K}$ | $1.0 \cdot 10^{5}\,\mathrm{K}$ |
| Magnetic field | 0.01 T (100 G) | $10^{-4}$ T (1 G) | 5 nT |
| Thermal speed, $v_{\mathrm{th,e}}$ | $4600\,\mathrm{km\,s}^{-1}$ | $4600\,\mathrm{km\,s}^{-1}$ | $1200\,\mathrm{km\,s}^{-1}$ |
| Plasma frequency, $\omega_\mathrm{p}$ | $1.8 \cdot 10^{9}\,\mathrm{s}^{-1}$ | $1.8 \cdot 10^{8}\,\mathrm{s}^{-1}$ | $1.3 \cdot 10^{5}\,\mathrm{s}^{-1}$ |
| Electron cycl. freq., $\Omega_\mathrm{e}$ | $1.8 \cdot 10^{8}\,\mathrm{s}^{-1}$ | $1.8 \cdot 10^{7}\,\mathrm{s}^{-1}$ | $880\,\mathrm{s}^{-1}$ |
| Electron mean free path: | | | |
| $L(1\,v_{\mathrm{th}})$ | 817 m | 73 km | $0.81\,R_\odot$ |
| $L(5\,v_{\mathrm{th}})$ | 436 km | $0.06\,R_\odot$ | 2.2 AU |
| $L(20\,\mathrm{keV})$ | $0.1\,R_\odot$ | $9\,R_\odot$ | 335 AU |

Table 1.1: Typical plasma parameters for electrons in the solar corona and wind

Table 1.1 shows typical plasma parameters for electrons in the solar corona and wind. Densities, temperatures, and magnetic fields are given for open and closed coronal magnetic field structures, and for the solar wind near Earth. Electron thermal speeds, plasma frequencies $\omega_\mathrm{p} = \sqrt{N_\mathrm{e}\, e^2/(m_\mathrm{e}\,\epsilon_0)}$, and electron gyrofrequencies $\Omega_\mathrm{e} = e\,B/m_\mathrm{e}$ are also listed. The last part displays collisional mean free paths based on Coulomb collisions of the electrons both with protons and with other electrons. Electrons are collision-dominated if their mean free paths are short as compared to other characteristic length scales. In the solar corona, thermal electrons ($v = 1\,v_{\mathrm{th}}$) have short mean free paths, they are clearly collision dominated. But in interplanetary space the mean free path is almost a solar radius. So solar wind thermal electrons are still influenced by collisions, but not as strongly as in the corona.

This changes for suprathermal electrons ($v = 5\, v_{\mathrm{th}}$). Coulomb collision frequencies approximately scale as $v^{-3}$. The coronal mean free paths are of the order of typical length scales like loop diameters and coronal funnels at the coronal base. So these electrons are borderline collisionless. In interplanetary space, suprathermal electrons are clearly collisionless. The last line of the table shows that energetic electrons are collisionless even in the corona.

## 1.3 Solar wind observations

Due to the collisionless nature of space plasmas it is no surprise that spacecraft observations of solar wind particle velocity distribution functions (VDFs) reveal strong deviations from simple Maxwellian VDFs. Helios data of solar wind protons (Marsch, 2006) show temperature anisotropies and non-Maxwellian VDFs shaped in a way that is in agreement with expectations from resonant interaction with ion cyclotron waves. In the solar corona, strong temperature anisotropies and preferential heating of heavy ions is found (Kohl et al., 1998) despite the higher density there. This has motivated Vocks (2002) and Vocks & Marsch (2002) to study the coronal heating process with a kinetic model for ions that includes the effects of Coulomb collisions and resonant interaction with ion cyclotron waves. The model indeed finds preferred heating of heavy ions.

Solar wind electron VDFs also show distinct deviations from Maxwellian distributions, with a thermal core, an isotropic halo of suprathermal electrons, and a magnetic-field aligned beam or "strahl" that is usually directed away from the Sun (Lin, 1974; Pilipp et al., 1987). Figure 1.3 shows isolines of solar wind electron VDFs as observed by EESA-Low (EESAL), one of the electron electrostatic analyzers of the 3DP experiment (Lin et al., 1995) onboard the WIND spacecraft. EESAL measures full 3D electron VDFs with a pitch-angle resolution of 22 degrees. The isolines have been chosen in such a way that they would form equidistant circles for a Maxwellian VDF. The plots cover the energy range up to 1 keV. At higher energies, the VDFs become isotropic.

The four plots differ in detail due to slightly different solar wind conditions, but they share the same basic characteristics. In all of them the thermal core and the extended halo are clearly visible. The strahl can be identified as a distinctive anisotropic feature. This beam is limited to energies below approximately 1 keV, and it shows a finite width well above the instrumental angular resolution.

These observations demonstrate that the core assumption of fluid models, a state close to local thermodynamic equilibrium, is not fulfilled in the corona and in interplanetary space.

## 1.4 Kinetic models

The observed non-Maxwellian distributions, their origin and their role in coronal heating and solar wind acceleration are beyond the scope of fluid models. Kinetic models are necessary to describe the microphysics of these processes. Kinetic models are based on VDFs, i.e. the phase-space densities, $f(\vec{r}, \vec{v}, t)$ of the particle species under study. The assumption of a certain shape of the VDF, e.g. being close to a Maxwellian as in fluid models, is not needed anymore. This enables them to describe states far away from LTE.

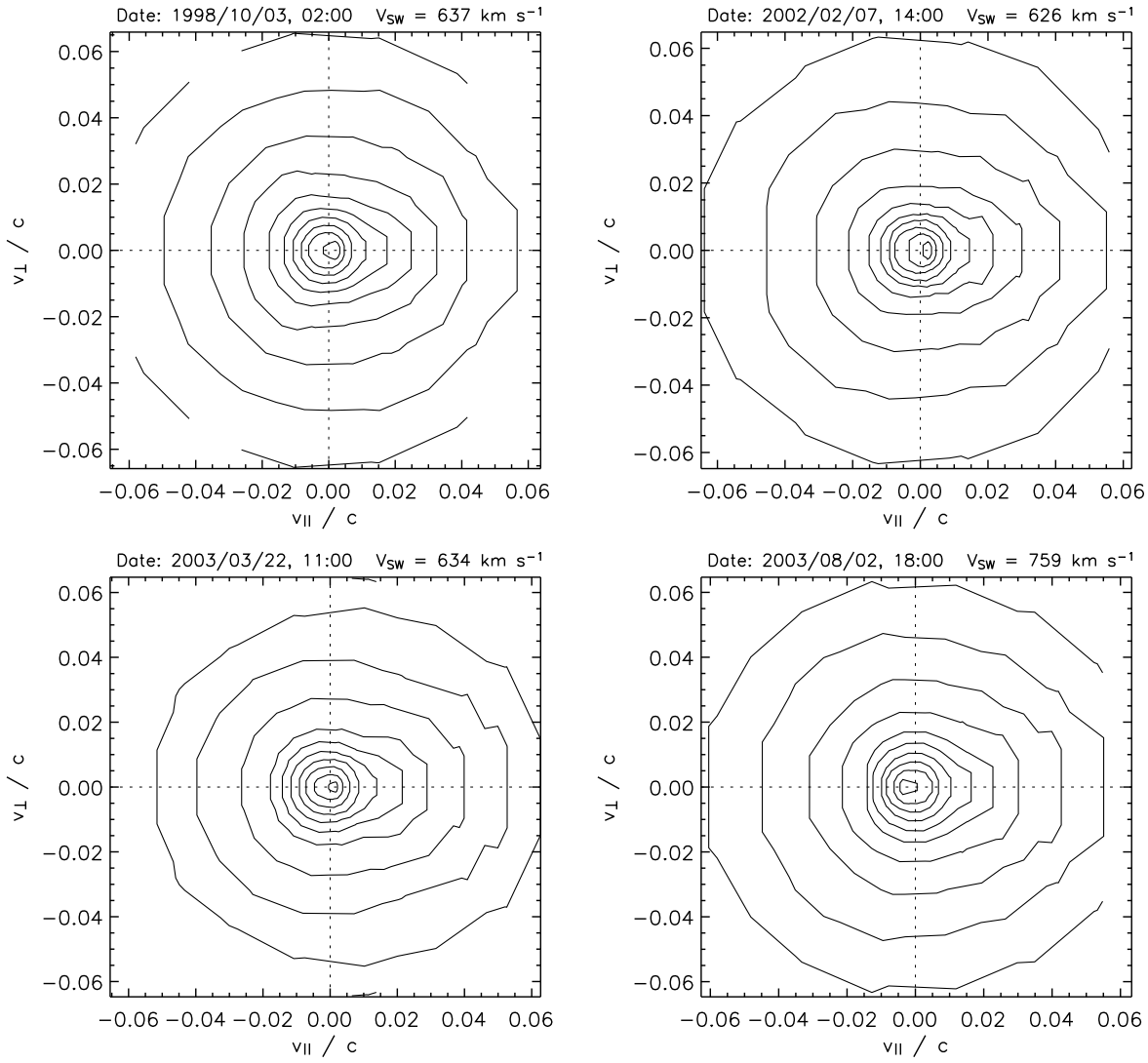


Figure 1.3: Isolines of the electron VDF as observed by *WIND* 3DP at four different dates in the fast solar wind. The dates and solar wind speeds ($v_{SW}$) are indicated in the plots. From (Vocks et al., 2005).

But a price has to be paid for the kinetic description of a plasma: While fluid models depend only on up to three spatial coordinates, kinetic models additionally introduce up to three velocity coordinates to describe particle VDFs. This leads to considerably higher computer costs. Furthermore, boundary conditions have to be defined at all bounds of the simulation box, not only for spatial but also for velocity coordinates.

The basic equation of kinetic theory for space plasmas is the Vlasov equation, that reads for electrons:

$$\frac{\mathrm{d}f}{\mathrm{d}t} = \frac{\partial f}{\partial t} + (\vec{v}\cdot\nabla)f + \left[m_e\gamma_L\vec{g} - e(\vec{E}+\vec{v}\times\vec{B})\right]\cdot\frac{\partial f}{\partial\vec{p}} = 0. \tag{1.6}$$

It is presented here in relativistic form, since flare-generated energetic electrons with energies up to hundreds of keV require a relativistic treatment. The velocity coordinates, $\vec{v}$, are replaced by

momentum coordinates, $\vec{p}$. $\vec{g}$ and $\vec{E}$ represent the gravitational and electric field, respectively. In space plasmas, $\vec{E}$ normally corresponds to the charge-separation electric field that ensures quasi-neutrality of the solar corona against different gravitational scale heights of protons and electrons. $\vec{B}$ is the background magnetic field, $\gamma_L = \sqrt{1 + p^2/(m_e c)^2}$ the Lorentz factor, and $m_e$ the electron rest mass. The Vlasov equation basically states that the number of electrons in a given phase-space volume element does not change while this volume element is evolving in time.

If a diffusion process is present that scatters electrons in and out of the phase-space element, then the Vlasov equations turns into the Boltzmann-Vlasov equation, a Fokker-Planck type equation with a diffusion term on the right hand side:

$$\frac{\mathrm{d}f}{\mathrm{d}t} = \left(\frac{\partial f}{\partial t}\right)_{\mathrm{diff}} \tag{1.7}$$

One scattering mechanism is Coulomb collisions between electrons and both protons and other electrons, since thermal electrons are not entirely collision-free, see Table 1.1. Another very important mechanism is the resonant interaction of electrons with plasma waves. It leads to strong scattering and diffusion, as will be demonstrated in the next chapter.

# Chapter 2

# Kinetic solar wind models

Generally, a kinetic solar wind model is based on the solution of a Boltzmann-Vlasov equation (1.7), that describes the temporal evolution of a VDF $f(\vec{r}, \vec{p}, t)$ in the solar corona and in interplanetary space. The complexity of the kinetic model depends on what physical effects are considered in the term on the right hand side of the equation. The following presentation of models follows largely the review of Vocks (2011).

## 2.1 Exospheric models

The simplest kinetic models are exospheric models (Jockers, 1970; Lie-Svendsen et al., 1997) that are based on the assumption that electrons are collisionless above a certain height in the solar atmosphere, called the exobase. Then, solar wind electron VDFs are just described by the Vlasov equation (1.6).

In such a model, suprathermal electrons in the corona exceed the local escape velocity, $v_{\mathrm{esc}}$, from the Sun's combined gravitational and electrostatic potential. Thus, they move into interplanetary space, leading to the formation of a strahl-like structure. However, these electrons escape from the Sun and do not return. So for negative velocities parallel to the magnetic field, $v_{\parallel} < -v_{\mathrm{esc}}$, the VDF becomes $f = 0$ with a sharp cutoff, as illustrated in Fig. 2.1. The inclusion of Coulomb collisions (Lie-Svendsen et al., 1997) results in more realistic electron VDFs with a thermal core and an anisotropic halo resembling the strahl (Pierrard et al., 2001), as well as an improved description of solar wind acceleration (Landi and Pantellini, 2003). But the steep phase-space gradient at $v_{\parallel} < -v_{\mathrm{esc}}$ remains, and no isotropic suprathermal halo as it is observed (Fig. 1.3) can be formed.

It is noteworthy that even for such simple models it is not sufficient to study the electron VDF alone. The Vlasov equation (1.6) depends on the gravitational, electric and magnetic fields, $\vec{g}$, $\vec{E}$, and $\vec{B}$, respectively. $\vec{g}$ just depends on the solar distance and $\vec{B}$ is determined by the magnetic field geometry, e.g. the Parker spiral. But $\vec{E}$ needs to be provided. Since the electrons are guided by the magnetic field lines around which they gyrate, it is sufficient to consider only the electric field component $E_{\parallel}$ parallel to $\vec{B}$.

This field component is the charge-separation electric field that enforces equal scale heights for electrons and positive ions in the solar corona and wind, so that the quasi-neutrality condition of

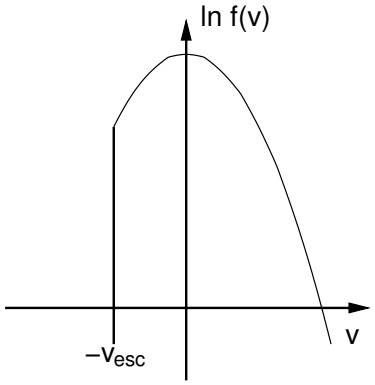


Figure 2.1: Sketch of the electron VDF in an exospheric model.

equal negative and positive charge densities in the plasma is fulfilled everywhere. Any spatial concentration of charges leads to a strong electric field that drives it away immediately. Such an electrostatic fluctuation is called *Langmuir oscillation*, and its frequency is the plasma frequency $\omega_\mathrm{p}$ that is listed in Table 1.1.

The electric field $E_\parallel$ can readily be derived from the electron fluid momentum equation (1.2):

$$N_\mathrm{e} m_\mathrm{e} \frac{\mathrm{d}\vec{v}_\mathrm{e}}{\mathrm{d}t} = -\nabla p_\mathrm{e} - N_\mathrm{e}\, e\, E_\parallel + N_\mathrm{e}\, m_\mathrm{e}\, \vec{g} \tag{2.1}$$

Since the electron mass is much smaller than the proton mass, inertial effects can be neglected for the electrons, effectively setting $m_\mathrm{e} = 0$ in the equation above. The result is:

$$E_\parallel = -\frac{1}{N_\mathrm{e}\, e} \nabla p_\mathrm{e} \tag{2.2}$$

The potential difference between the low corona and near-Earth interplanetary space is model-dependent, but typically of the order 1 kV. $E_\parallel$ only depends on the local electron density and pressure gradient. But by means of quasi-neutrality, $N_\mathrm{e}$ is coupled to the ion density. Therefore it is not possible to have an electron-only kinetic model for the solar wind. A background model that includes ion dynamics is needed. The inclusion of Coulomb collisions also requires knowledge of the collision partners, which are not only electrons but also ions.

## 2.2 Suprathermal electrons

The lack of electrons returning to the Sun, that manifests itself as low phase-space densities for $v_\parallel < -v_\mathrm{esc}$ in exospheric models, is in strong contrast to the observations of an isotropic suprathermal halo distribution. However, these exospheric models are based on Maxwellian electron VDFs in the corona. Observed solar wind VDFs can be fitted by two Maxwellians for the core and halo. But the observations indicate higher phase-space densities for suprathermal energies above approximately $5\, v_\mathrm{th}$ than the halo fit provides. A better fit can be obtained with a single kappa distribution (Maksimovic et al., 1997)

$$f_\kappa(p) = N_\mathrm{e} \frac{\Gamma(\kappa+1)}{\pi^{3/2}(2\kappa-3)^{3/2} p_\mathrm{th}^3 \Gamma(\kappa-1/2)} \left(1 + \frac{p^2}{(2\kappa-3)p_\mathrm{th}^2}\right)^{-(\kappa+1)} \tag{2.3}$$

with a "thermal momentum", $p_{\rm th} = \sqrt{m_e k_B T}$. This kappa distribution has power-law suprathermal tails $\propto p^{-2(\kappa+1)}$. Such a fit can be further improved by a Maxwellian core and a kappa halo (Nieves-Chinchilla and Viñas, 2008). The presence of suprathermal tails of solar wind electron VDFs leads to the question where the electrons are accelerated. This does not have to happen in interplanetary space. By calculating the VDF evolution back to the solar corona it is possible to show that a coronal origin of the suprathermal tails is possible (Pierrard et al., 1999). Such non-Maxwellian coronal electron VDFs have the interesting consequence that non-local effects can become important, like velocity filtration (Scudder, 1992a,b), and heat fluxes different from the classical Spitzer-Härm law, even against a temperature gradient (Dorelli & Scudder, 2003).

Exospheric models with kappa distributions yield more realistic results (Zouganelis et al., 2004) than models based on Maxwellian VDFs, with higher solar wind speeds and electron temperatures closer to observations. But also in these models the problem remains that no electrons with speeds faster than the escape velocity can return to the Sun, so that still $f(v_\parallel < -v_{\rm esc}) \to 0$.

## 2.3 Electron scattering by whistler waves

This remains in contrast to observations that indicate not only an anisotropic strahl, but also an isotropic halo. Furthermore, the interplanetary magnetic field is not homogeneous. It decreases with solar distance in the opening field structure of the Parker spiral approximately as $B \propto r^{-2}$. For an electron that moves through such a magnetic field both the kinetic energy, $m_{\rm e}(v_\parallel^2 + v_\perp^2)/2$, and the magnetic moment, $m_{\rm e} v_\perp^2/(2B)$, are conserved. As $B$ decreases, $v_\perp$ must also decrease, and $v_\parallel$ increase. So this "mirror force" would focus all anti-sunward moving electrons into an extremely narrow beam. Figure 2.2 shows this beam in the kinetic solar wind model of Vocks & Mann (2003) that included Coulomb collisions as the only scattering mechanism for electrons leaving the Sun. The width of this beam is limited by the grid resolution of the numerical model.

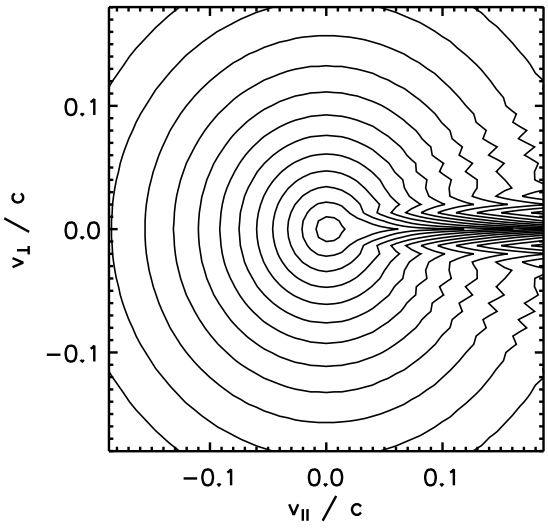


Figure 2.2: Isolines of the electron VDF at a solar distance of 1 AU in the kinetic model of Vocks & Mann (2003).

Such a narrow beam is not supported by observations of finite strahl widths (Hammond et al., 1996) and of an isotropic halo. So some mechanism must exist that scatters electrons back towards the Sun, against the mirror force. Owens et al. (2008) have determined the amount of scattering that is needed from Ulysses observations. Coulomb collisions are too inefficient in interplanetary space, solar wind suprathermal electrons are collision-free.

A promising candidate for this mechanism is electron scattering by electromagnetic waves. Interplanetary space is not a vacuum, but filled with a spectrum of electromagnetic fluctuations (Salem, 2000; Mangeney et al., 2001). The cyclotron resonant interaction with plasma waves can be described within the framework of quasilinear theory (Kennel and Engelmann, 1966). Linear theory describes small fluctuations of electromagnetic fields, $\vec{E}_1$, and electron VDFs, $f_1$ that change in time harmonically as $\sin(\omega t)$. It neglects terms of higher order in these fluctuations. Quasilinear theory also considers quadratic terms $\vec{E}_1 f_1$, that change in time as $\sin(\omega t)^2$, and whose temporal average does not vanish. So quasilinear theory, unlike linear theory, describes the long-term evolution of electron VDFs due to wave action, but is not fully self-consistent with a prescribed dispersion and being evaluated in the zero wave growth rate limit.

The simplifying assumption of wave propagation parallel to the background magnetic field is made, since a complicated integral in wave-vector space would occur otherwise (Marsch & Tu, 2001). The resulting diffusion equation can be written in the coordinates momentum, $p$, and pitch-angle, $\theta$:

$$\left(\frac{\partial f}{\partial t}\right)_{\mathrm{w}} = \frac{1}{p^2 \sin\theta}\left[\frac{\partial}{\partial p}\left(\alpha_{pp}\frac{\partial f}{\partial p} + \alpha_{p\theta}\frac{\partial f}{\partial \theta}\right) + \frac{\partial}{\partial \theta}\left(\alpha_{\theta p}\frac{\partial f}{\partial p} + \alpha_{\theta\theta}\frac{\partial f}{\partial \theta}\right)\right] \tag{2.4}$$

Marsch (1998) provides the quasilinear diffusion coefficients as

$$\begin{aligned} \alpha_{pp} &= \tfrac{1}{\tau} p^2 \sin^3\theta\, v_{\mathrm{ph}}^2 \\ \alpha_{p\theta} = \alpha_{\theta p} &= \tfrac{1}{\tau} p \sin^2\theta\, v_{\mathrm{ph}} (v_{\mathrm{ph}} \cos\theta - v) \ , \\ \alpha_{\theta\theta} &= \tfrac{1}{\tau} \sin\theta\, (v_{\mathrm{ph}} \cos\theta - v)^2 \end{aligned} \tag{2.5}$$

with wave phase speed, $v_{\mathrm{ph}}$, electron speed, $v = p/(m_e\gamma)$, and "collision frequency" associated with the wave-electron interaction:

$$\frac{1}{\tau} = \frac{\pi}{4}\Omega_{\mathrm{e}}^2 \left|\frac{v_{ph} - v\,\cos\theta}{v_{ph}}\right| \hat{\mathcal{B}}_\omega \tag{2.6}$$

$\hat{\mathcal{B}}_\omega$ is the wave spectral energy density at the frequency $\omega$, normalized to the magnetic field energy density, $B^2/(2\mu_0)$, and $\Omega_{\mathrm{e}}$ is the electron cyclotron frequency, $\Omega_{\mathrm{e}} = eB/m_e$.

The frequency of a wave that interacts with an electron with given momentum $(p, \theta)$ is determined by the resonance condition. It reads for whistler waves, that are right-hand polarized:

$$\omega - k_{\|} p_{\|} /(m_e\gamma) = \Omega_{\mathrm{e}}/\gamma. \tag{2.7}$$

$p_{\|} = p\,\cos\theta$ is the momentum component parallel to the background magnetic field, and $k_{\|}$ is the parallel wave vector component. The resonance condition basically states that the electron's gyrofrequency equals the Doppler-shifted wave frequency in the electron frame. Interaction with left-hand polarized waves, i.e. proton cyclotron waves, is not relevant here, since this resonance

condition reads $-\Omega_e$ on the right hand side and can only be fulfilled if the electron speed $v_\parallel$ exceeds the wave phase speed by a factor that is larger than the proton-electron mass ratio. The resonance frequencies are thus very close to the proton cyclotron frequency where wave phase speeds are small. But these waves are strongly damped by protons. Resonance frequencies down in the MHD range are only reached for electrons with much higher energies than discussed here.

Whistler or electron cyclotron waves are right-hand polarized waves with dispersion relation

$$\left(\frac{c}{v_{ph}}\right)^2 = 1 + \frac{\omega_p^2/\Omega_e^2}{(m_e/m_p + \omega/\Omega_e)(1 - \omega/\Omega_e)}. \tag{2.8}$$

$\omega_p = \sqrt{N_e\, e^2/(m_e\, \epsilon_0)}$ is the plasma frequency. It can be replaced by the electron Alfvén speed, $v_{A,e} = B/\sqrt{N_e\, m_e\, \mu_0}$, using the identity $\omega_p^2/\Omega_e^2 = (c/v_{A,e})^2$. The electron Alfvén speed can be used as a rough estimate for the whistler wave phase speed, that reaches its maximum value, $v_{ph,max} \approx 0.5\, v_A$, at the frequency $\omega = 0.5\, \Omega_e$.

The main effect of resonant electron - whistler interaction is pitch-angle scattering of the electrons in the reference frame of the waves, leading to the formation of "kinetic shells" as in the solar wind model of Isenberg et al. (2001) who studied the interaction of protons with proton cyclotron waves.

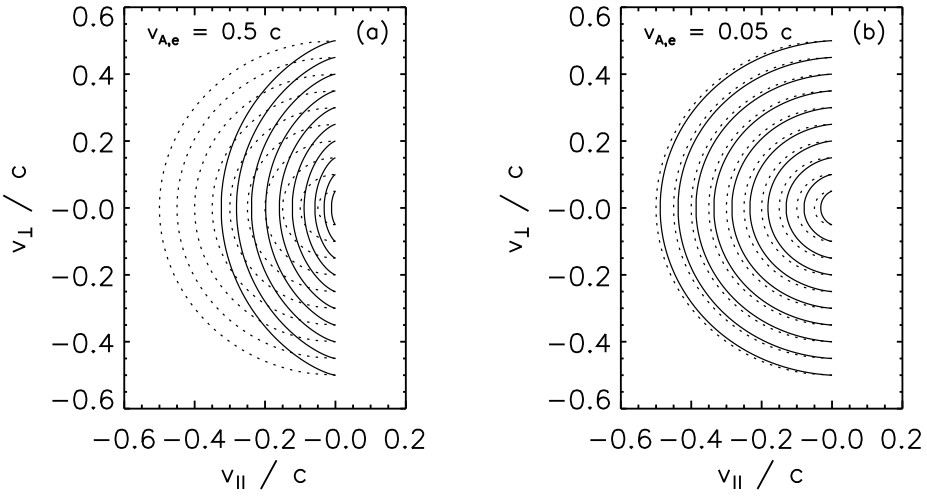


Figure 2.3: Kinetic shells for electrons in plasmas with different electron Alfvén speeds (solid lines). Isolines for a Maxwellian VDF are shown for comparison (dotted lines).

Figure 2.3 shows the kinetic shells for (a) high and (b) low electron Alfvén speeds. The waves propagate away from the Sun, so only the half-space $v_\parallel < 0$ can interact with them. For non-dispersive waves with frequency-independent phase speeds, the kinetic shells would just be concentric circles around $(v_\parallel = v_{ph}, v_\perp = 0)$. Because of the dispersion relation (2.8) they deviate from such a simple geometry. Consequently, the resonant interaction with whistler waves tends to deform the isolines of the electron VDF in such a way that they would coincide with the resonance shells. To demonstrate the effect of the waves, the isolines of an undisturbed Maxwellian VDF are also plotted as dotted lines in Figure 2.3.

High wave phase speeds, (a), are found in the solar corona. The wave-electron interaction aims at creating an electron VDF that deviates significantly from a Maxwellian. The solar wind corresponds to the case of low wave phase speeds, (b). Due to the small difference between wave and plasma reference frames the resonant interaction with whistlers mainly leads to pitch-angle scattering of the electrons.

Since the whistler wave dispersion relation (2.8) only allows wave propagation for frequencies below the local electron cyclotron frequency, $\omega < \Omega_e$, it follows from the resonance condition (2.7) that electrons and waves must propagate into opposite directions, $k_\parallel p_\parallel < 0$. This requires the existence of sunward-propagating whistler waves in order to scatter electrons, that are moving away from the Sun, against the mirror force into an isotropic halo.

## 2.4 Kinetic solar wind model with whistler waves

Vocks & Mann (2003) have introduced resonant interaction with whistler waves into a kinetic model for electrons in the solar corona and wind. The focus of the paper was on whistler waves propagating away from the sun and their influence on coronal electron VDFs. Such a wave spectrum and its effects will be discussed in chapter 4.3. Due to the lack of sunward-propagating whistlers, this model did not provide any electron scattering out of the strahl in interplanetary space. So it developed the extremely narrow beam depicted in Fig. 2.2.

Vocks et al. (2005) then improved the model substantially by adding a whistler wave spectrum based on observational data of interplanetary space turbulence. Since this spectrum contains waves propagating both away from and towards the Sun, the new model did provide pitch-angle scattering of all electrons in the solar wind. The source of the wave spectrum is assumed to be a turbulent cascade. This is a highly nonlinear process beyond the scope of the kinetic model presented here. Furthermore, the observed wave spectrum shows little temporal variation. Therefore, the wave spectrum is assumed to be constant in time.

### 2.4.1 Interplanetary whistler wave spectrum

Wave generation by a turbulent cascade will produce waves that propagate in all directions, not only parallel to the background magnetic field, $\vec{B}$. Observations and models indicate the existence of oblique waves in the solar wind, see e.g. (Matthaeus et al., 1990) or (Leamon et al., 1998). But the diffusion equation (2.4) applies only to waves that propagate parallel to $\vec{B}$. However, the inclusion of obliquely propagating waves would greatly complicate the diffusion equation (Marsch, 2001) and preclude a numerical solution. On the other hand, the basic effects of quasilinear wave-electron interaction, i.e. pitch-angle diffusion, are found by a model that only includes waves propagating parallel to $\vec{B}$. Furthermore, Bieber et al. (1994) have found that parallel waves do most of the scattering of energetic particles, and that highly oblique waves contribute very little to it. Thus, the exclusive consideration of whistlers propagating parallel to $\vec{B}$ is a strong, but not a too strong model assumption.

The first step in defining the spectrum of sunward propagating whistlers is finding the overall wave spectrum in interplanetary space. As a reference, the global spectrum of solar wind elec-

tromagnetic fluctuations for frequencies from $10^{-6}$ Hz up to $10^{5}$ Hz of Salem (2000) is used. It is a collection of data from different instruments onboard the WIND spacecraft (Mangeney et al., 2001). This frequency interval covers fluctuations from the MHD range up to electron cyclotron waves.

These data have been gathered at a solar distance of 1 AU. Since a useful simulation box for the kinetic model extends from the solar corona far into interplanetary space, it is necessary to model the variation of the wave spectrum as a function of distance from the Sun. Based on the assumption that the mechanism that generates the waves does not change significantly with solar distance, a non-dimensional spectral function, $B^*_\omega(x)$, with $x = \omega/\Omega_e$, is introduced. $B^*_\omega(x)$ does not change within the simulation box. The spectral wave power can then be calculated as:

$$B_\omega = \frac{B^2}{2\mu_0}\frac{1}{\Omega_\mathrm{e}}B^*_\omega(\omega/\Omega_\mathrm{e}) \tag{2.9}$$

The best fit to the solar wind measurements in Salem (2000) is achieved with

$$B^*_\omega(x) = 1.5 \cdot 10^{-9} x^{-2.6} \tag{2.10}$$

The wave spectrum is found to be very steep with a spectral coefficient of -2.6. For the average solar wind conditions in Salem (2000) with a magnetic field $B = 5.25$ nT at 1 AU, the combination of Eqs. (2.9) and (2.10) results in:

$$B_\omega = 1.1 \cdot 10^{-22}\left(\frac{\omega}{\Omega_\mathrm{e}}\right)^{-2.6} \mathrm{J\,m^{-3}\,s} \tag{2.11}$$

For a frequency that is a fixed fraction $x$ of the local electron gyrofrequency, the spectral wave power as defined in Eq. (2.9) varies proportional to the magnetic field, as $B$ changes with distance from the Sun, $s$. But such a dependency of the wave power on $B$ leads to an unrealistic increase of the power towards the solar corona, and a too strong decrease at solar distances beyond 1 AU.

In order to reconcile the wave spectrum, Eq. (2.9) with observations and models of waves in the solar wind, another factor depending on the electron number density, $N_\mathrm{e}$, is introduced:

$$B_\omega = \frac{B(s)^2}{2\mu_0}\frac{1}{\Omega_\mathrm{e}(s)}\frac{N_\mathrm{e}(1\,\mathrm{AU})}{N_\mathrm{e}(s)}B^*_\omega(\omega/\Omega_\mathrm{e}(s)) \tag{2.12}$$

This assumption seems to be somewhat arbitrary. However it is not the objective of this analysis to provide an accurate theory on the physics of wave generation in interplanetary space. The variation of the wave spectrum with distance from the Sun as it is described by Eq. (2.12) is in good agreement with both the model results and Helios data that are presented by Hu et al. (1999) and the Ulysses observations of N. Lin et al. (1998), so this model spectrum is appropriate for a kinetic study of electron diffusion in interplanetary space.

The equation (2.12) describes the total wave power $B_\omega$ as it is observed in interplanetary space. It contains contributions from many wave modes propagating in all directions. But only whistler waves propagating towards the Sun ($k_\parallel < 0$) can fulfill the resonance condition, Eq. (2.7), with electrons that move away from the Sun ($v_\parallel > 0$).

It is reasonable to assume that at small frequencies only a minor fraction, that is chosen to be 1%, of the total wave power at a given frequency, can be assigned to sunward propagating whistler waves. The rest can be in other wave modes, propagating parallel or perpendicular to the background magnetic field, or obliquely to $\vec{B}$.

This is different for frequencies above the lower hybrid frequency, $\omega_{\rm LH} = \sqrt{\Omega_{\rm p}\Omega_{\rm e}}$, with $\Omega_{\rm p}$ being the proton cyclotron frequency. Since the plasma frequency, $\omega_{\rm p}$, is much higher than the electron cyclotron frequency in the solar corona and wind, no wave mode can propagate perpendicular to the background magnetic field in the frequency interval $\omega_{\rm LH} < \omega < \Omega_{\rm e}$. Only electron cyclotron / whistler waves can propagate parallel to $\vec{B}$ at these frequencies. Thus the contribution of sunward propagating whistler waves to the total wave power can increase up to 50%, with the other 50% provided by anti-sunward propagating whistlers. In order to avoid numerical problems with a discontinuous change of the contribution, a smooth transition is set up.

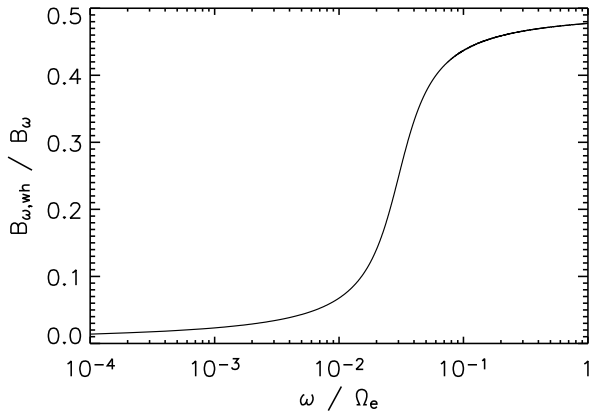


Figure 2.4: Contribution of sunward propagating whistler waves to the total wave power in interplanetary space as function of the wave frequency, $\omega$, normalized to the electron cyclotron frequency, $\Omega_{\rm e}$.

Figure 2.4 shows the fraction $B_{\omega,\rm wh}/B_\omega$ of the total wave power that is assigned to sunward propagating whistler waves as a function of frequency. At low frequencies, this fraction is of the order of 1% and increases rapidly at the lower hybrid frequency, $\omega_{\rm LH} = 0.023\,\Omega_{\rm e}$, towards values up to 50%.

In the kinetic calculations, the wave power of both the sunward and anti-sunward propagating whistlers is defined as the fraction of the total wave power (2.12) that is displayed in Fig. 2.4. This whistler wave power is used to determine the "collision frequency" $1/\tau$ in Eq. (2.6) and to evaluate the electron diffusion term, Eq. (2.4).

### 2.4.2 Proton-electron solar wind background model

It has been pointed out in Sect. 2.1 that determining the charge-separation electric field $E_\parallel$ requires a background model that includes ion dynamics. This is also true for calculating the electron-whistler interaction, Eq. (2.4), that is based on the wave phase speed, $v_{\rm ph}$ from Eq. (2.8). The

phase speed depends on the electron density through the plasma frequency or electron Alfvén speed, and is connected to the ion density through the quasi-neutrality of the plasma. For Coulomb collisions it is also necessary to know the densities and temperatures of the collision partners. In an electron-proton plasma this is both electrons and protons.

Therefore, a background model including the ions is needed for the electron kinetic model. Since the characteristic time-scales of protons and electrons differ by three orders of magnitude due to their mass ratio, the protons cannot be treated kinetically in the same model. Instead, a fluid model is used to describe the background plasma conditions in the solar corona and wind. This model also enables the definition of initial and boundary conditions for the electron VDF.

The background solar wind model is a 2-fluid model for protons and electrons. It is a combination of two models. Densities and flow speeds are calculated by the same method as in the classical solar wind model of Parker (1958). Note that the quasineutrality and zero current conditions in the plasma require equal number densities and flow speeds of both protons and electrons. But in contrast to Parker's isothermal solar wind model, given profiles of proton and electron temperatures, $T_\mathrm{p}(s)$ and $T_\mathrm{e}(s)$, and the magnetic flux tube cross sectional area, $A(s)$, can be handled here. The spatial coordinate $s$ represents the direction along the flux tube under consideration. The plasma wave pressure is also taken into account. To calculate the proton and electron temperature profiles, the energy equations of Hackenberg et al. (2000) are used. They include energy exchange between the particle species due to Coulomb collisions, radiative cooling of the electrons, and heat fluxes. The protons are heated by resonant absorption of proton cyclotron waves that enter the simulation box with a given power law spectrum and propagate anti-sunwards.

To yield a solution that satisfies both the Parker-type model and the energy equation, an iterative method is employed. Initially, the Parker-type model is used to generate profiles for the particle number densities, $N(s)$, and flow speeds, $v_\mathrm{d}(s)$ for an isothermal initial temperature profile, $T_\mathrm{p}(s) = T_\mathrm{e}(s) \equiv T_0$, that is set to a typical coronal value of $T_0 = 10^6\,\mathrm{K}$. Then, the energy equations for protons and electrons are solved with these profiles of $N(s)$ and $v_\mathrm{d}(s)$, resulting in new temperature profiles $T_\mathrm{p}(s)$, $T_\mathrm{e}(s)$ for the protons and electrons, respectively. In the next step of the iteration, $N(s)$ and $v_\mathrm{d}(s)$ are recalculated with the Parker-type model that has been fed with the new temperature profiles. Then, the energy equation is solved again with the resulting new $N(s)$ and $v_\mathrm{d}(s)$, yielding new temperature profiles. Then the Parker-type model is utilized again, and so forth. This method is iterated until the profiles for $N(s)$, $v_\mathrm{d}(s)$, and the temperature profiles do not change any more with the iteration steps. This method returns profiles $N(s)$, $v_\mathrm{d}(s)$, $T_\mathrm{p}(s)$, and $T_\mathrm{e}(s)$ that solve both the energy equations for protons and electrons, and the continuity and momentum equations on which the Parker-type model is based on.

Figure 2.5 shows model results for the fast solar wind. The magnetic field geometry considered here is a coronal funnel that is open towards interplanetary space. The profile $B(s)$ is taken from the coronal funnel model of Hackenberg et al. (2000). It describes a magnetic structure that is open towards the solar wind and is characterized by a rapid expansion of the magnetic flux tube in the transition region and low corona (Gabriel, 1976). Towards the solar wind, the magnetic field decreases radially as $B \propto r^{-2}$, with $r$ being the distance from the solar center. The interplanetary magnetic field geometry of a Parker spiral is also taken into account, based on an average solar wind speed of $450\,\mathrm{km\,s^{-1}}$ in interplanetary space. $B(s)$ is displayed in Figure 2.5a. Note that the spatial coordinate, $s$, represents the height above the coronal base, not the distance from the solar center. The model extends from the coronal base into the interplanetary space beyond 1 AU. The

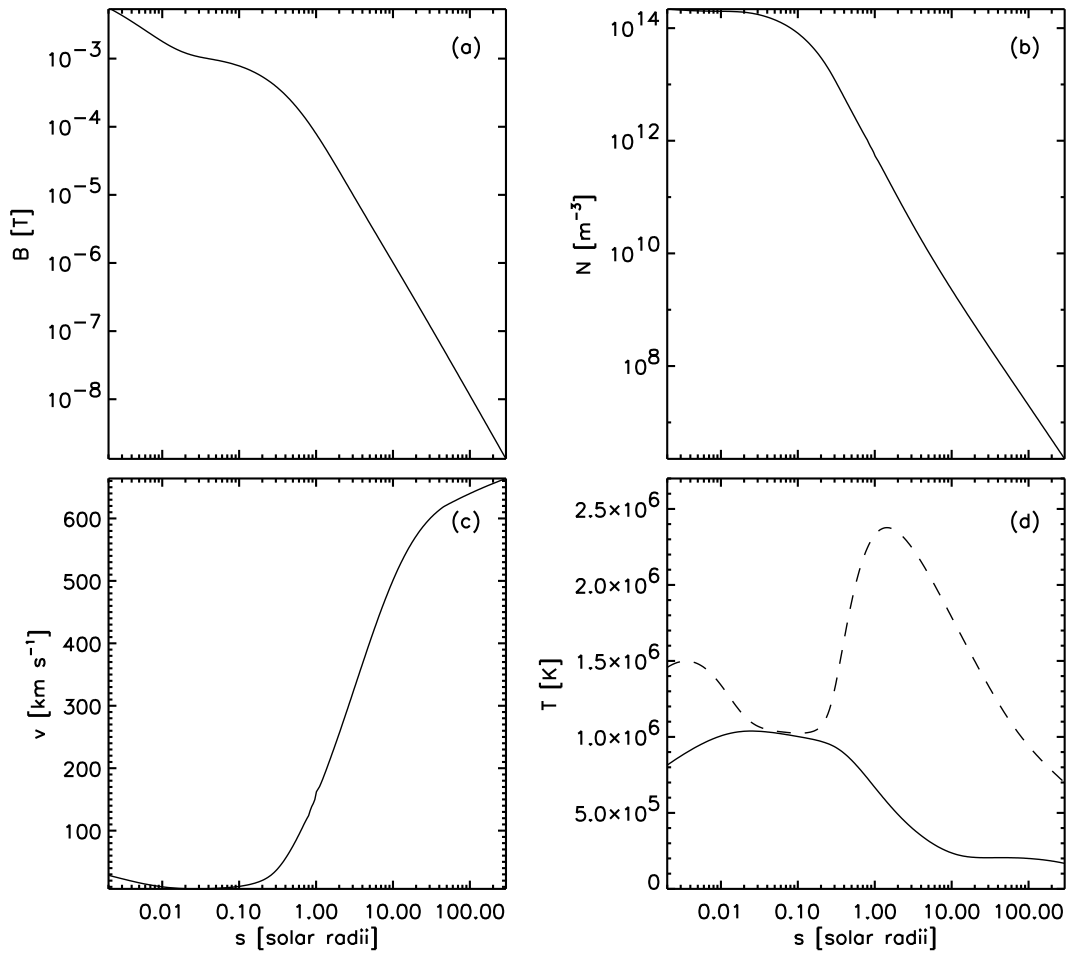


Figure 2.5: Background solar wind conditions for the kinetic model. Shown are: (a) the magnetic field, (b) particle number density for both protons and electrons, (c) flow speed, and (d) temperatures for electrons (solid line) and protons (dashed line). Note that the spatial coordinate, $s$, denotes the height above the coronal base along the magnetic flux tube under consideration, not the distance from the solar center.

logarithmic scale for $s$ allows a detailed look at the plasma conditions in the low corona. The rapid expansion of the coronal funnel in the low corona is clearly visible at the left border of Figure 2.5a. Within less than a percent of a solar radius the magnetic field decreases by a factor of 10. This rapid expansion ceases in the corona, and in interplanetary space the magnetic field decreases as $B \propto r^{-2}$.

Figure 2.5b shows the particle number density profile. The quasi-neutrality condition requires equal values for protons and electrons. The density decreases from $2 \cdot 10^{14}\,\mathrm{m}^{-3}$ at the coronal base to some $10^{6}\,\mathrm{m}^{-3}$ in the solar wind at 1 AU. Figure 2.5c displays the solar wind speed. It reaches a value of nearly $700\,\mathrm{km\,s}^{-1}$ at 1 AU. This is reasonable, since open magnetic structures like the coronal funnel modeled here are well known as the sources of the fast solar wind.

In Figure 2.5d, the temperatures of both protons and electrons are plotted. The protons are heated by ion cyclotron waves and reach a maximum temperature of $2.4 \cdot 10^{6}\,\mathrm{K}$. Towards the solar wind, both proton and electron temperatures decrease with height. Below the temperature maximum of

the protons, the particle densities are higher and the Coulomb collisions can provide an efficient heat exchange between protons and electrons. Thus, proton temperatures are lower there, and equal to the electron temperatures that reach a maximum. At the coronal base, where the funnel expands rapidly, the proton temperature shows a local maximum. This is due to the heating mechanism based on resonant absorption of ion cyclotron waves. The rapid decrease of the magnetic field with height corresponds to a rapid decrease of proton cyclotron frequency and dissipation of the wave power in this frequency range. This "frequency sweeping" mechanism leads to a high heating rate at this location.

### 2.4.3 Kinetic results for solar wind electrons

The kinetic model for electrons in the solar corona and wind is based on the solution of the Boltzmann-Vlasov equation (1.7) in the non-relativistic limit. On the right hand side the diffusion terms both due to interaction of electrons with whistler waves and due to Coulomb collisions are considered.

The Coulomb collisions of electrons with both electrons and protons are calculated using the Landau collision integral (Ljepojevic & Burgess, 1990). In order to yield analytic expressions for the diffusion coefficients, Maxwellian VDFs of the collision partners are assumed. This is a good assumption, since the thermal cores of both particle populations provide the largest contributions to Coulomb collisions. The reason for this is the small number densities of particles in the suprathermal tails of the VDFs, and the $v^{-3}$ dependency of Coulomb collision frequencies. For the protons, a Maxwellian has to be assumed anyway, since the background model as a fluid model only yields values for the density, drift velocity and temperature of the protons, but no information on the VDFs themselves. For the electrons, the shape of the VDF is to be investigated, and deviations from a Maxwellian in the tails of the distribution are expected. But the core of thermal electrons should still be close to a Maxwellian, since they are influenced a bit by Coulomb collisions, see Table 1.1. So the assumption of a Maxwellian VDF for the collision partners in electron - electron collisions is not problematic.

A VDF $f(\vec{r}, \vec{p}, t)$ depends on three spatial, three momentum, and on the time coordinate. Since the numerical effort to solve the Boltzmann-Vlasov equation for this $f$ is far too high, a simplification is necessary. This simplification is the assumption of gyrotropy. It is very reasonable, since the electron gyroperiods are much smaller than any other characteristic time scale. This assumption reduces the momentum coordinates $\vec{p}$ to two components, like absolute value and pitch-angle, $(p, \theta)$, or the components parallel and perpendicular to the background magnetic field, $(p_\parallel, p_\perp)$. The spatial coordinates $\vec{r}$ are reduced to $s$, the coordinate along the magnetic flux tube.

The kinetic model presented in this chapter only covers non-relativistic energies, and the velocity coordinates $(v_\parallel, v_\perp)$ are used. For a gyrotropic VDF $f(s, v_\parallel, v_\perp, t)$, the Boltzmann-Vlasov equation (1.7) reads:

$$\frac{\partial f}{\partial t} + v_\parallel \frac{\partial f}{\partial s} + \left( g_\parallel - \frac{e}{m_e} E_\parallel \right) \frac{\partial f}{\partial v_\parallel} + \frac{v_\perp}{2A} \frac{\partial A}{\partial s} \left( v_\perp \frac{\partial f}{\partial v_\parallel} - v_\parallel \frac{\partial f}{\partial v_\perp} \right) = \left( \frac{\delta f}{\delta t} \right)_{\mathrm{w}} + \left( \frac{\delta f}{\delta t} \right)_{\mathrm{Coul.}} \tag{2.13}$$

Only the components of the gravitational field, $\vec{g}$, and the charge separation electric field, $\vec{E}$, parallel to the background magnetic field enter the Boltzmann-Vlasov equation. The last term on

the left-hand side of equation (2.13) arises from the mirror force influencing the electrons due to change of the the cross sectional area, $A(s) \propto B^{-1}(s)$, of the magnetic flux tube with height, $s$. The quasilinear diffusion equation (2.4) takes a very simple form in the coordinates $(v_\parallel, v_\perp)$ (Marsch, 1998):

$$\left(\frac{\partial f}{\partial t}\right)_{\mathrm{w}} = \frac{\partial}{\partial v_\parallel}\left[\frac{1}{\tau} v_\perp \left(v_\perp \frac{\partial f}{\partial v_\parallel} + (v_{\mathrm{ph}} - v_\parallel)\frac{\partial f}{\partial v_\perp}\right)\right] + \frac{\partial f}{\partial v_\perp}\left[\frac{1}{\tau}(v_{\mathrm{ph}} - v_\parallel)\left(v_\perp \frac{\partial f}{\partial v_\parallel} + (v_{\mathrm{ph}} - v_\parallel)\frac{\partial f}{\partial v_\perp}\right)\right] \quad (2.14)$$

To find a solution of the Boltzmann-Vlasov equation (2.13), the temporal evolution of the electron VDF $f(s, v_\parallel, v_\perp, t)$ is iterated starting from an initial condition until a final steady state is reached. This $f(s, v_\parallel, v_\perp, t)$ is calculated against the background of the 2-fluid model for the solar corona and wind. In a self-consistent kinetic model for the electrons, the moments, as density, $N_{\mathrm{e}}$, flow speed, $v_{\mathrm{D}}$, temperature, $T$, and heat flux, $q$, of the electron VDF would have to be considered in the fluid equations to determine the charge separation electric field and the heat exchange between protons and electrons. However, such a method would require a recalculation of the fluid model in each time step. The computer costs for such a procedure would be forbiddingly high.

Instead, the electron VDF is calculated against the background fluid model that is computed once and considered to be constant in time. This simplification has not too strong consequences for the Boltzmann-Vlasov equation. The background conditions enter the kinetic model through the electric field, the Coulomb collision parameters, and the wave propagation properties in the simulation box. Replacing them by values from a background that is held constant greatly reduces the numerical effort and just enables the calculation of electron VDFs from the coronal base up into the solar wind.

### The simulation box

The simulation box extends from the upper transition region at a temperature level of $7 \cdot 10^5$ K up to 3.9 AU in interplanetary space. Due to the assumption of a gyrotropic electron VDF, the computational domain is composed of one spatial coordinate, $s$, along the background magnetic field $\vec{B}$, and the two velocity coordinates, $v_\parallel$ and $v_\perp$, parallel and perpendicular to $\vec{B}$, respectively. $s = 0$ corresponds to the lower boundary of the simulation box in the transition region.

The spatial grid step size $\Delta s$ of the computational mesh increases from 120 km in the transition region up to 0.62 AU at 3.9 AU. This resolves the pressure scale height in the low corona and keeps the number of spatial grid points at a manageable level. At a solar distance of 1 AU, $\Delta s = 0.18$ AU. The simulation results can be compared with the WIND data in Figure 1.3, that were collected at 1 AU. In order to avoid any influence of the upper boundary of the box on the simulation results there, the box extends much farther out into interplanetary space.

The velocity coordinates cover electron speeds up to 0.15 $c$. This corresponds to an electron energy of 5.7 keV. The main objective of this model is to study the formation of the electron strahl and halo at much lower energies $E < 1$ keV. This choice of the velocity range of the box prevents the model results from being influenced by the high-speed boundaries of the box. The velocity grid step sizes are equidistant with $\Delta v_\parallel = \Delta v_\perp = 1500\,\mathrm{km\,s^{-1}}$. This is a considerable fraction of the electron thermal speed, e.g. $v_{th} = 3893\,\mathrm{km\,s^{-1}}$ for $T = 10^6$ K. But it is not the aim of this model to resolve the thermal core of the electron VDF accurately. Smaller $\Delta v$ would increase the computer

costs both due the higher number of grid points, and because they require smaller time steps $\Delta t$ in iterating toward a solution of the Boltzmann-Vlasov equation (2.13) that is stationary in time. Since a simulation run already took more than one week with $\Delta v_{\parallel} = \Delta v_{\perp} = 1500\,\mathrm{km\,s^{-1}}$ on a Beowulf cluster, a reduction of the $\Delta v$ is not feasible.

**Resulting electron VDFs**

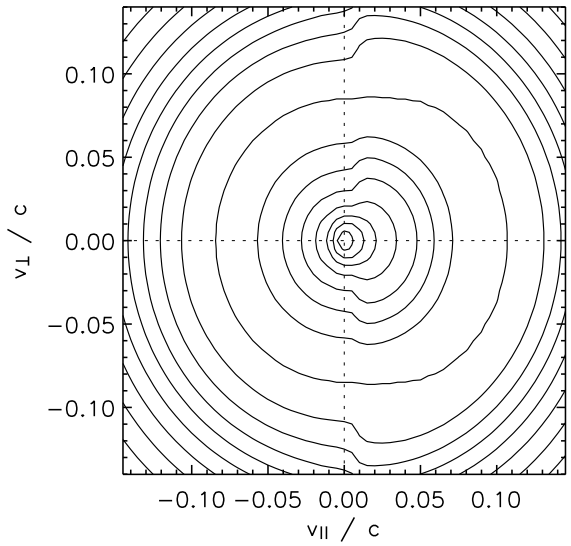


Figure 2.6: Isolines of the electron VDF at $s = 0.96$ AU for the solar wind kinetic model of Vocks et al. (2005)

Figure 2.6 shows the resulting electron VDF at $s = 0.96$ AU. Due to the action of the sunward propagating part of the whistler wave spectrum, the electron VDF displays only small pitch-angle gradients in the range of positive $v_{\parallel}$, and the extremely narrow beam that formed in the model without whistlers (Figure 2.2) has disappeared. Furthermore, the spacing between the isolines of the VDF is much smaller at low speeds $v < 0.02\,c$ than at higher speeds. $v = 0.02\,c$ corresponds to an electron energy of 100 eV. Since the isolines would form equidistant circles for a Maxwellian VDF, this feature can be interpreted as thermal core and an extended halo.

Figure 2.7 provides a close-up view of Fig. 2.6 for electron velocities up to $0.065\,c$. It enables a comparison with the WIND data in Fig. 1.3. Instead of the narrow beam in the model without sunward propagating whistlers, a strahl with a finite width has developed at low speeds $v_{\parallel} < 0.04\,c$, that is in fairly good agreement with the WIND observations in the fast solar wind, Fig. 1.3. At higher speeds, the electron distribution tends to be more isotropic.

This result shows that whistler waves fundamentally change the shape of solar wind electron VDFs. Despite the low spectral power of the whistlers, they can overcome the focusing by the mirror force and isotropize the distribution. The basic effect of the resonant interaction of solar wind electrons with whistlers is pitch-angle diffusion in the reference frame of the waves, but since the whistler wave phase speeds are smaller than the electron thermal speed, this cannot be discriminated from pitch-angle diffusion in the plasma frame.

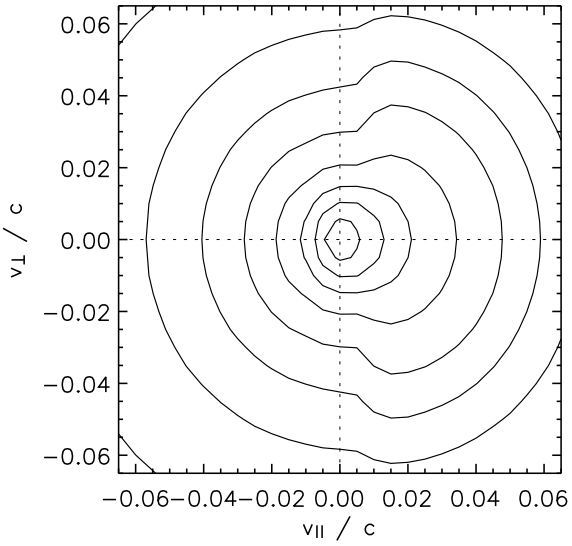


Figure 2.7: Close-up view of the isolines of the electron VDF at $s = 0.96$ AU.

However, there is one feature in the simulation results that is not confirmed by the WIND observations: Along the line $v_\parallel = 0$, the electron VDF in Fig. 2.7 shows a strong pitch-angle gradient.

The efficiency of the pitch-angle diffusion by resonant whistler-electron interaction depends on the "collision frequency" $1/\tau$ in the diffusion equation (2.4). The definition (2.6) shows that $1/\tau$ depends on the spectral wave power at the resonance frequency, $\omega_{\rm res}$. For a given electron speed $v_\parallel$, $\omega_{\rm res}$ is defined by the resonance condition, Eq. (2.7). Due to the frequency dependence of the wave phase speed, $v_{\rm ph} = \omega/k_\parallel$, and thus of $k_\parallel$, this is an implicit equation for $\omega_{\rm res}$.

Only anti-sunward moving electrons, $v_\parallel > 0$, can fulfill the resonance condition with sunward propagating whistlers, $k_\parallel < 0$. The smaller the electron speed, the higher the resonance frequency. In the limit $v_\parallel \to 0$, $\omega_{\rm res}$ approaches $\Omega_{\rm e}$. The very steep wave spectrum with a spectral coefficient of -2.6 in Eq. (2.10) then has the consequence that slow electrons interact with much less wave power than faster electrons.

**Diffusion across $v_\parallel = 0$**

Figure 2.8 displays the "collision frequency" $1/\tau$ as a function of the electron velocity component $v_\parallel$ parallel to the background magnetic field. It can clearly be seen that $1/\tau$ sharply drops for $v_\parallel < 0.01\,c$. The little bulge around $v_\parallel = 0.02\,c$ is due to the increase of the fraction of the whistler waves to the total wave power at frequencies above the lower hybrid frequency, as it is shown in Fig. 2.4.

The slow electron diffusion at $v_\parallel \to 0$ results in a low diffusion rate across the line $v_\parallel = 0$. The diffusion is more efficient at higher $v_\parallel > 0$. Since the whistler waves diffuse the electrons away from the narrow beam that forms without sunward propagating whistlers, the electron phase space density at $v_\parallel > 0$ and $v_\perp > 0$ is increased there. For negative speeds, $v_\parallel < 0$ the increase as compared to the model of Vocks & Mann (2003) without interplanetary whistlers is much smaller.

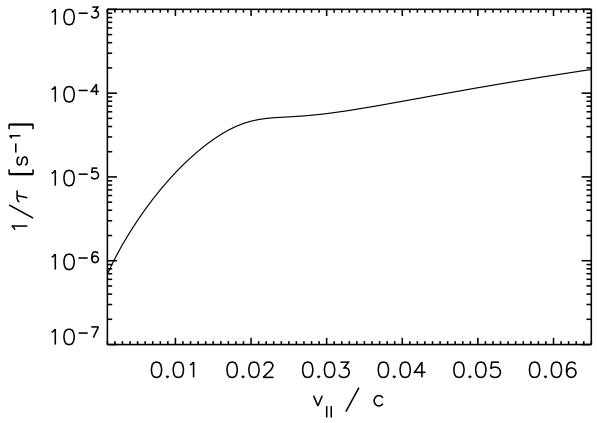


Figure 2.8: Wave-electron "collision frequency" $1/\tau$ as a function of $v_\parallel$ at $s = 0.96\,\mathrm{AU}$.

The lack of diffusion across the line $v_\parallel = 0$ leads to the formation of a sharp pitch-angle gradient across $v_\parallel = 0$.

This model considers only the resonant interaction between electrons and whistler waves that propagate either parallel or antiparallel to the background magnetic field. As mentioned above, the consideration of obliquely propagating waves would greatly increase the complexity of the quasilinear description and is beyond the scope of this work. It is conceivable that this simplification is responsible for the low diffusion across $v_\parallel = 0$ and the effective separation of the two half-spaces $v_\parallel > 0$ and $v_\parallel < 0$.

Another model assumption is the limit of sharp resonance between electrons and whistler waves, i.e. small damping $|\gamma| = |\mathrm{Im}(\omega)| \ll \mathrm{Re}(\omega)$ implicit in quasilinear theory (Kennel and Engelmann, 1966). Bieber et al. (1994) introduce dynamical effects associated with turbulence, that provide a finite scattering rate at a pitch-angle of 90 degrees, in order to bring the scattering theory of energetic particles in the heliosphere into agreement with observations. Dröge (2003) further investigates the role of resonance broadening and finds that it can strongly enhance the diffusion across $v_\parallel = 0$. But again the inclusion of these effects would greatly increase the complexity of the model and prevent an employment of the numerical method used here.

Thus, it is reasonable to assume that the "collision frequency" $1/\tau$ for small $v_\parallel$ is higher than it is displayed in Fig. 2.8. In order to overcome the model artifact of small $1/\tau$ for $v_\parallel \to 0$, and to represent the effects of diffusion mechanisms that are not considered here, some diffusion of $1/\tau$ along $v_\parallel$ is introduced. For each grid point $i$ of the computational mesh $(1/\tau)_i$ is replaced by

$$\left(\frac{1}{\tau_i}\right) \to 0.4 \cdot \left(\frac{1}{\tau_i}\right) + 0.2 \cdot \left(\left(\frac{1}{\tau_{i+1}}\right) + \left(\frac{1}{\tau_{i-1}}\right)\right) + 0.1 \cdot \left(\left(\frac{1}{\tau_{i+2}}\right) + \left(\frac{1}{\tau_{i-2}}\right)\right) \tag{2.15}$$

With a grid spacing $\Delta v_\parallel = 1500\,\mathrm{km\,s^{-1}}$ this corresponds approximately to a sliding average over the curve in Fig. 2.8 with a window width of $0.01\,c$. It strongly reduces the sharp drop at small $v_\parallel$, but barely influences $1/\tau$ at higher electron speeds parallel to the background magnetic field.

Figure 2.9 shows the isolines of the electron VDF at $s = 0.96\,\mathrm{AU}$ that has been calculated under consideration of the diffusion in $1/\tau$, Eq. (2.15). The diffusion has greatly reduced the pitch-angle gradient across $v_\parallel = 0$.

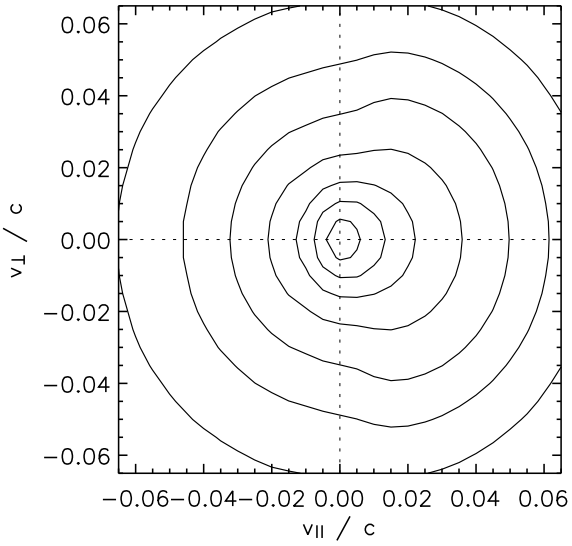


Figure 2.9: Isolines of the electron VDF at $s = 0.96$ AU from the simulation run including diffusion in $1/\tau$.

The WIND observations of electron VDFs, that are displayed in Fig. 1.3, show only very small pitch-angle gradients at $v_{\parallel} = 0$, indicating that the efficiency of electron diffusion at $v_{\parallel} = 0$ is not much lower than at other pitch angles. In many cases observations show that there are even slightly more electrons on the side $v_{\parallel} < 0$ than on $v_{\parallel} > 0$, resulting in an reversed pitch angle gradient from the one in Fig. 2.9.

Pitch-angle diffusion alone tends to smooth out any pitch-angle gradient, but cannot reverse it. Even if the effects of obliquely propagating whistlers were properly considered here, they could not lead to such a reversal. Thus some other effects must play a role in these cases. One possibility is the transport of electrons parallel to the background magnetic field, $\vec{B}$, according to their $v_{\parallel}$. The electron speeds parallel to the background magnetic field are modified by the pitch-angle scattering, and the mirror force tends to push them towards positive $v_{\parallel}$. Since the electron density varies with solar distance along $\vec{B}$, it is conceivable that these dynamics influence the pitch-angle distribution of the electrons. But since the model results that are displayed in Fig. 2.9 still show some pitch-angle gradient at small $v_{\parallel}$ that is not in coincidence with the WIND data, the investigation of such effects is beyond the scope of the current version of the electron kinetic model.

The isolines of the electron VDF in Fig. 2.9 show a strong anisotropy between positive and negative $v_{\parallel}$. The isolines are extended towards higher $v_{\parallel}$ for $v_{\parallel} > 0$. This anisotropy closely resembles the strahl in the WIND observations, Fig. 1.3. The electron VDF becomes more isotropic with increasing energy, in good agreement with the WIND observations.

These simulation results show that the inclusion of some diffusion in $1/\tau(v_{\parallel})$ alleviates the influence of the simplifying assumption of wave propagation solely parallel to the background magnetic field, and leads to model results that exhibit some basic properties of solar wind electron VDFs as they are observed in interplanetary space.

Figure 2.10 shows a cut of the electron VDF in Fig. 2.9 along the line $v_{\perp} = 0$. The figure also

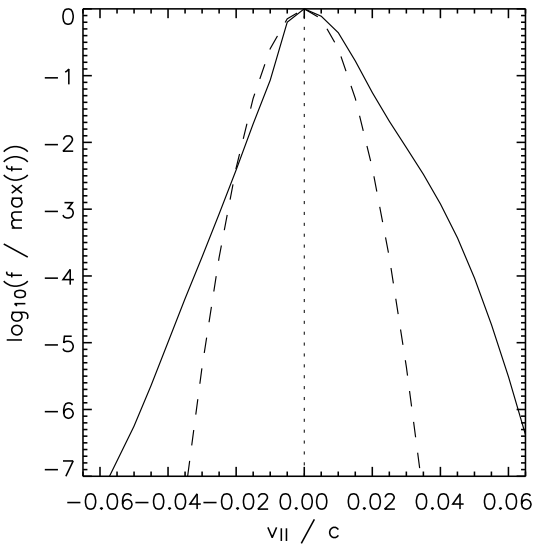


Figure 2.10: Cut along the line $v_\perp = 0$ of the electron VDF at $s = 0.96\,\mathrm{AU}$ from the simulation run including diffusion in $1/\tau$ (solid line) and a Maxwellian VDF with the same density and temperature (dashed line).

displays a Maxwellian VDF with the same density and temperature. The strahl in Fig. 2.9 appears as an enhancement of the electron VDF for $v_\parallel > 0$ over the corresponding $v_\parallel < 0$. The values for $v_\parallel = v$ and $v_\parallel = -v$ approach each other with increasing speed $v$. This is a manifestation of the tendency of the electron VDF to become more isotropic at higher energies that has been found in Fig. 2.9.

A comparison of the electron VDF in Fig. 2.10 with the model of Vocks & Mann (2003) without sunward propagating whistlers shows that the whistlers not only have a strong impact on the VDF in the velocity range $v_\parallel > 0$, but also in the range $v_\parallel < 0$. For positive $v_\parallel$, the values of the VDF are slightly reduced since electrons are scattered away from the extremely narrow beam. But for $v_\parallel < 0$, the electron VDF now is considerably enhanced above the Maxwellian VDF, in strong contrast to exospheric models where no electrons return towards the Sun. These results show that the sunward propagating whistler waves, even if their energy corresponds to a small fraction of the total wave power in interplanetary space, limit the focusing of the strahl and furthermore lead to the formation of a halo component of the electron VDF.

### Conclusions for the kinetic solar wind model

Adding an interplanetary whistler wave spectrum with waves propagating both towards and away from the Sun to the kinetic model shows that the whistlers can influence the electron VDF at 1 AU significantly. The electrons are effectively diffused away from the extremely narrow beam for all energies in the simulation box, despite of the low whistler wave intensity of just 1% of the total wave power for each propagation direction. Since the resonance frequency of whistler waves decreases with increasing electron speed, $v_\parallel$, and the spectral wave power, Eq. (2.12) increases with decreasing frequency, the pitch-angle diffusion can become so strong that beaming electron

distributions are completely eliminated.

The simplifying model assumptions of whistler waves propagating only parallel to the background magnetic field and the zero wave growth rate limit of quasi-linear theory lead to an artificial separation between the two velocity half-spaces $v_\parallel > 0$ and $v_\parallel < 0$, that results in a strong pitch-angle gradient across the line $v_\parallel = 0$, with a higher phase space density for $v_\parallel > 0$. This separation can be reduced by introducing some diffusion of the wave-particle "collision frequency" $1/\tau$ along $v_\parallel$.

This modification aims at addressing the effects of obliquely propagating whistlers and other effects like resonance broadening that enhance diffusion across the line $v_\parallel = 0$. It reduces the separation between the velocity half-spaces, but it does not entirely rule out the pitch-angle gradient at small $v_\parallel$. Electron VDFs that have been recorded by the WIND spacecraft in the fast solar wind show only small pitch-angle gradients in this region of velocity space, in many cases with slightly higher phase space densities at $v_\parallel < 0$. The kinetic model presented here cannot address this feature due to the still important simplification of considering only whistler waves that propagate parallel to the background magnetic field.

Beside from this pitch-angle gradient at small $v_\parallel$, the kinetic results are in very good agreement with electron VDFs observed by WIND. At energies well below 1 keV, a strahl is visible both in the simulation and spacecraft data, and at higher energies the electron distribution becomes isotropic. The sunward propagating whistler waves lead to the formation of a halo component of the electron VDF, as a result of the pitch-angle diffusion of the strahl population. Scattering of strahl electrons into the halo is also found in observational studies of solar wind electron VDFs (Maksimovic et al., 2005; Pagel et al., 2007; Štverák et al., 2009). So it has to be concluded that scattering of electrons by whistler waves plays an important role in the evolution of solar wind VDFs.

These results demonstrate that whistler waves can play a significant role in interplanetary space, even for low wave power. This has strong implications on the transport of suprathermal electrons in the solar wind. The pitch-angle diffusion caused by the waves has the tendency to isotropize the electron VDF, and thus to compensate the focusing effect of the mirror force. Furthermore, electrons that move anti-sunwards with $v_\parallel > 0$ can be scattered to $v_\parallel < 0$ and travel back towards the Sun and interact with anti-sunwards propagating whistler waves in the solar wind or even in the solar corona. The waves and the mirror force can bring them back to $v_\parallel > 0$ so that they move away from the Sun again. Some electrons can be subject to several of such cycles.

With this kinetic model, the electron halo and strahl formation in the solar wind has been studied under quiet solar conditions. The background conditions and the electron VDFs produced by the model do not change in time. But energetic electrons that are emitted in solar energetic particle events can also be affected by resonant wave-particle interaction. A study of the implications of the whistler waves on their propagation through interplanetary space is the topic of the next chapter.

# Chapter 3

# Scattering of solar energetic electrons in interplanetary space

In the previous chapter the influence of whistler wave scattering on solar wind electron distributions has been discussed for quiet solar conditions. Those results represent a stationary state. But interplanetary space can be highly dynamic. Solar flares are well known for generating high fluxes of energetic electrons. These electrons lead to the emission of radio waves as they traverse the background plasma of the solar corona, and release X-rays through bremsstrahlung and thermal emission when they are stopped by the ambient medium. But solar energetic electrons can also escape from the solar corona into interplanetary space, where they are directly observed by spacecraft (Lin, 1974). Since electrons with higher energies move with higher speeds, they arrive earlier at the observer than those with lower energies. This velocity dispersion provides the opportunity to infer electron release times and travel path lengths from energy-dependent electron arrival times as registered by spacecraft (Krucker et al., 1999; Classen et al., 2003).

However, one would expect that electron arrival times at an observer located at a solar distance of 1 AU are influenced by scattering of the electrons by whistler waves in interplanetary space. If the scattering modifies the arrival times significantly, this could lead to severe errors in the path lengths and release times as yielded by a simple velocity-dispersion analysis based on the assumption of scatter-free electron propagation.

Indeed, substantial time differences are found frequently between the electron release times that are inferred from velocity-dispersion observations, and the onset of X-ray and radio emission that indicates the presence of energetic electrons in the solar corona, e.g. (Krucker et al., 2007; Haggerty & Roelof, 2002; Klassen et al., 2002). The release of energetic electrons into interplanetary space seems to be delayed from 10 min to 30 min.

But on the other hand, the electron travel times in Krucker et al. (1999) and Classen et al. (2003) are found to be inversely proportional to the electron speed. So the scatter-free assumption seems to work well.

This raises the question of whether the energetic electrons in interplanetary space belong to the same population that leads to coronal X-ray and radio emission in the solar corona, and if so, whether they are stored in the solar corona prior to their release, or if they are delayed due to

scattering in interplanetary space. Cane (2003) presents interplanetary type III radio burst observations, i.e. signatures of energetic electron beams (Suziki & Dulk, 1985), and argues that the electrons are delayed in interplanetary space, while Klein et al. (2005) come to the conclusion that the origin of delayed electron releases is the interplay between electron acceleration and injection into different magnetic structures in the solar corona. So it is worthwhile to have a closer look at the impact of whistler wave scattering on electron arrival times at 1 AU.

## 3.1 The model

In order to investigate to what extent the scattering of solar wind electrons by resonant interaction with whistler waves in interplanetary space influences their arrival times at 1 AU, the kinetic solar wind model from the previous chapter has been used by Vocks & Mann (2009) to study the propagation of energetic electrons after their release in a solar flare in the lower corona.

The solar wind background model from the previous chapter and the whistler wave spectrum in interplanetary space are unaltered. The kinetic model is based on the relativistic form (1.6) of the Boltzmann-Vlasov equation, and uses as momentum coordinates the absolute value and pitch-angle $(p, \theta)$ instead of the components $(p_\parallel, p_\perp)$. The electron-whistler interaction is described by the quasilinear diffusion equation (2.4). The resonance condition (2.7) and the requirement $\omega < \Omega_e$ from the whistler wave dispersion relation (2.8) result in high electron speeds being connected with low wave frequencies. Due to the power-law spectrum (2.10) of whistlers in interplanetary space, this has the consequence that electrons with high energies are scattered more strongly than those with low energies.

The diffusion equation (2.4) provides an estimate of electron mean free paths. For solar energetic electrons with energies of several 10 keV, they are typically of the order 0.8 AU. Thus, energetic electrons can be expected to be delayed by a substantial fraction of the free-propagation time from the Sun to 1 AU, which is e.g. 1250 s for 40 keV electrons. So delays by several minutes seem to be possible.

The lower boundary of the simulation box is located in the corona, 40 Mm above the coronal base. The Box extends 3 AU into interplanetary space. The lower boundary is open to electrons that leave it with a negative momentum component $p_\parallel < 0$, while electrons with $p_\parallel > 0$ enter it with a VDF that is provided as a boundary condition. Normally, this would be a Maxwellian distribution with typical coronal density and temperature. But a Maxwellian distribution shows strong phase-space gradients for higher electron energies of several 10 keV. Since they cause numerical problems, a kappa distribution (2.3) is used instead, with a high $\kappa = 30$. Note that this kappa distribution becomes a Maxwellian in the limit $\kappa \to \infty$. At low energies there is little difference between the kappa distribution and a Maxwellian, and the core of the VDF rapidly thermalizes. So there is no inconsistency with the assumption of Maxwellian collision partners in the calculation of Coulomb collision coefficients (Ljepojevic & Burgess, 1990).

### 3.1.1 Solar flare electrons

The injection of solar flare electrons into the simulation box is done by modifying this lower boundary condition. The flare electrons have a power-law distribution whose parameters are derived from observations with the solar X-ray telescope *RHESSI* (Lin et al., 2002).

The total number density of flare energetic electrons, $N_{\mathrm{f,tot}}$, propagating downwards from the flare site can be derived by dividing the electron flux distribution, which is obtained from hard X-ray (HXR) spectra, by the electron speed and the area of the thick-target interaction, i.e. the HXR footpoint area, and integrating over all electron energies. Using *RHESSI* data (Lin et al., 2003), Holman et al. (2003) have obtained values of the order of $N_{\mathrm{f,tot}} = 10^{15}\,\mathrm{m}^{-3}$ for the peak of an X-class flare. Krucker et al. (2007) have shown that the total number of electrons injected into interplanetary space is just a small fraction of the HXR-producing ones, on average 0.2%. A value of $N_{\mathrm{flare}} = 10^{11}\,\mathrm{m}^{-3}$, which reflects the density of electrons propagating outwards in a medium-sized flare, is thus adopted.

$\delta = 4$ is chosen as a representative spectral index of the accelerated electron flux, see (Krucker et al., 2007; Warmuth et al., 2009). Both rise and fall times of the electron injection profile were taken as 1 min, which is a typical value both for HXR pulses and type III radio bursts, see Fig. 1 in (Krucker et al., 2007). The flare electron distribution has a low-energy cutoff at 20 keV, below which the distribution is assumed to be constant.

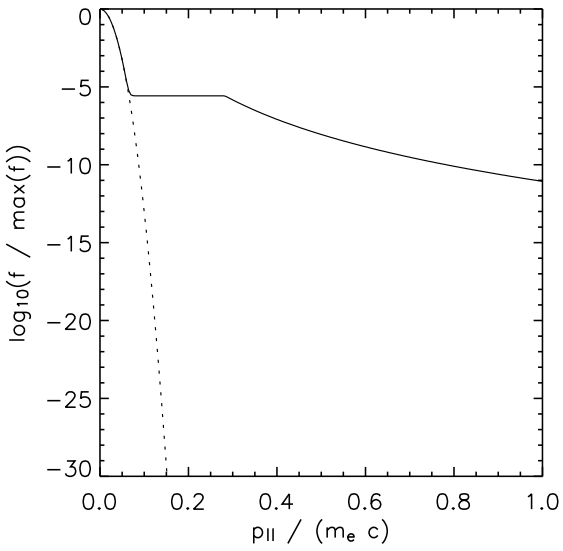


Figure 3.1: Cut along the line $p_\perp = 0$ of the electron VDF at the lower boundary during the solar flare (solid line), and Maxwellian VDF with the same density and temperature as the coronal background (dotted line).

Figure 3.1 shows the lower boundary condition during the solar flare. Note that the half-space $p_\parallel < 0$ is not relevant here, since these electrons do not enter the simulation box. At low energies, the VDF is dominated by the Maxwellian, or here $\kappa = 30$, distribution of the coronal background plasma.

As the energetic electrons propagate into interplanetary space after the onset of the flare, more energetic, i.e. faster, electrons will outpace the slower ones. The earlier arrival of more energetic electrons at some distance from the Sun has the consequence that the electron VDF there can become unstable to the generation of Langmuir waves, which eventually leads to the emission of type III radio emission. These processes are basically nonlinear, so that quasilinear theory is not applicable here. Thus, these processes are beyond the scope of this model. On the other hand, these nonlinear processes can stabilize the electron distribution (Thejappa et al., 1999). So, not including Langmuir wave generation in the model is a strong simplification, but not a too strong one.

## 3.2 Flare electron propagation and resulting arrival times

The kinetic model is based on calculating the temporal evolution of the electron VDF inside the box by solving the Boltzmann-Vlasov equation (1.6), and thus enables a study of flare electron propagation. Such an approach requires the definition of an initial condition for the electron VDF. This is provided by a kappa distribution (2.3) based on the local plasma conditions in the background solar wind model, and $\kappa = 30$. This is close to a Maxwellian VDF, as in the lower boundary condition. The upper boundary condition is defined in the same way. The large extent of the simulation box over 3 AU has been chosen in order to avoid any influence of the upper boundary on the simulation results at 1 AU. The injection of flare electrons at the lower boundary has already been described in the previous section.

The flare electron arrival time at any height in the simulation box is defined as the time when the spectral electron flux exceeds a threshold value of $0.01\,\mathrm{keV^{-1}cm^{-2}s^{-1}}$. This would correspond to a spectral flux of $1\,\mathrm{keV^{-1}s^{-1}}$ for a detector with an effective area of $100\,\mathrm{cm^2}$.

### 3.2.1 Beware of numerical diffusion

The numerical representation of the convection term of the gyrotropic Boltzmann-Vlasov equation, $v_\parallel \partial f/\partial s$, which looks rather innocuous, can have a significant influence on the simulation results. In an earlier version of the numerical code, a simple upwind difference scheme had been employed:

$$\frac{\partial f_i}{\partial s} = \begin{cases} (f_i - f_{i-1})/\Delta s, v_\parallel > 0 \\ (f_{i+1} - f_i)/\Delta s, v_\parallel < 0. \end{cases} \tag{3.1}$$

This first-order accurate scheme has the advantages of simplicity and stability, but it leads to strong numerical diffusion. The result is a spread of the rapid increase of energetic electron fluxes associated with the arrival of flare electrons over a wide spatial range in the model heliosphere, thus leading to erroneous arrival times.

This numerical diffusion can be strongly reduced by using a more advanced numerical scheme. For the study presented here, the "superbee flux limiter" has been chosen, see Yang & Przekwas (1992) for a review. For $v_\parallel > 0$, this scheme reads for a timestep $\Delta t$

$$\frac{\partial f_i}{\partial s} = \frac{g_{i+1/2} - g_{i-1/2}}{\Delta s} \tag{3.2}$$

with

$$g_{i+1/2} = f_i + \delta f_i \left(1 - v_{\parallel} \Delta t / \Delta s\right) / 2 \tag{3.3}$$

differences $\Delta f_i = f_i - f_{i-1}$ and finally:

$$\begin{aligned} \delta f_i \;\; = \;\; & (\mathrm{sgn}(\Delta f_i) + \mathrm{sgn}(\Delta f_{i+1})) \times \\ & \min(|\Delta f_i|, |\Delta f_{i+1}|, \max(|\Delta f_i|, |\Delta f_{i+1}|)/2) \end{aligned} \tag{3.4}$$

where $\mathrm{sgn}(x)$ returns the sign of $x$. The equations (3.2) and (3.3) resemble the simple upwind scheme, but the term $\delta f_i$ limits the fluxes between neighboring grid points and thus keeps numerical diffusion under control.

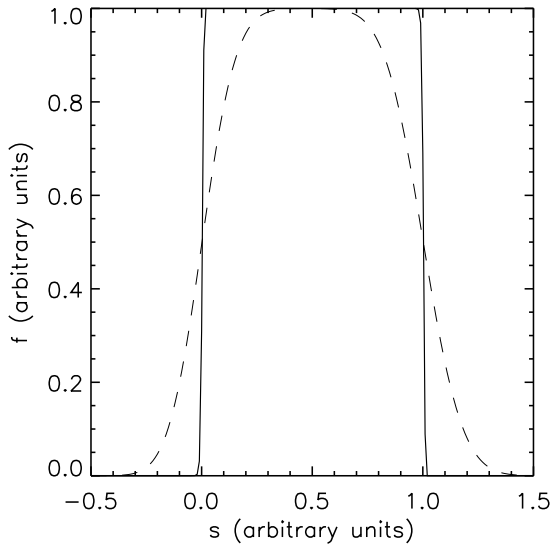


Figure 3.2: The shape of an initially rectangular pulse after convection over a distance of 4 times its width, both for the superbee scheme (solid line) and the upwind scheme (dashed line)

Figure 3.2 demonstrates the effect of numerical diffusion and its mitigation in a simple 1D-model. An initially rectangular pulse has been transported by 4 length units. The simple upwind scheme has rounded the corners significantly. It can easily be seen that an "arrival time" based on the value of the pulse exceeding e.g. 0.1 would be strongly affected by the diffusion. The more advanced scheme, on the other hand, yields much better results, and deviations from the initial rectangular shape are hardly visible.

### 3.2.2 Test run without whistler waves

In the previous sub-section it was shown that numerical artifacts might influence the calculated electron arrival times at 1 AU. Thus, it is reasonable to test the numerical model in a simulation run without any whistler waves first. The Boltzmann-Vlasov equation (1.7) now only has the Coulomb collision term on the right hand side. But electrons with energies of several tens of keV are basically scatter-free, see Table 1.1. So free propagation of flare electrons is expected,

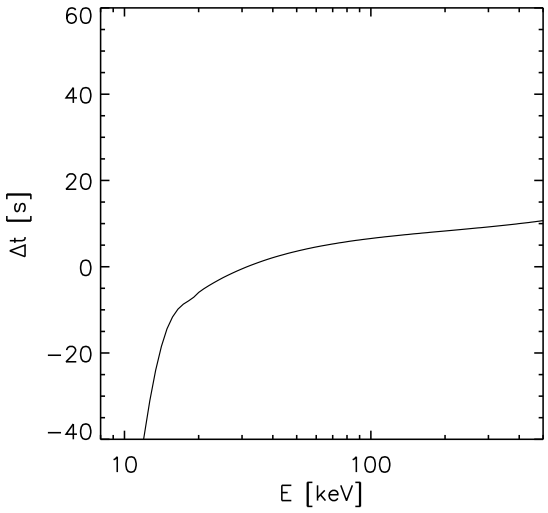


Figure 3.3: Difference of electron arrival times at $s = 1.07$ AU between the model without whistler waves and free propagation, as function of electron energy.

resulting in arrival times calculated as path lengths along the Parker spiral divided by electron speed.

Figure 3.3 shows the difference $\Delta t$ between the energetic electron arrival times calculated by the kinetic model and the free-propagation times. These values have been obtained at a spatial position of $s = 1.07$ AU along the Parker spiral, that corresponds to a radial distance of $r = 0.95$ AU from the Sun.

A positive $\Delta t$ means that the energetic electrons in the kinetic model arrive later than expected from free propagation. The figure shows that there is a delay of 10 s for the highest electron energies of about 500 keV. The delay decreases with decreasing energy, and becomes negative for energies below 30 keV.

Electrons with a kinetic energy of 500 keV have speeds of $v = 0.86\,c$. Their travel time over a distance of $s = 1.07$ AU is 618 s. So an artificial delay of 10 s in the model corresponds to an error of 1.6% in travel time, which is fairly good. So the model has passed the free-propagation test.

The negative values of $\Delta t$, i.e. early arrival of the flare electrons, for energies below 30 keV, are due to Coulomb collisions. The mechanism by which scattering of electrons in momentum or energy can lead to an early arrival of flare electrons is discussed below.

### 3.2.3 Pure pitch-angle diffusion

After the numerical model has been tested to yield reliable flare electron arrival times at a solar distance of about 1 AU, the effect of electron diffusion by resonant interaction with whistler waves is added. For typical solar wind conditions, the dispersion relation (2.8) yields whistler wave phase speeds of the order of 1000 km s$^{-1}$. This is comparable to electron thermal speeds. For energetic

electrons with speeds that are a substantial fraction of the light speed, pitch-angle scattering in the wave frame hardly differs from pitch-angle scattering in the plasma frame. This has already been pointed out in the discussion of Figure 2.3b. In such a plasma, the diffusion equation (2.4) is dominated by the coefficient $\alpha_{\theta\theta}$.

Under the simplifying assumption of pure pitch-angle diffusion, only the term $\alpha_{\theta\theta}$ needs to be considered in the quasilinear diffusion equation (2.4). This saves much computational effort, so it is worth investigating whether it is applicable without altering the simulation results.

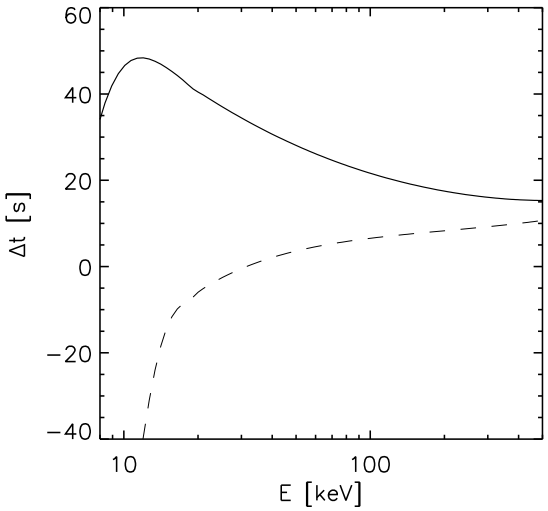


Figure 3.4: Difference of electron arrival times at $s = 1.07$ AU between the pure pitch-angle diffusion model and free propagation, as function of electron energy (solid line). The model results without whistler waves are also shown for comparison (dashed line).

Figure 3.4 shows the differences between the electron arrival times at $s = 1.07$ AU ($r = 0.95$ AU) and the expected times based on free propagation. The results of the simulation run without whistler waves are also plotted for comparison.

The results show that the pitch-angle diffusion delays the flare electrons considerably. For high electron energies of 500 keV, the delay is only 5 s, but it increases with decreasing energy. It is about 15 s for 100 keV, and 35 s for 30 keV. For energies little above 10 keV, the pitch-angle diffusion counters the early arrival of flare electrons caused by Coulomb collisions, leading to a delay of 60 s as compared to the whistler-free run, and to a peak of $\Delta t$ in the plot.

So the simulation run including pitch-angle diffusion by resonant interaction with whistler waves demonstrates that the whistlers can delay electron arrival times. The maximum delay found here is of the order of 1 min.

The energy dependence of the delay also needs some attention. The calculation of electron release times in analyses like that of Krucker et al. (2007) is based on scatter-free electron propagation

$$s = v(t_a - t_r) \tag{3.5}$$

along the path length $s$. $t_r$ and $t_a$ are the electron release and arrival times, respectively. $t_a$ is directly measured, the electron speed $v$ depends on the energy, but both $t_r$ and $s$ are unknown. Solving the above equation for $t_a$ and calculating the derivative in $v$ yields:

$$\frac{\partial t_a}{\partial v} = -\frac{s}{v^2}. \tag{3.6}$$

The velocity dispersion $\partial t_a/\partial v$ can be derived from satellite data and yields the path length $s$ by means of Eq. (3.6). Once $s$ is known, Eq. (3.5) provides the electron release time.

The energy dependence of $\Delta t$ as shown in Fig. 3.4 alters the velocity dispersion $\partial t_a/\partial v$ and thus introduces an error into the calculation of $s$. This contribution can be estimated to be of the order of 0.02 AU for electrons with an energy of 90 keV, leading to an error of 20 s in the release time.

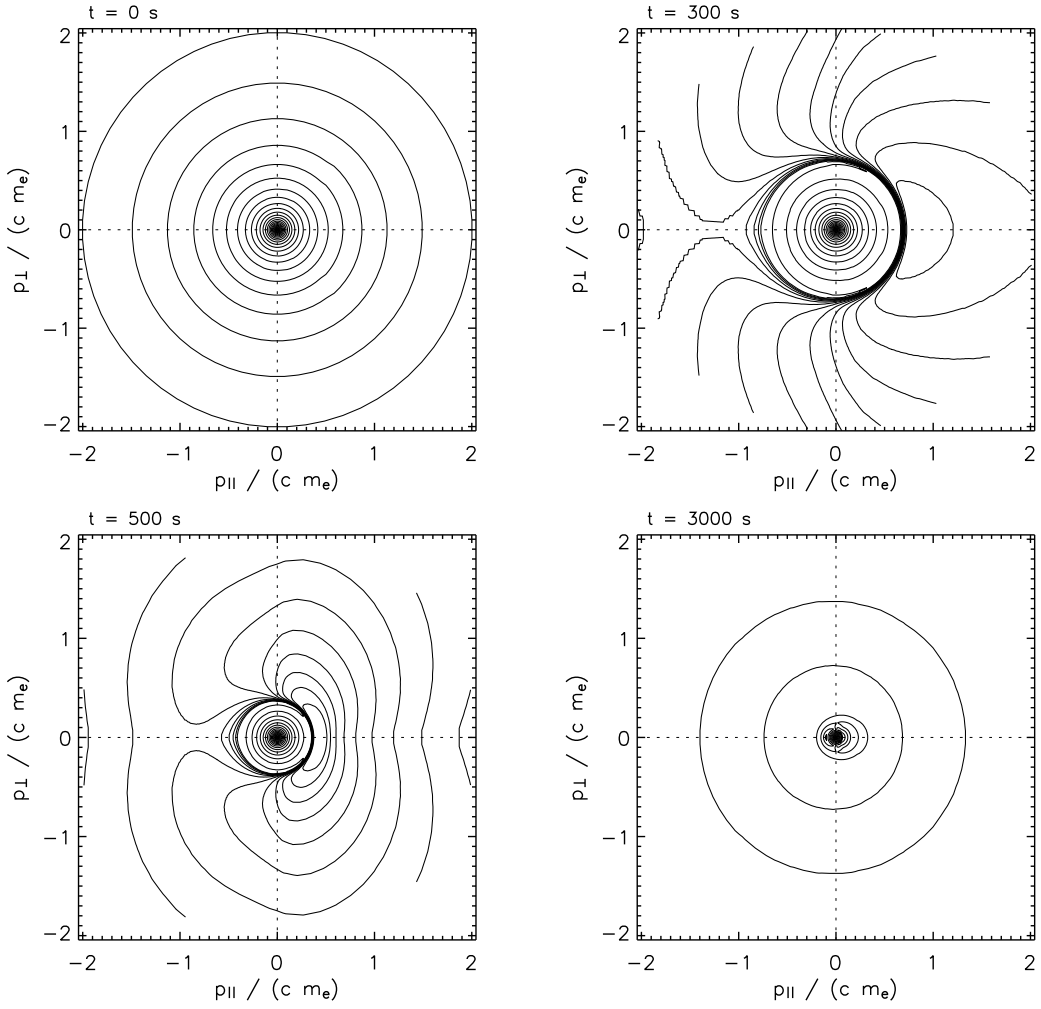


Figure 3.5: Electron VDFs at $s = 0.35$ AU for four different simulation times. The isolines are chosen in such a way that they would be equidistant for a Maxwellian VDF.

So far, only model results for the arrival times of energetic electrons at 1 AU have been presented, but not interplanetary electron VDFs during flare electron arrival. Figure 3.5 shows the VDF at $s = 0.35$ AU for four different simulation times, $t$. $t = 0$ s corresponds to the initial $\kappa = 30$

distribution. At $t = 300\,\mathrm{s}$ the flare electrons have arrived for electron momentum $p > 0.7\,m_\mathrm{e}c$. The pitch-angle scattering of them can be seen clearly. At $t = 500\,\mathrm{s}$, the energetic electrons can be found for $p > 0.35\,m_\mathrm{e}c$. At $t = 3000\,\mathrm{s}$ the flare is over, but the model heliosphere is still filled with an isotropic halo of energetic electrons. The pitch-angle scattering suppresses their escape through the upper boundary of the simulation box, they are kept there for simulation times of the order $10^5\,\mathrm{s}$, i.e. for days. This result resembles the super-halo of energetic electrons that is observed in solar wind electron VDFs even under quiet conditions (Lin, 1998).

These results are based on the model assumption of pure pitch-angle scattering. This scattering generally inhibits the transport of electrons straight along the background magnetic field, and thus leads to delayed arrival times at 1 AU. Diffusion along the momentum coordinate, $p$, has been deemed to be negligible, since the coefficient $\alpha_{pp}$ is small. However, the plots in Fig. 3.5, which show the arrival of flare electrons, indicate strong phase-space gradients along $p$.

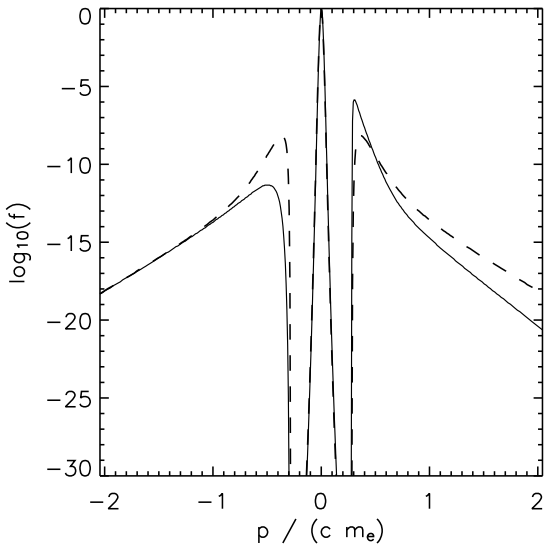


Figure 3.6: Cuts through the electron VDF at $s = 1.07\,\mathrm{AU}(r = 0.95\,\mathrm{AU})$ and simulation time $t = 2000\,\mathrm{s}$ along $p_\parallel$ (solid line) and $p_\perp$ (dashed line).

Figure 3.6 shows cuts through the electron VDF at $s = 1.07\,\mathrm{AU}(r = 0.95\,\mathrm{AU})$ during the arrival of flare electrons at a simulation time of $t = 2000\,\mathrm{s}$. It can be seen that the phase-space density jumps by more than 25 orders of magnitude over a momentum interval of $\Delta p = 0.1\,m_\mathrm{e}c$. Since a small diffusion coefficient, multiplied by an extreme gradient, can still yield substantial diffusion, it is now questionable whether pure pitch-angle diffusion is appropriate for energetic electrons in interplanetary space.

Diffusion across the strong gradient in Fig. 3.6 would transport electrons to lower momentum, i.e. to lower energy. Thus, at this lower energy, the phase-space density increases earlier than expected from scatter-free propagation, and these electrons also move further up in the box. As a consequence, diffusion in the momentum coordinate leads to an early arrival of energetic electrons as compared to the scatter-free expectation. This is also the reason why non-negligible Coulomb collisions lead to negative $\Delta t$ for energies below 20 keV in the test run without whistler waves, see Fig. 3.3.

The effect of diffusion in momentum space on the electron arrival times can be estimated as follows. A simple diffusion equation

$$\frac{\partial f}{\partial t} = \frac{\partial}{\partial p}\left(\alpha_{pp}\frac{\partial f}{\partial p}\right) \tag{3.7}$$

broadens a Gaussian distribution $f \propto \exp(-p^2/(2p_0^2))$:

$$\frac{\partial (p_0)^2}{\partial t} = 2\alpha_{pp}. \tag{3.8}$$

Thus, the width of the phase-space gradient in Fig. 3.6 would also be broadened if there were no propagation effects. Replacing $\partial(p_0)^2/\partial t$ by $v\partial(p_0)^2/\partial s$ and integrating from the lower boundary ($s = 0$) through the simulation box up to $s = 1.07\,\mathrm{AU}$($r = 0.95\,\mathrm{AU}$) yields a total $\Delta p_0$. The influence of such a broadening of the phase-space gradient on electron arrival times then can be estimated as $\Delta t = (t_\mathrm{a} - t_\mathrm{r})\Delta p_0/p$.

For 60 keV electrons, this yields an early arrival of 10 s in our model heliosphere. Thus, the early arrival of flare electrons due to diffusion in momentum space is of the same order of magnitude as the delay due to pitch-angle scattering. In other words, pure pitch-angle diffusion is not a valid approach, although the original diffusion equation (2.4) seems to be dominated by the pitch-angle term, $\alpha_{\theta\theta}$.

### 3.2.4 Full diffusion equation

So for solar energetic electron arrival times at 1 AU, the effect of electron diffusion along the momentum coordinate is not negligible compared to the effect of pitch-angle diffusion. The simplification of pure pitch-angle diffusion is not allowed. The full diffusion equation (2.4) has to be implemented instead.

Figure 3.7 shows the resulting arrival times for the full diffusion model, and the previous results for comparison. The strong delay that has been found in the pure pitch-angle diffusion model has almost disappeared. There is only a small difference of about 5 s compared to the free-propagation model.

This result confirms the above estimate of the influence of diffusion along the momentum coordinate on the arrival times. The early arrival of flare electrons is comparable to the delay due to pitch-angle diffusion. Thus, both parts of the full diffusion equation are capable of partly compensating each other.

It is also noteworthy that the new result for the delay of energetic electrons due to scattering in interplanetary space shows little energy dependence. The delay is rather constant, about 10 s over a wide energy range. Thus, it has little additional impact on inferred path lengths and release times of flare electrons.

### 3.2.5 Variation of the whistler wave power

All simulation results presented so far have been obtained with the whistler wave spectrum from chapter 2.4, that attributes 1% of the total wave power measured in interplanetary space to the

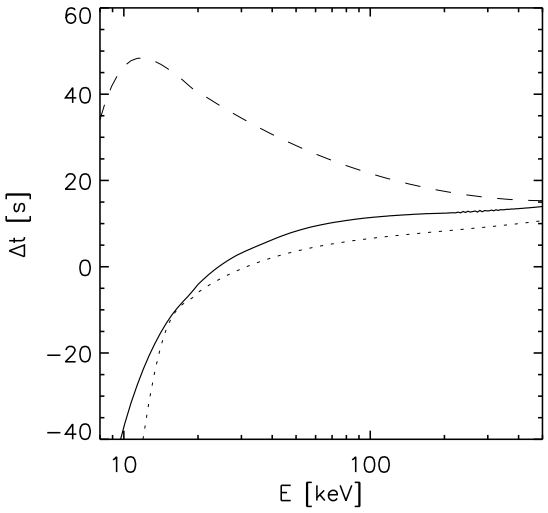


Figure 3.7: Difference of electron arrival times at $s = 1.07$ AU between the full diffusion model and free propagation, as functions of electron energy (solid line). The model results for pure pitch-angle diffusion (dashed line) and the run without whistler waves (dotted line) are also shown for comparison.

whistlers. This choice is somewhat arbitrary, and the wave spectrum might also vary in time. Thus, the effect of a variation of the wave power on the resulting electron delays needs to be investigated. This can be done by multiplying the wave spectrum by a given factor and re-running the full diffusion model.

Figure 3.8 shows the resulting electron delays at 1 AU for five different wave spectra, ranging from no wave power up to the five-fold power as compared to the results from Fig. 3.7. It is evident that the delays increase with increasing wave power, as one would expect for more efficient diffusion.

The energy dependence of the delays changes slightly. For low wave powers up to a two-fold increase, $\Delta t$ increases with increasing electron energy, but for the highest wave power this relation is reversed. So the degree to which the effects of pitch-angle diffusion and diffusion in the momentum coordinate compensate each other is not independent of energy. But even for the highest wave power, no strong energy dependence of $\Delta t$ is found.

The maximum delay found in this parametric study is less than 30 s, even for the highest wave intensity, and stays below 15 s for all other simulation runs.

## 3.3 Conclusions

In this chapter, the impact of scattering of solar energetic electrons due to resonant interaction with whistler waves in interplanetary space has been investigated. Since the quasi-linear diffusion equation appears to be dominated by the pitch-angle diffusion term, it seemed to be reasonable to simplify the model accordingly.

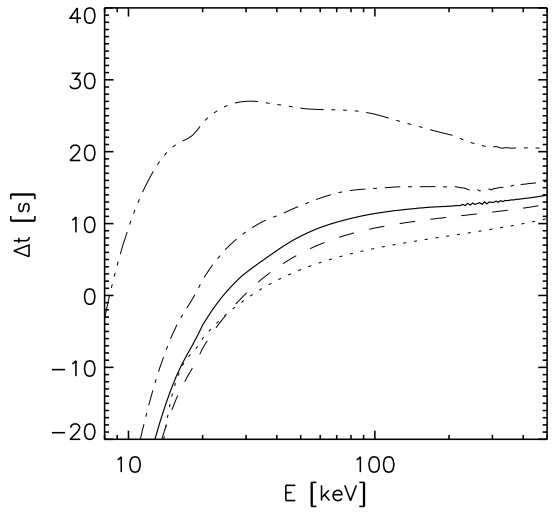


Figure 3.8: Difference of electron arrival times at $s = 1.07$ AU between the full diffusion model and free-propagation, as functions of electron energy (solid line). The results after multiplication of the whistler-wave spectrum with a factor of 0 (dotted line), 0.5 (dashed line), 2 (dash-dotted line), and 5 (dash-dot-dotted line) are also shown.

Pitch-angle scattering leads to a delay of electron arrival times as compared to the theoretical free-propagation time from the Sun up to 1 AU. The maximum delay found in this simulation is about 1 min. This is much less than the delays of between 10 min and 30 min that are reported in the literature. So this result already indicates that pitch-angle diffusion cannot explain delays of tens of minutes.

The simulated delay shows a strong energy dependence that is strongest for low energies of about 20 keV. This energy dependence can influence the derivation of release times and path lengths of the electrons. The resulting errors have been estimated as 20 s, which is also well below 10 min.

However, the pure pitch-angle diffusion model turned out to be oversimplified. Since more energetic, i.e. faster electrons arrive earlier at a given solar distance, interplanetary electron VDFs develop strong phase-space gradients. This leads to significant diffusion along the momentum coordinate, i.e. in energy, despite the low diffusion coefficient in the quasilinear equation. If more energetic electrons are scattered to lower energies in interplanetary space, this leads to an earlier increase of the spectral flux at this lower energy at any position further away from the Sun, e.g. at 1 AU.

So diffusion in the momentum coordinate leads to earlier electron arrival times compared to pure pitch-angle diffusion. This effect becomes clearly visible at energies of less than 20 keV. In this energy range, Coulomb collisions are not entirely negligible, although even keV solar wind electrons are still collision-free with mean free paths of the order of hundreds of AU. The effects of Coulomb diffusion on electrons in the energy range of a few keV is an interesting topic for future studies.

A simple estimate of the earlier electron arrival due to diffusion along the momentum coordinate

shows that this effect is of the same order of magnitude as the delay due to pitch-angle scattering. Thus, it has to be concluded that the assumption of pure pitch-angle scattering without any energy diffusion is not applicable. Instead, a full diffusion model is needed. The results obtained with the new model clearly demonstrate that these two effects indeed compensate each other. The resulting electron delays hardly differ from free-propagation times.

This provides a hint as to why analyses that are based on the assumption of free propagation yield good results, although non-negligible diffusion is present in interplanetary space. The maximum difference to free-propagation times found in a series of model runs with different wave power is below 30 s, even for the strongest diffusion.

All results presented here have been obtained with the same solar wind background model, and thus with the same whistler-wave phase speeds in interplanetary space. The wave speeds are always relatively small, of the order of electron thermal speeds, and the effect of the wave-particle interaction on an electron distribution is pitch-angle diffusion in the wave frame. Thus, energetic electrons will always experience strong pitch-angle scattering in the plasma frame, independent of the exact background conditions.

But this is not the case for the diffusion component along the momentum coordinate in the plasma frame. This component is proportional to the square of the wave phase-speed, see Eq. (2.5). Whistler wave phase speeds are characterized by the electron Alfvén speed $v_{\mathrm{A,e}} = B/\sqrt{\mu_0 N_\mathrm{e} m_\mathrm{e}}$. The stronger the magnetic field, and the lower the plasma density, the higher the phase speeds.

So the compensation between the delay due to pitch-angle diffusion and the early arrival due to momentum (or energy) diffusion depends on the solar wind conditions. But nevertheless, the pure pitch-angle diffusion model provides an upper limit on the delays of about 1 min.

The choice of the wave spectrum is somewhat arbitrary, but comparative runs with different wave intensities show that the delays do not increase beyond 30 s, even for the strongest whistler waves. So the main result of this model is that delays of 10 min and more cannot be caused by resonant interaction with whistler waves in interplanetary space, unless unrealistically high values for the whistler wave power are assumed.

# Chapter 4

# Formation of suprathermal electron distributions in the quiet solar corona

In the previous chapters it has been found that scattering of electrons by whistler waves in interplanetary space plays an important role in forming solar wind electron VDFs, and that it has significant influence on energetic electron propagation. The main effect of resonant interaction (2.4) of electrons with whistlers is pitch-angle scattering in the reference frame of the waves. The solar wind is a medium with relatively low whistler wave phase speeds. The maximum phase speed of whistlers is half the electron Alfvén speed, $v_{\mathrm{A,e}} = B/\sqrt{\mu_0 N_\mathrm{e} m_\mathrm{e}}$, and it is comparable to electron thermal speeds. So for energetic electrons there is little difference between the wave frame and the plasma frame, the whistlers just lead to pitch-angle scattering. This has already been concluded from Figure 2.3b, and has motivated the pure pitch-angle scattering model for flare electrons in the previous chapter.

This is different in the solar corona, where whistler wave phase speeds are much higher. For coronal conditions, typically $B = 10^{-3}\,\mathrm{T}$ and $N_\mathrm{e} = 10^{14}\,\mathrm{m}^{-3}$, this results in an electron Alfvén speed of $v_{\mathrm{A,e}} = 0.3\,c$. This corresponds to the case depicted in Figure 2.3a. The whistler waves tend to form "kinetic shells" in the electron VDF that strongly deviate from a Maxwellian distribution.

This enables electrons to considerably gain energy due to pitch-angle diffusion in the wave frame along the kinetic shells. As an example, take an electron at the position $(v_\parallel = -0.06\,c, v_\perp = 0)$ in velocity space. It can reach the position $(v_\parallel = 0, v_\perp = 0.2\,c)$ along its shell. This corresponds to an energy increase from 0.9 keV to 10 keV. This acceleration mechanism was studied by Vocks & Mann (2003) in order to find an explanation for the observed presence of suprathermal electron VDFs in the solar wind even under quiet conditions without any flare activity (Lin, 1998; Maksimovic et al., 1997), as presented in chapter 2.2.

The lower electron energy change due to resonant interaction with whistlers in regions with lower $v_{\mathrm{A,e}}$, i.e. towards the solar wind, has the consequence that this acceleration mechanism can only be efficient in the solar corona. But if the fluxes of electrons in the range of several keV, as observed in the solar wind, are generated already in the corona, two questions arise:

- Is there enough whistler wave energy in the corona to provide significant suprathermal electron fluxes?

- Can electrons that have been accelerated in the corona escape into interplanetary space without being relaxed due to Coulomb collisions?

These questions have been addressed by Vocks & Mann (2003).

## 4.1 Sufficient wave energy in the corona?

An efficient electron acceleration by resonant interaction with whistler waves in the solar corona requires a sufficient supply of wave energy there. Is it reasonable to assume that these waves exist? To address this question, one can have a look at the problem of solar coronal heating. Resonant interaction between ions and ion cyclotron waves is discussed as heating mechanism (Cranmer et al., 1999; Vocks, 2002; Vocks & Marsch, 2002). In these models, the waves are generated in the transition region, with frequencies well below all ion cyclotron frequencies. They propagate upwards in the corona, until they reach a height where the cyclotron frequencies have decreased so far that the waves come into resonance with ions.

Ion cyclotron waves are left-hand polarized waves. If the waves are generated with frequencies well below local ion cyclotron frequencies, there should be no preference for left-hand polarized over right-hand polarized, i.e. whistler, waves. These whistler waves are not affected by resonances with ions, but the electron resonance condition (2.7) applies to them. Of course, the electron cyclotron frequency is about a factor $m_\mathrm{p}/m_\mathrm{e}$ higher than the proton cyclotron frequency. Normally, the wave spectral energy decreases with increasing frequency, e.g. with a power law $\propto \omega^{-\alpha}$, with a spectral coefficient $\alpha \geq 1$. Thus, much less wave energy is available for electrons than for protons or other coronal ions.

However, the ion cyclotron waves provide enough energy to heat the ions to coronal temperatures. Heavy ions can reach temperatures of several $10^6$ K (Kohl et al., 1998). For the electrons, such a strong heating is neither needed in coronal models, nor observationally supported (Esser & Edgar, 2000). Only some suprathermal electrons are to be accelerated to higher energies. It is indeed possible to accelerate suprathermal electrons without the bulk of thermal electrons absorbing all the wave power and being heated. This is due to the decrease of the magnetic field, and thus the electron cyclotron frequency, with height in a magnetic structure that is open towards the solar wind, e.g. a coronal funnel. The mechanism is based on "frequency sweeping" (Tu & Marsch, 1997) that also plays an important role in the heating of coronal ions with ion cyclotron waves (Vocks, 2002).

Figure 4.1 illustrates the frequency sweeping mechanism. On the ordinate, the spatial coordinate $s$ along a coronal magnetic field line is displayed, and thus the height above the transition region. The abscissa represents the frequency coordinate. For two heights $s_1$ and $s_2$, electron VDFs in the range $v_\parallel < 0$ are sketched. For $v_\parallel < 0$, it is possible to replace the velocity coordinate by the resonance frequency in a unique way, using Eqs. (2.7) and (2.8). The higher the absolute value of $v_\parallel < 0$ is, the lower is the resonance frequency. The VDFs are restricted to the local electron cyclotron frequency $\Omega_\mathrm{e}$, with $\Omega_\mathrm{e}$ corresponding to $v_\parallel = 0$. Now a whistler wave is considered, with a given frequency $\omega$, that propagates anti-sunwards through the corona. In the low corona, at $s_1$, its frequency is much below the electron cyclotron frequency, thus it cannot interact resonantly with any electrons. But at a larger height, $s_2$, the electron cyclotron frequency has decreased,

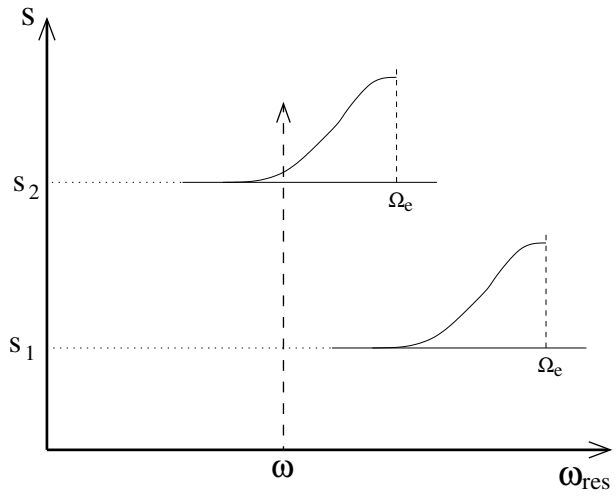


Figure 4.1: Sketch of the frequency sweeping mechanism. A wave with frequency $\omega$ propagates upwards in the corona and comes into resonance with electrons at a certain height. For further details, see text.

and the wave frequency can fulfill the resonance conditions with some electrons. These are those electrons with the highest $v_{\|}$ directed towards the sun. These electrons can gain energy from the wave in the way described above.

But the thermal bulk of electrons still does not fulfill the resonance condition with the frequency $\omega$ at this height. So the bulk cannot absorb the wave while suprathermal electrons already are being accelerated. Due to this preferred interaction of suprathermal electrons ($v_{\|} < 0$) with whistler waves, electron acceleration in the corona is possible, in spite of the smaller energy supply compared to that provided to the ions.

## 4.2 Can suprathermal tails escape from the corona?

While resonant interaction with whistler waves can add energy to an electron VDF and deform it from a Maxwellian, Coulomb collisions have the tendency to relax it towards a Maxwellian. Since the efficiency of Coulomb collisions depends on the density, the relaxation will be most effective in the low corona where the acceleration mechanism is also working. Furthermore, the $v^{-3}$ dependence of Coulomb collision frequencies implies that thermal cores of VDFs can be dominated by Coulomb collisions, whereas electrons in the suprathermal tails can cross the corona without being relaxed.

To estimate if suprathermal tails of electron VDFs can escape into the solar wind after their formation in the corona, the relaxation process of a non-Maxwellian electron VDF under typical coronal conditions is studied. For this test, a homogenous proton-electron plasma without external forces is set up, with particle number density $N_e = 10^{14}\,\mathrm{m}^{-3}$ and temperature $T = 10^6\,\mathrm{K}$. As an initial condition with suprathermal tails, the electron VDF is defined as a kappa distribution (2.3) with $\kappa = 5$. Such kappa distributions are discussed for solar coronal electron VDFs by Scudder (1992b). The electron kinetic model is used to calculate the temporal evolution of the electron

VDF caused by Coulomb collisions with both protons and other electrons. Any wave-electron interaction is not considered here.

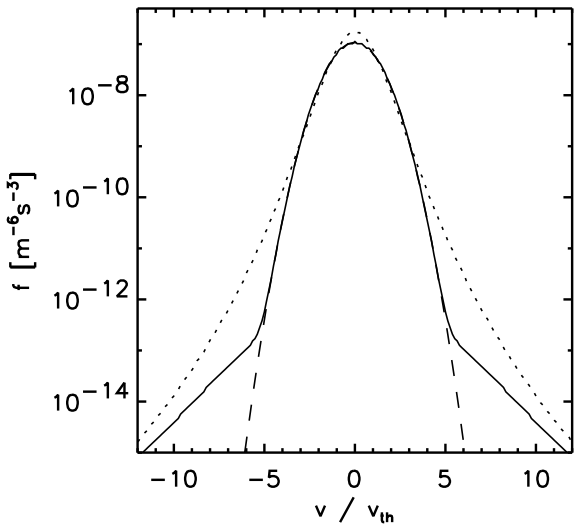


Figure 4.2: Relaxation of a kappa electron VDF under typical coronal conditions. Shown are the electron VDF after a simulation time of 5 s (solid line), the initial distribution with $\kappa = 5$ (dotted line), and a Maxwellian VDF (dashed line).

Figure 4.2 shows the electron VDF after a simulation time of 5 s. The initial kappa distribution and a Maxwellian representing the thermal equilibrium state are also plotted. It can clearly be seen that electrons with a speed $v < 5\,v_{\rm th}$, with $v_{\rm th}$ being the thermal velocity, have already relaxed towards the Maxwellian VDF. But at higher speeds, the suprathermal tails of the kappa distribution are still present. The relatively sharp transition between these two parts is due to the $v^{-3}$ dependence of Coulomb collision frequencies that implies a strong variation of relaxation times with speed. The choice of 5 s simulation time is arbitrary, but has the following reason: Electrons with $v = 5\,v_{\rm th}$ can pass a distance of $10^5$ km, i.e. two coronal pressure scale heights, within these 5 s. Electrons with higher speeds traverse this distance in shorter times, and from the simulation result shown in Fig. 4.2 it follows that these times are shorter than their relaxation times. Thus, their VDFs can preserve their shape during the passage through the corona.

The result of this simple simulation run leads to the conclusion that electrons with at least $v = 5\,v_{\rm th}$ can traverse the corona from the coronal base towards interplanetary space without significant relaxation due to Coulomb collisions. This speed corresponds to an electron energy of 1.1 keV. Thus, this test confirms the finding of Pierrard et al. (1999) that a coronal origin of the suprathermal tails, measured in the solar wind at energies of several keV, is possible.

## 4.3 Suprathermal electron production in the solar corona

Vocks & Mann (2003) have investigated the coronal production of suprathermal electrons by adding resonant electron-whistler interaction to the Boltzmann-Vlasov equation (1.7). However,

only waves propagating away from the Sun were considered in this model, but not the whistler wave turbulence in interplanetary space. The resonance condition (2.7) and the whistler wave dispersion relation (2.8) dictate that only electrons moving towards the Sun, $v_{\parallel} < 0$, can interact with these waves. So there is no wave scattering of anti-sunward moving electrons here.

### 4.3.1 The model

The kinetic model is based on the non-relativistic Boltzmann-Vlasov equation (2.13) using velocity coordinates $(v_{\parallel}, v_{\perp})$. The simulation box extends from the transition region between chromosphere and corona up to 1 AU into interplanetary space. For the velocity coordinates, a rectangular grid in the $v_{\parallel}$ - $v_{\perp}$ - plane is used. The step sizes $\Delta v_{\parallel}$, $\Delta v_{\perp}$ are equidistant with $\Delta v_{\parallel} = \Delta v_{\perp} = 2000\,\mathrm{km\,s^{-1}}$. This is a considerable fraction of the electron thermal speed $v_{\mathrm{th}} = 3900\,\mathrm{km\,s^{-1}}$ at a temperature $T = 10^6\,\mathrm{K}$, but the objective of this simulation run is not a detailed study of the thermal bulk of the electron VDF, but to cover an energy range of 10 keV, which corresponds to $15\,v_{\mathrm{th}}$.

At each spatial position $s_i$ in the simulation box, the wave spectrum is calculated. The frequency coordinate is discretized with an equidistant spacing on a logarithmic scale, i.e. frequency positions $\omega_j = \omega_0 \exp(j/N_w)$, with $\omega_0$ being a reference frequency and $N_w$ the number of grid points per logarithmic decade. The frequency coordinate covers the resonance frequencies of electrons at all grid points inside the whole simulation box, from the lowest frequencies of electrons with high $v_{\parallel} < 0$ in interplanetary space to the electron cyclotron frequency, $\Omega_{\mathrm{e}}$, at the lower boundary where the resonance frequency is highest.

The whistler waves in the model plasma enter the the simulation box at the lower bound with a given power law spectrum $\propto k^{-1}$. Only waves propagating parallel to the background magnetic field are considered, thus $k_{\parallel} = k$. The waves propagate upwards inside the simulation box, and their spectrum evolves due to the changes of wave phase speed and magnetic flux tube geometry, and due to the resonant absorption by electrons.

The solar wind background model is the same as in chapter 2.4.2. As initial and boundary conditions for the electron VDF in the simulation box, a kappa distribution (2.3) with electron density and temperature corresponding to the background model has been chosen. The ideal choice would have been a Maxwellian, since a kappa distribution has power-law suprathermal tails $\propto p^{-2(\kappa+1)}$. But for higher electron energies a Maxwellian shows steep phase-space gradients that cause numerical problems. A kappa distribution turns into a Maxwellian in the limit $\kappa \to \infty$. For this study, a very high value of $\kappa = 200$ is used. This is much higher than the kappa values well below 10 in the models of Scudder (1992a) or in the fits to Ulysses observations by Maksimovic et al. (1997), and provides a VDF that is very close to a Maxwellian. The use of such a distribution as boundary condition ensures that for keV energies hardly any electrons are injected into the simulation box, and therefore avoids numerical artifacts.

### 4.3.2 Locations of electron acceleration

The electron acceleration mechanism by resonant absorption of whistler waves is most effective in regions where the electron Alfvén speed is high. With the solar wind background model at

hand, it is possible to plot the electron Alfvén speed as a function of the height coordinate in the simulation box:

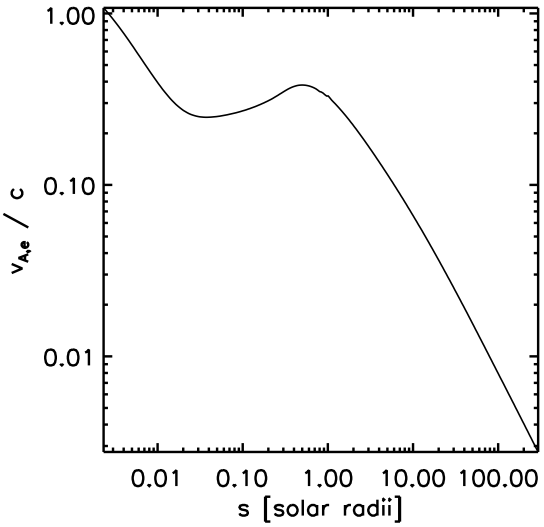


Figure 4.3: Electron Alfvén speed as derived from the background solar wind model. Note that the spatial coordinate, $s$, denotes the height above the coronal base along the magnetic flux tube under consideration, not the distance from the solar center.

Figure 4.3 displays this electron Alfvén speed. The highest values $v_{\mathrm{A,e}} \approx c$ are reached in the coronal funnel close to the lower bound, due to the strong magnetic field there. In the low corona, $v_{\mathrm{A,e}}$ decreases rapidly and reaches a local minimum of $v_{\mathrm{A,e}} = 0.25\,c$ at a height of $s = 0.03\,R_\odot$ above the coronal base. Then it increases towards a local maximum of $v_{\mathrm{A,e}} = 0.4\,c$ at $s = 0.5\,R_\odot$. After this maximum, $v_{\mathrm{A,e}}$ strongly decreases towards interplanetary space. The reason for this non-monotonic course is the decrease of both the magnetic field, $B$, and the electron number density, $N_\mathrm{e}$, with height, as can be seen from Fig. 2.5a,b. The decrease of $B$ tends to decrease $v_{\mathrm{A,e}}$, while the decrease of $N_\mathrm{e}$ increases it.

This figure leads to the conclusion that the electron acceleration is indeed strongest in the corona. Towards interplanetary space, $v_{\mathrm{A,e}}/c$ takes very small values, and the electron acceleration ceases.

### 4.3.3 Results

The Boltzmann-Vlasov equation (1.7) is now solved iteratively, starting with the near-Maxwellian $\kappa = 200$ initial condition. The velocity coordinates of the simulation box cover speeds of up to $5.6 \cdot 10^7\,\mathrm{km\,s^{-1}}$, that corresponds to an electron energy of 9.6 keV.

The whistler waves enter the simulation box at the lower bound with a spectrum $\propto k^{-1}$. The spectral wave energy is chosen in such a way that it is coincident in the MHD regime with the spectrum of ion cyclotron waves that has been used in the coronal heating model of Vocks & Marsch (2002).

**Coronal electron VDFs**

Starting with the initial condition, the evolution of the electron VDF has been calculated over a simulation time of $t_{\mathrm{sim}} = 2 \cdot 10^4$ s. After this time, the simulation has reached a final steady state, and the electron VDF does not change any more.

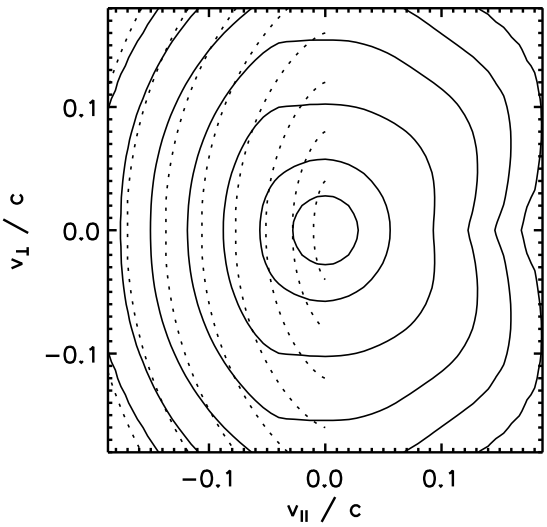


Figure 4.4: Isolines of the electron VDF at the height $s = 0.014\,R_\odot$ (solid lines), and kinetic shells due to resonant electron - whistler wave interaction (dotted lines).

Figure 4.4 shows the resulting electron VDF at a height of $s = 9500\,\mathrm{km}$ ($0.014\,R_\odot$). Again, the isolines are chosen in such a way that they would form equidistant circles for a Maxwellian VDF. The kinetic model here is based on velocity components $(v_\parallel, v_\perp)$. But due to gyrotropy of the electron VDF, these are actually cylindrical coordinates that imply $v_\perp \geq 0$. Negative $v_\perp$ have been added by the symmetry condition $f(v_\parallel, -v_\perp) = f(v_\parallel, v_\perp)$, to make the plots more readable. The position $s = 0.014\,R_\odot$ is located in the rapidly expanding coronal funnel, where the electron Alfvén speed $v_{\mathrm{A,e}} = 0.34\,c$ is still relatively high. This situation corresponds to Fig. 2.3a. In Fig. 4.4, the kinetic shells that the whistler waves try to establish, are also plotted as dotted lines.

The plot reveals a temperature anisotropy $T_\perp > T_\parallel$. In the range $v_\parallel < 0$ strong deformations of the isolines can be observed. They are in good coincidence with the kinetic shells, especially at higher negative $v_\parallel$. Thus, the simulation result shows the expected effect of resonant interaction between electrons and whistler waves. It can be seen that electrons are accelerated from relatively small, negative $v_\parallel$ to high $v_\perp$.

On the anti-sunward side, electrons can be seen that have been accelerated at lower heights, and have been transported to $v_\parallel > 0$ by the mirror force that influences the electrons in the diverging magnetic field geometry of the coronal funnel.

In the range of lower, sunwards electron speeds, $v_\parallel < 0$, the deformation of the isolines ceases. This has several reasons. First, the Coulomb collision frequency increases with $v^{-3}$ as the velocity decreases. So Coulomb collisions are more capable of relaxing the electron VDF there. Another reason can be derived from the resonance condition, equation (2.7). The resonance frequency

approaches $\Omega_e$ for $v_\parallel \to 0$. The dispersion relation (2.8) yields decreasing wave phase speeds for $\omega_{res} \to \Omega_e$. Thus the acceleration mechanism becomes less efficient. A further reason for the undisturbed isolines at $v_\parallel \to 0$ can be seen from the spectrum of the whistler waves:

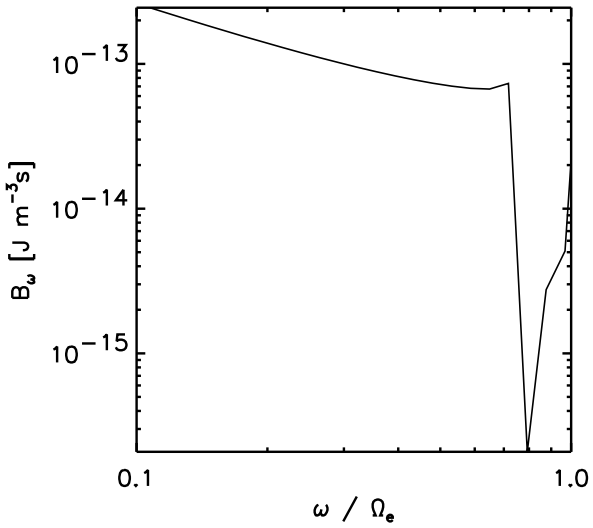


Figure 4.5: Wave spectral energy density at the height $s = 0.014\,R_\odot$.

Figure 4.5 displays the wave spectral energy density at $s = 0.014\,R_\odot$. The absorption of the waves by the electrons is clearly visible. Since the resonance frequencies of electrons with $v_\parallel \to 0$ is close to $\Omega_e$, hardly any wave energy is left over for them. But electrons with higher negative $v_\parallel$ can interact with waves that have not been absorbed at lower heights. This is the essence of the frequency sweeping mechanism. The increase of the wave spectral energy density in the vicinity of $\Omega_e$ is due the abovementioned weaker wave absorption of electrons with $v_\parallel$ close to 0. It is insignificant for the kinetic results at $s = 0.014\,R_\odot$. Since the waves propagate upwards, and $\Omega_e$ decreases with height, it does also not affect the kinetic results higher up in the simulation box.

Figure 4.6 shows the electron VDF at a larger height $s = 0.028\,R_\odot$ in the corona. The VDF is now closer to a Maxwellian, the deformation of isolines at negative $v_\parallel$ is much weaker. The reason for this can be seen from Fig. 4.3, the electron Alfvén speed passes its local minimum at $s = 0.028\,R_\odot$. The electron acceleration process is less efficient here, the pitch-angle diffusion of electrons by the interaction with whistler waves results in smaller deviations from a Maxwellian VDF.

With further growing height, the electron Alfvén speed increases again, and the electron acceleration becomes more efficient. Figure 4.7 shows the electron VDF at $s = 1.06\,R_\odot$, where the electron Alfvén speed reaches its local maximum, see Fig. 4.3. In figure 4.7 the pitch angle diffusion caused by the waves is evident again. It is also clearly visible that the electrons that have been accelerated at lower heights are focused into the anti-sunward direction. This is due to the mirror force related to the large-scale decrease of the coronal magnetic field, and the lack of a turbulent whistler wave spectrum in the solar corona and wind that could provide pitch-angle scattering to these electrons.

Note the high density of isolines on the anti-sunward side around $v_\parallel \approx -0.05\,c$ and low $v_\perp$. This is related to a strong gradient of the electron VDF. The onset of the drop of the electron VDF with

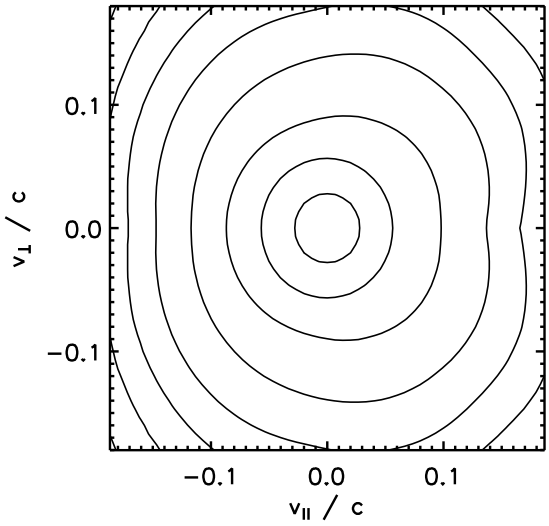


Figure 4.6: Isolines of the electron VDF at the height $s = 0.028\,R_\odot$.

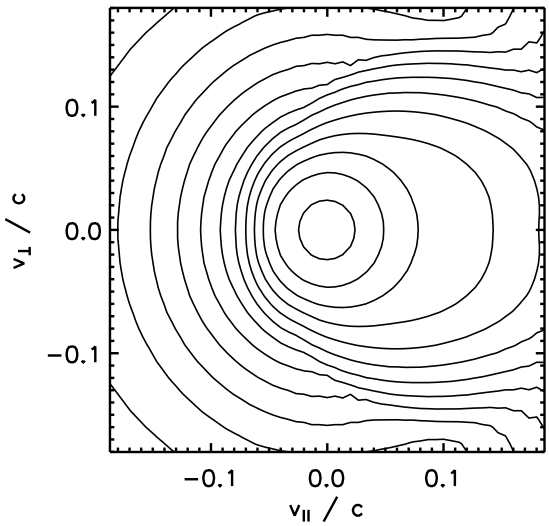


Figure 4.7: Isolines of the electron VDF at the height $s = 1.06\,R_\odot$.

increasing negative $v_\parallel$ is located at approximately $v_\parallel = 0.04\,c$. This corresponds to an electron energy of 408 eV. This is in good coincidence with the electrostatic potential drop within the simulation box from $s = 1.06\,R_\odot$ to the upper boundary. This potential drop is calculated from the charge-separation electric field in the background fluid model and amounts to 381 V. Electrons with higher energies can escape into interplanetary space through the upper boundary. They do not return, so there is a lack of electrons moving sunwards with $|v_\parallel| > 0.04\,c$. So the results display a typical feature of exospheric models. The electrons inside the simulation box in this velocity range have entered it through the upper boundary condition.

Figure 4.8 displays the further evolution of the electron VDF in the nascent solar wind at $s =$

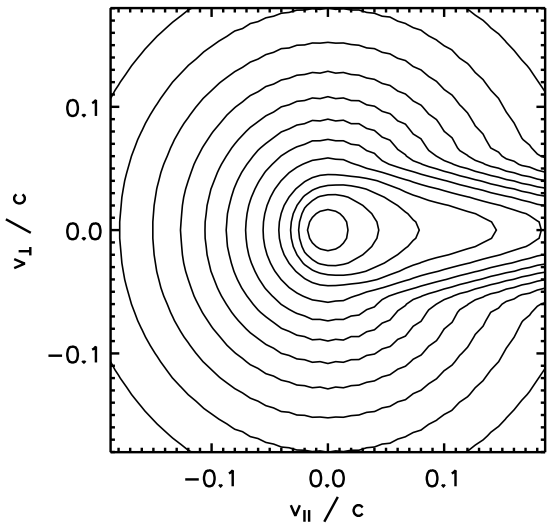


Figure 4.8: Isolines of the electron VDF at the height $s = 6.5\,R_\odot$.

$6.5\,R_\odot$. On the anti-sunward side, the mirror force focuses the accelerated electrons to a narrow pitch angle range. This feature resembles the "strahl" in solar wind observations (Lin, 1974; Rosenbauer et al., 1977; Pilipp et al., 1987). On the sunward side, the temperature anisotropy due to the electron - whistler interaction is still visible.

The focusing of the "strahl" due to mirror force continues towards interplanetary space, leading to the extremely narrow beam shown in figure 2.2. However, the aim of this model run was not realistic solar wind electron VDFs, but to investigate the production of suprathermal electrons in the corona.

### Suprathermal electron fluxes

Spacecraft instruments do not measure the electron VDFs directly, but electron fluxes as a function of energy. Often, the fluxes are averaged over all spatial directions to yield better statistics, especially at higher energies, like in Lin (1998). Thus, to compare the calculated electron VDFs with solar wind data, it is reasonable to derive the fluxes from the VDFs.

The number density of electrons within a speed interval $\mathrm{d}v$ and a solid angle interval $\mathrm{d}\Omega$ around a velocity vector $\vec{v}$, with absolute value $v = |\vec{v}|$, is $f(\vec{v})v^2\mathrm{d}v\,\mathrm{d}\Omega$. The flux of these electrons through a detector with unit aperture area can then be calculated by multiplication with $v$:

$$f(\vec{v})\,v^3\mathrm{d}v\,\mathrm{d}\Omega$$

Changing from the velocity coordinate, $v$, to the energy coordinate, $E$, by $E = v^2 m_\mathrm{e}/2$, yields a spectral electron flux that still depends on the direction, $\vec{e} = \vec{v}/v$:

$$\phi(E,\vec{e}) = f(\vec{v} = \sqrt{2E/m_\mathrm{e}}\cdot\vec{e})v^2/m_\mathrm{e}\,\mathrm{d}\Omega \tag{4.1}$$

Averaging over all directions can be done in spherical coordinates, $(\theta,\phi)$, by $\mathrm{d}\Omega = \mathrm{d}\phi\,\sin\theta\,\mathrm{d}\theta$. The integration over the gyro-angle, $\phi$, is trivial due to the gyrotropy of the electron VDF $f(\vec{v})$. It

just yields a factor $2\pi$. For the pitch angle, $\theta$, the relation $\cos\theta = v_\parallel/v$ holds. This simplifies the integration over all $\theta$ by

$$\int_0^\pi \sin\theta \, \mathrm{d}\theta = \int_{-1}^{1} \mathrm{d}(\cos\theta) = \frac{1}{v} \int_{-v}^{v} \mathrm{d}v_\parallel$$

Thus, the spectral electron flux $\phi(E)$ can be calculated as:

$$\phi(E) = \frac{2\pi v}{m_\mathrm{e}} \int_{-v}^{v} f\left(v_\parallel, v_\perp = \sqrt{v^2 - v_\parallel^2}\right) \mathrm{d}v_\parallel \qquad \text{with} \quad v = \sqrt{2E/m_\mathrm{e}} \tag{4.2}$$

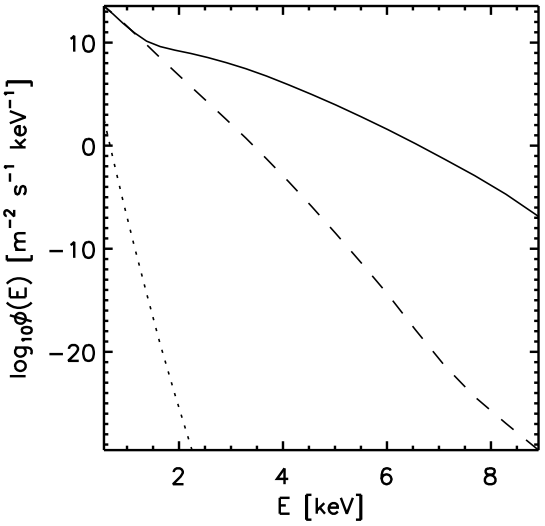


Figure 4.9: Electron fluxes at $s = 1$ AU that are derived from the model results presented in this chapter (solid line), from a comparative study without whistler waves (dashed line), and from the initial $\kappa = 200$ distribution (dotted line).

Figure 4.9 shows the electron fluxes at $s = 1$ AU (solid line) that have been calculated from the model VDF. For comparison, the fluxes derived from the initial kappa distribution at $s = 1$ AU are also plotted (dotted line). It can be seen that the fluxes are enhanced by several orders of magnitude. The very small high-energy tails of the initial $\kappa = 200$ distribution play no role here.

But the whistler waves are not the only effect that forms the electron VDF in the model plasma. The background conditions that provide densities, temperatures, and the magnetic field are inhomogeneous and change with height. This also deforms the VDF. To identify the effect of the whistler waves on the electron flux, the whole numerical study has been repeated without any whistler wave activity. The resulting spectral electron flux is plotted as the dashed line in Fig. 4.9. It is also significantly enhanced compared to the initial condition. The reason for this is the "strahl" that also forms in such a simulation run. In the solar corona, the temperature is higher and the electron VDF is thus broader than in the solar wind (Fig. 2.5d). Suprathermal electrons of sufficient energy can escape the electrostatic potential and are focused towards the anti-solar direction due to the mirror force in the large-scale decrease of the magnetic field. This process is independent of the presence of whistler waves (Lie-Svendsen et al., 1997).

But a comparison of the fluxes resulting from the otherwise identical simulation runs with and without whistler waves shows that the wave action increases the electron flux in the energy range of a few keV by several orders of magnitude. The electron spectrum is much flatter than in the run without whistlers. At energies below 1.5 keV the fluxes resulting from the simulation runs with and without whistler waves hardly differ. Such energies correspond to electron velocities $v < 0.075\,c$. This is in coincidence with the finding that the wave effect on the electrons ceases at low speed, as it has been discussed above for the low corona, $s = 0.014\,R_\odot$, see Figs. 4.4 and 4.5.

These results demonstrate that the resonant interaction with whistler waves in the corona can increase the flux of solar wind electrons in the keV energy range significantly. The model includes no transient events like flare activity or shock waves that produce suprathermal electrons. **The calculations show that the quiet solar corona is capable of producing high-energetic electrons.**

A more quantitative look at Fig. 4.9 shows that the fluxes at low energies around 1 keV are in very good agreement with the observations of Lin (1998) under quiet conditions. At higher energies, the whistler waves enhance the electron fluxes considerably compared to the model run without waves, but the slope of the spectrum is still steeper than that observed in the solar wind. However, the tendency is clear. One possible reason for the steeper slope are the high-velocity boundaries of the simulation box. The computational domain is restricted to 10 keV, so boundary effects might influence the results at energies of several keV.

Another aspect is the location of the lower boundary of the simulation box. Its position is in the transition region at a temperature of $7.3 \cdot 10^5$ K, within the coronal funnel. Below this border, in the transition region, the magnetic field strongly increases towards the sun. This leads to high values of the electron Alfvén speed, see Fig. 4.3. But the simulation box cannot extend further down, since the stronger Coulomb collisions would require smaller time steps in the simulation, driving up computer costs too much.

## 4.4 Suprathermal electrons in a closed loop

The solar wind results in the previous section show enhanced fluxes of suprathermal electrons, and thus demonstrate that the quiet solar corona is capable of generating them even under quiet solar conditions without any flare activity. But these model calculations did not investigate either whether kappa-like electron VDFs form, as observed in the solar wind (Maksimovic et al., 1997), or how the suprathermal tails are shaped. Furthermore, the model was restricted to low electron energies of a few keV. So a more comprehensive analysis of the electron acceleration mechanism by resonant interaction with whistler waves in the corona requires an extension of the model to higher energies. In the solar wind, suprathermal electrons are observed up to 100 keV (Lin, 1998), so this energy range should be covered.

Vocks & Mann (2008) provide a more detailed analysis of the evolution of coronal electron VDFs under the influence of resonant interaction with whistler waves. The previous model calculations were limited to electron energies of less than 10 keV, but now suprathermal electron energies of several tens of keV are to be studied. Furthermore, in order to avoid any influence of the high-energy border of the computational domain on the simulation results, the simulation box should cover energies of the order of 100 keV. The model calculations start, as in the previous section,

with a kappa distribution. The kappa value had to be lowered to $\kappa = 80$ in order to avoid too steep phase-space gradients at energies of 100 keV. This still ensures that it is indeed the whistlers, and not some initial or boundary condition, that leads to suprathermal tail formation. The geometry of the simulation box is a closed coronal loop, and not a coronal hole as in the previous section which is open towards interplanetary space. The closed geometry has the advantage that it enables a study focused on the physical processes in the corona, without the need to either define an upper boundary condition for the electron VDF in the corona, or extend the model into the solar wind.

Electron energies of the order of 100 keV require the relativistic form (1.6, 1.7) of the Boltzmann-Vlasov equation. The momentum coordinates can be described as $(p_\parallel, p_\perp)$, the components parallel and perpendicular to the magnetic field, respectively. But such a coordinate system becomes problematic for higher electron energies and momenta, $p$. This is because the wave-electron interaction and the mirror force in a diverging magnetic field geometry both change the pitch-angles of electrons. If the simulation box is a rectangle in $(p_\parallel, p_\perp)$ space, then lines of constant $p$ cross both the high-$p_\parallel$ and high-$p_\perp$ boundaries of the box for some high $p$. As a consequence, this section of the simulation box is strongly influenced by both boundaries, and the boundary conditions applied there. This can cause numerical instabilities and renders the simulation results useless. The use of $p$ and the pitch-angle, $\theta$, as momentum-space coordinates overcomes this issue.

### 4.4.1 Coronal loop background model

The Coulomb collisions and the whistler wave phase speeds depend on plasma background parameters like densities, drift velocities, and temperatures of both ions and electrons. These parameters, as well as the magnetic field geometry, have to be provided by a background model for the coronal loop under study.

The background model does not change during a simulation run, so electrons that are described by the Boltzmann-Vlasov equation (1.7) can be regarded as test particles. The solution of Eq. (1.7) again requires the definition of an initial condition for the electron VDF, which is a $\kappa = 80$ distribution with the same density, drift velocity, and temperature as in the background model. This is close to a Maxwellian and avoids any artificial insertion of suprathermal electrons into the simulation box.

The coronal loop geometry, i.e. the magnetic field, $B(s)$, and the angle $\psi(s)$ between $\vec{B}$ and the direction normal to the solar surface, is calculated from photospheric potential magnetic field extrapolation, e.g. (Seehafer, 1978; Sakurai, 1982). The same algorithm is used as in (Aurass et al., 2005). A photospheric dataset from the 28 Oct 2003 has been used to reconstruct the loop, but for a region that is separated from the active region that produced the strong flare events of that day.

The "upper" and "lower" boundaries of the simulation box, with respect to the spatial coordinate along the loop, $s$, are located in the transition region. The temperature inside the loop is set to $1.4 \cdot 10^6$ K for both electrons and protons, and the particle number densities at the coronal base is $N_\mathrm{e} = N_\mathrm{p} = 2 \cdot 10^{15}\,\mathrm{m}^{-3}$. Inside the loop, the pressure is hydrostatic, and there is no plasma flow along the loop.

Figure 4.10 shows the loop height, magnetic field, particle number densities of both electrons and protons, and electron Alfvén speeds as functions of $s$. The total length of the loop is 210 Mm,

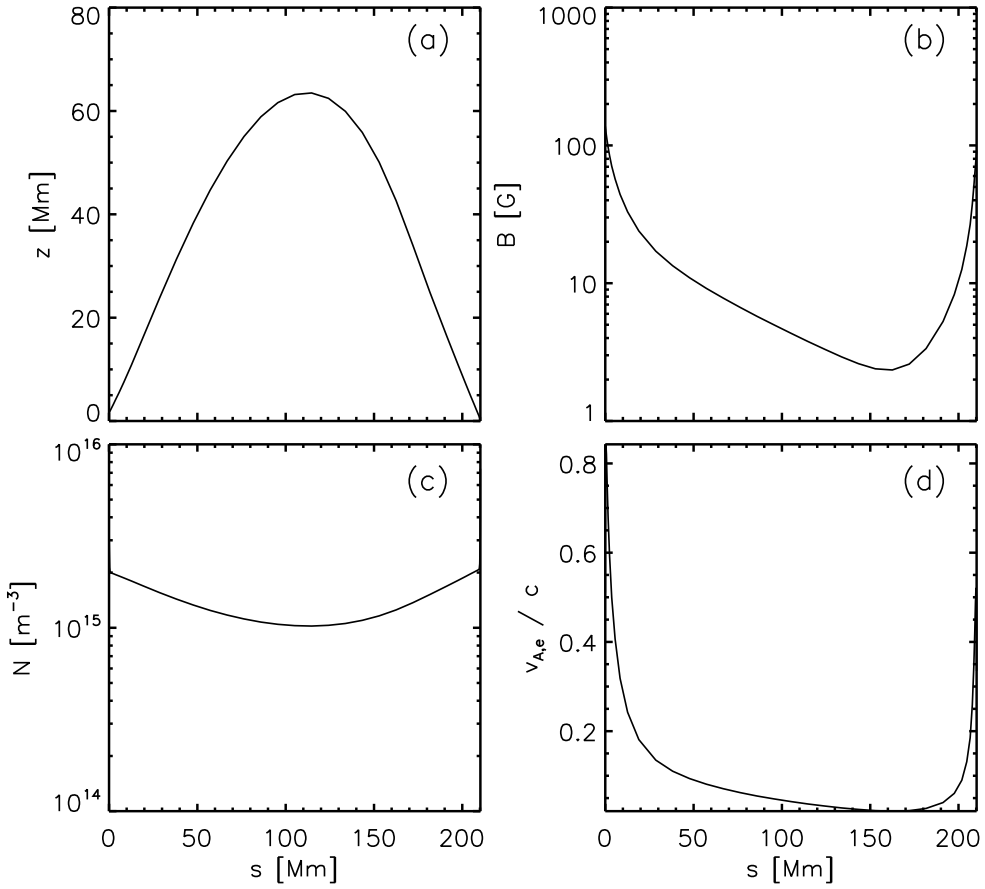


Figure 4.10: The coronal loop background model. Shown are loop height, $z$, magnetic field, $B$, particle number densities, $N$, and electron Alfvén speed normalized to the speed of light, $v_{\mathrm{A,e}}/c$, all as functions of the spatial coordinate, $s$, along the loop. Electrons and protons have the same densities, $N = N_{\mathrm{e}} = N_{\mathrm{p}}$.

its maximum height is $z_{max} = 63.5$ Mm at $s = 115$ Mm. The strong density gradients of the transition region are barely visible at the $s = 0$ Mm and $s = 210$ Mm edges of the plot. The borders of the simulation box are located at a temperature of $4 \cdot 10^5$ K. It clearly can be seen that the loop is not symmetric. The magnetic field at the loop footpoints is $B(s = 0\,\mathrm{Mm}) = 137$ G and $B(s = 210\,\mathrm{Mm}) = 92$ G, and the minimum value of $B$ is not reached at the loop top, but at $s = 162$ Mm with $B_{min} = 2.3$ G. This also leads to high values of the electron Alfvén speed near the footpoints, while the speed near the magnetic field minimum is very small. Therefore, electron acceleration will be strongest close to the loop footpoints.

The whistler waves enter the coronal loop at both footpoints. Again, the waves are assumed to be a high-frequency tail of the same wave spectrum that is discussed for coronal heating, e.g. (Cranmer et al., 1999; Vocks & Marsch, 2002). The ion cyclotron waves discussed in these papers are left-hand polarized, but it is reasonable to assume that not only left-hand, but also right-hand polarized waves, i.e. whistler waves, are present. The whistler wave spectrum is set up as a power law, $\mathcal{B}_\omega \propto \omega^{-\alpha}$, with an index $\alpha = 1.3$. The total wave power is chosen in such a way that the total energy content of the full spectrum, from the 5-minute oscillations up to the electron cyclotron frequency, corresponds to a wave energy flux density of 275 $\mathrm{Wm}^{-2}$ (Hollweg, 2006). The waves

propagate into the loop, and the evolution of the wave spectrum due to the spatial variation of the phase speed and the absorption by electrons is considered in the model.

### 4.4.2 Resulting coronal loop electron VDFs

The Boltzmann-Vlasov equation (1.7) is now solved numerically for this loop. The electron momentum range covers values up to $p_{\max} = 0.6\, m_e\, c$, that corresponds to energies of up to 100 keV. The total simulation time is 80 s. This allows electrons with thermal speed to travel from one footpoint to the other one, and back. So the time is long enough to let the numerical system "forget" its initial condition, and indeed it is found to have reached a final steady state.

The results presented here have been obtained with a grid spacing of the momentum coordinate of $\Delta p = 2000\,\mathrm{km\,s^{-1}}\, m_e$. This is less than half of the thermal speed inside the loop, and fine enough to study the formation of suprathermal VDF tails. In order to ensure that the results shown here are indeed based on whistler-electron interaction, and are not an artifact due to numerical diffusion in momentum space, the calculation has been re-run with a finer $\Delta p = 1500\,\mathrm{km\,s^{-1}}\, m_e$, since numerical diffusion strongly depends on $\Delta p$. The results do not differ significantly.

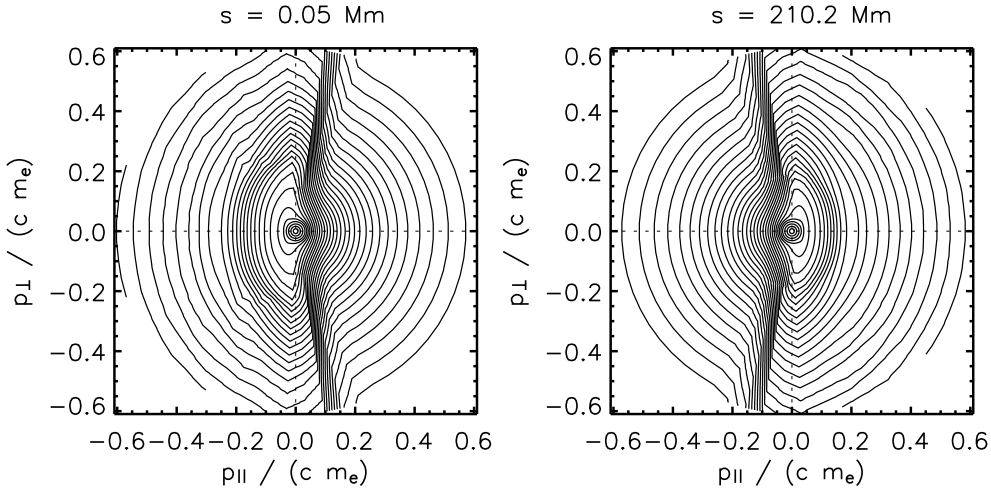


Figure 4.11: Isoline plots of the electron VDFs close to the loop footpoints at $s = 0\,\mathrm{Mm}$ (left) and $s = 210\,\mathrm{Mm}$ (right). The region with high isoline density marks the boundary between electrons that have entered the loop at the footpoints and electrons that have been mirrored inside the loop, as described in the text.

Figure 4.11 shows the resulting electron VDFs at both loop footpoints, $s = 0\,\mathrm{Mm}$ (left) and $s = 210\,\mathrm{Mm}$ (right). The VDFs clearly demonstrate the effect of the resonant interaction with whistler waves. At $s = 0\,\mathrm{Mm}$, the waves enter the loop with wavenumbers $k_\parallel > 0$, and from the resonance condition, Eq. (2.7), it follows that only electrons with $p_\parallel < 0$ can interact with these waves. The deformation of the VDF towards "kinetic shells" in this momentum range can clearly be seen in the left part of the figure. At the $s = 210\,\mathrm{Mm}$ footpoint, the whistler waves entering the loop propagate towards smaller $s$. Thus, $k_\parallel < 0$, and the resonance condition requires $p_\parallel > 0$. The corresponding "kinetic shells" can be seen in the right part of Fig. 4.11. These deformations of initially isotropic VDFs demonstrate that electron acceleration is happening due

to the high wave phase speeds near the footpoints. As an example, electrons are diffused from ($p_\parallel = -0.15\, m_\mathrm{e}\, c, p_\perp = 0$) to ($p_\parallel = 0, p_\perp = 0.3\, m_\mathrm{e}\, c$), which corresponds to a 4-fold increase of energy.

The sections of electron momentum space that are not affected by the whistler-electron interaction, i.e. $p_\parallel > 0$ at $s = 0$ Mm and $p_\parallel < 0$ at $s = 210$ Mm, respectively, are populated by electrons that just have entered the loop through the footpoint boundaries. Their VDFs are close to the kappa distributions, with $\kappa = 80$ and transition region densities and temperatures, that are used as spatial boundary conditions of the simulation box, and do not show pronounced suprathermal tails. As a consequence, a strong phase-space density gradient develops at the boundary between these two electron populations, that can be seen as regions with high isoline density in the figure.

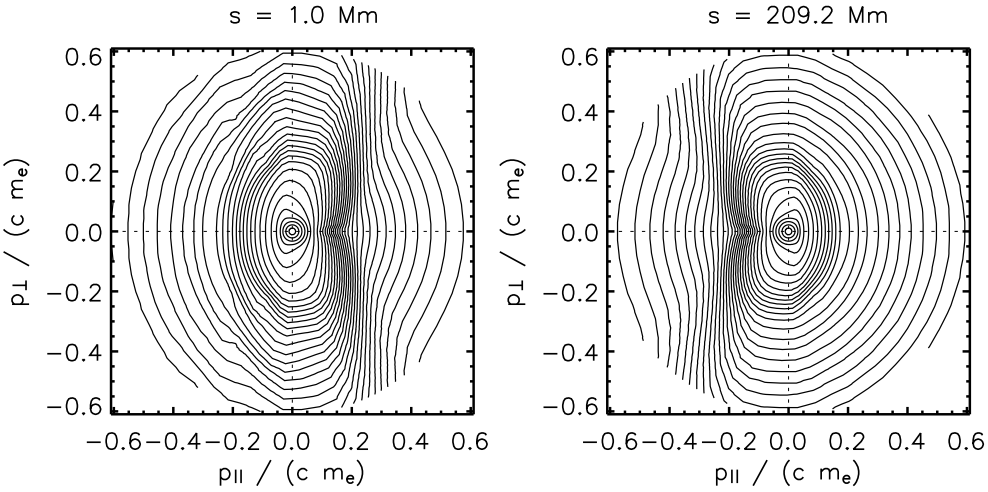


Figure 4.12: Isoline plots of the electron VDFs at heights of 1 Mm above the loop footpoints. The spacing of the isolines is the same is in Fig. 4.11, and the high isoline density between electrons trapped inside the loop and having entered it through the footpoints is still visible.

Inside the coronal loop, the VDFs evolve further. Figure 4.12 shows that with increasing height above the transition region, the mirror force in the widening loop (cf. Fig. 4.10 (b)) pushes the electrons towards positive $p_\parallel$ ($s = 1$ Mm) and negative $p_\parallel$ ($s = 209$ Mm), respectively. These suprathermal electrons then propagate towards the loop top region. Due to this process, some loss-cone structures form that potentially could lead to whistler-wave excitation (Scharer & Trivelpiece, 1967; Mann et al., 1989). But considering such plasma instabilities is beyond the scope of the model calculations presented here. The phase-space densities of the loss-cone regions are also relatively low, so that the wave growth would be quite weak.

At the loop top, the electron VDF is more isotropic, as shown in figure 4.13. This is expected, since the suprathermal electrons from both footpoints reach this region. The whistler-electron interaction weakens here, since the magnetic field and thus the electron gyrofrequency barely changes with $s$, and most of the spectral wave power has been absorbed further down, closer to the footpoints. Furthermore, the effect of the whistlers is reduced to pure pitch-angle diffusion due to the low wave phase speeds, see Fig. 4.10 (d). The VDF is not perfectly symmetric, since the loop itself is asymmetric, see Fig. 4.10.

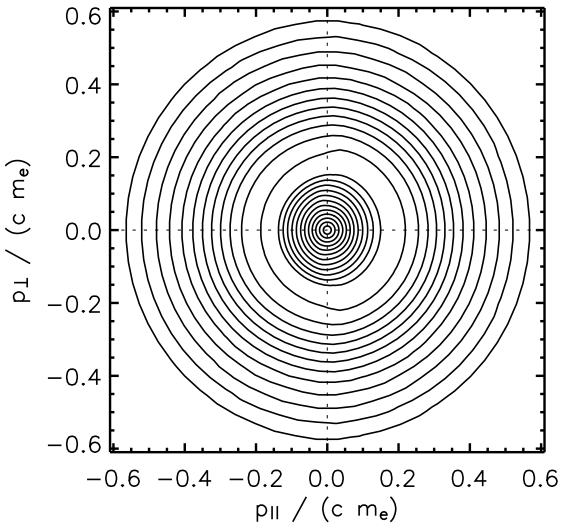


Figure 4.13: Isoline plots of the electron VDFs at the loop top, $s = 115\,\mathrm{Mm}$. The spacing of the isolines is the same is in Fig. 4.11.

Two components of the electron VDF can be distinguished, a thermal core and an extended halo. The thermal core forms due to the strong Coulomb collisions in the dense coronal loop, along with the weak local wave-electron interaction. The temperature of the core equals that of the background model, $T = 1.4 \cdot 10^6\,\mathrm{K}$. So it is apparent that a halo of suprathermal electrons has formed, in excess of the thermal population.

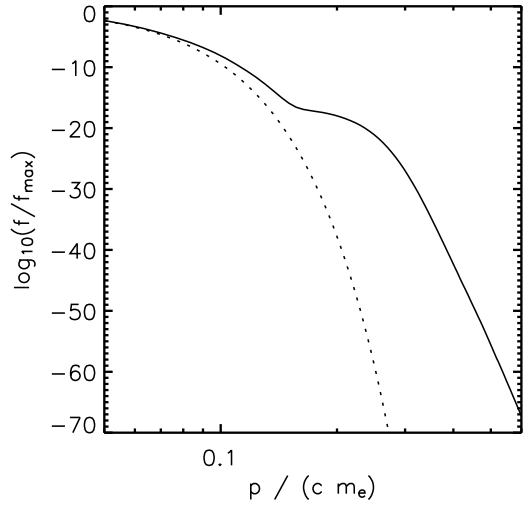


Figure 4.14: Pitch-angle average electron VDF at the loop top, $s = 115\,\mathrm{Mm}$. The dotted line is a Maxwellian VDF with the same density and temperature.

For a further study of this suprathermal tail, Figure 4.14 shows a plot of the pitch-angle average electron VDF at the loop top, $s = 115\,\mathrm{Mm}$. The thermal core and the deviation of the halo distribution from a Maxwellian VDF are clearly visible. The thermal core extends up to an electron

momentum of about $p = 0.15\, m_e\, c$, that corresponds to an energy of 6 keV. This is a consequence of the high density in the coronal loop. Above this energy, the halo distribution becomes visible. It can roughly be approximated by a double power-law. At low energies, up to about $p = 0.2\, m_e\, c$ (10 keV), it is relatively flat, but at higher energies up to the full 100 keV, it becomes steeper.

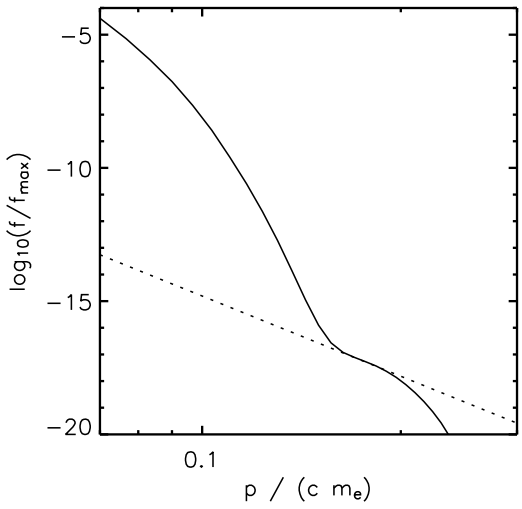


Figure 4.15: Pitch-angle average electron VDF at the loop top, $s = 115$ Mm, for low energies. The dotted line is a power-law, $p^{-\alpha}$, with $\alpha = 10$.

The energy range below 10 keV is of special interest, since it allows for a direct comparison of the simulation results with the solar wind measurements of Maksimovic et al. (1997), although the model does not include a mechanism for electron release from the loop into interplanetary space. Figure 4.15 shows the pitch-angle average VDF at lower energies, together with a power-law fit, $p^{-\alpha}$, with index $\alpha = 10$. According to the definition of the kappa function, Eq. (2.3), this corresponds to a $\kappa = 4$ for suprathermal energies. The fit of the electron VDF by the power law is very good in the momentum range $p = 0.15 - 0.2\, m_e\, c$, that just corresponds to energies of 6 – 10 keV, which are relevant for the comparison with solar wind measurements.

### The influence of the high-$p$ boundary condition

For low energies of less than 10 keV, the suprathermal electron halo distribution starts with a relatively small power-law index. But for higher energies above 10 keV, the slope of the VDF becomes steeper, as shown in Figs. 4.14 and 4.15. This raises the question of why the suprathermal electron production becomes less efficient at higher energies.

There are several potential reasons for the relatively low number of electrons at higher energies. One is the acceleration mechanism through diffusion along "kinetic shells" itself. The energy gain associated with the electron transport from low $p_\parallel$ to high $p_\perp$ depends on the ratio between the wave phase speed, $v_{\rm ph}$, and electron speed, $v$. A high $v_{\rm ph}/v$ leads to a strong energy gain, but with increasing electron energy, $v$ also increases, and the electron energy gain decreases. On the other hand, electrons in the coronal loop are reflected by the mirror force in the converging magnetic field geometry at the footpoints. The faster they are, the more acceleration cycles they can undergo

in a given time interval. But electrons with sufficiently small pitch-angles are not mirrored, and escape from the loop into the transition region and chromosphere. So faster electrons can have a higher escape rate.

But not only the footpoints, i.e. the spatial boundaries of the simulation box, can influence the results. At a first glance, an electron energy range of 100 keV in the simulation seems to be enough for a discussion of the electron VDF at 10 keV. But from the "kinetic shells" in Figs. 4.11 and 4.12 it can be seen that the high-$p$ boundary of the simulation box does influence the deep interior of the box. The pitch-angle diffusion in the wave reference frame transports electrons from relatively low $p_{\parallel} = 0.2\, m_\mathrm{e}\, c$ towards the high-$p$ boundary at a pitch-angle close to $\pi/2$. So the boundary condition, which is an extrapolation based on the $\kappa = 80$ distribution also used as initial condition, is directly connected to the results for 10 keV electrons. Therefore, it is necessary to extend the range of $p$ to avoid the boundary influence.

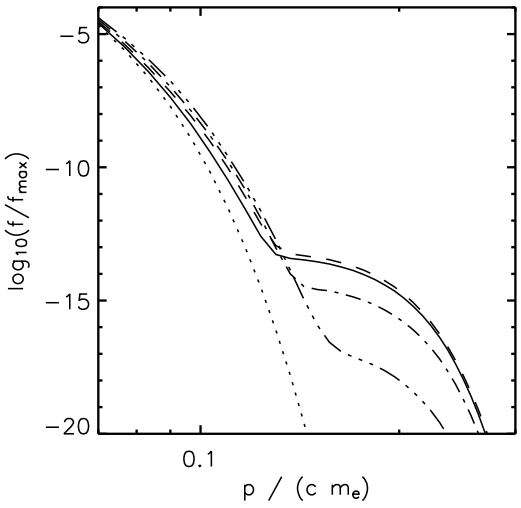


Figure 4.16: Pitch-angle average electron VDF at the loop top, $s = 115\,\mathrm{Mm}$, for low energies. Shown are the results of simulation runs with $p_\mathrm{max}/(m_\mathrm{e}\, c) = 0.6$ (dash-dot-dot-dotted line), 0.8 (dash-dotted line), 1.0 (dashed line), and 1.2 (solid line), as well as a Maxwellian VDF (dotted line).

Figure 4.16 shows the resulting pitch-angle average electron VDFs at the loop top for multiple simulation runs with subsequently increased momentum ranges, $p_\mathrm{max}/(m_\mathrm{e}\, c)$. For the lowest value of 0.6, the plot is identical to Fig. 4.15. An increase to $p_\mathrm{max}/(m_\mathrm{e}\, c) = 0.8$ leads to a strong increase of the VDF in the range $p/(m_\mathrm{e}\, c) = 0.15 - 0.25$. This is in agreement with the finding that the "kinetic shells" at the loop footpoints connect $p = 0.2\, m_\mathrm{e}\, c$ with the high$-p$ boundary for $p_\mathrm{max}/(m_\mathrm{e}\, c) = 0.6$. The extension of the momentum range alleviates the influence of the boundary condition considerably. A further extension to $p_\mathrm{max}/(m_\mathrm{e}\, c) = 1.0$ leads to an additional increase of the electron VDF around $p = 0.2\, m_\mathrm{e}\, c$ , but then it saturates. Increasing $p_\mathrm{max}$ further to $1.2\, m_\mathrm{e}\, c$ does not influence the result. So it can be concluded that the simulation results for suprathermal electrons are not affected by the boundary condition any longer for this high momentum range, which corresponds to a maximum energy of 287 keV in the model.

A comparison of the model results for $p_\mathrm{max}/(m_\mathrm{e}\, c) = 0.6$ and $p_\mathrm{max}/(m_\mathrm{e}\, c) = 1.2$ in Fig. 4.16 shows

that the former strongly underestimates the production of suprathermal electrons in the loop. So the analysis of the suprathermal population from the previous sub-section should be repeated for the $p_{\max}/(m_e\,c) = 1.2$ result.

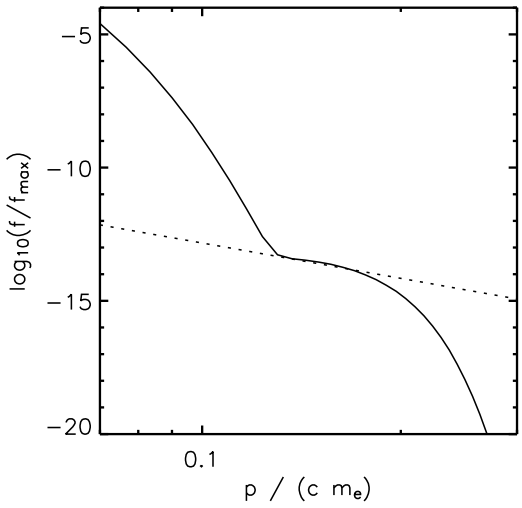


Figure 4.17: Pitch-angle average electron VDF at the loop top, $s = 115\,\mathrm{Mm}$, for low energies. The dotted line is a power-law, $p^{-\alpha}$ with $\alpha = 4.4$.

Figure 4.17 shows this electron VDF in the same style as in Fig. 4.15, together with a power-law fit, $p^{-\alpha}$. But here the index can be set as low as $\alpha = 4.4$. This is so low that it is not possible to calculate a corresponding $\kappa$. The term $(2\kappa - 3)$ in the definition of the kappa distribution, Eq. (2.3), requires that $\kappa > 1.5$. For high $p$, the kappa distribution turns into a power-law $p^{-2(\kappa+1)}$, so that a minimum $\alpha = 5$ is required for the definition of a corresponding $\kappa$. So this calculation demonstrates that the electron VDF can develop suprathermal tails which are even stronger than can be described by a $\kappa$ distribution.

The suprathermal electron population is now much stronger as compared to Fig. 4.15, with higher phase-space densities, and it separates from the thermal core at a lower momentum $p = 0.13\,m_e\,c$, which corresponds to an electron energy of about 4 keV. So the power-law fit is now valid for the energy range of 4 - 10 keV, as compared to 6 - 10 keV in Fig. 4.15. The previous calculation did indeed underestimate the suprathermal electron production.

Figure 4.18 shows the same electron VDF as in Fig. 4.17, together with a fit by a combined Maxwellian and kappa distribution. The Maxwellian VDF corresponds to the background plasma in the loop. The kappa distribution has a $\kappa = 1.8$ and a density of $3 \cdot 10^{-9}$ times the background electron density, $N_e$. This is $N_\kappa = 3 \cdot 10^6\,\mathrm{m}^{-3}$ in absolute units. The thermal momentum, $p_{\mathrm{th}}$, of the kappa component corresponds to the background temperature, $T = 1.4 \cdot 10^6\,\mathrm{K}$, but the fit is very insensitive to this parameter.

This fit of the loop VDF with a combined core and kappa distribution resembles the solar wind analysis of (Maksimovic et al., 1997). The low kappa value is in good agreement with their results. But the electron energies where the kappa component becomes apparent are much higher here. This is due the strong Coulomb collisions in the dense coronal loop. Electrons with energies below 4 keV are quickly thermalized. The kink of the VDF at $p = 0.13\,m_e\,c$ clearly shows that

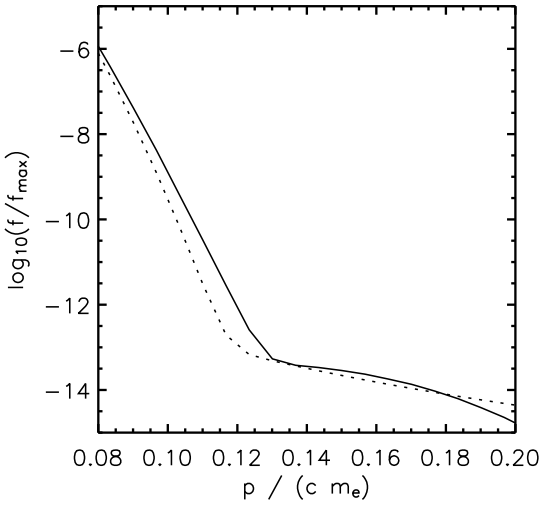


Figure 4.18: Pitch-angle average electron VDF at the loop top, $s = 115\,\mathrm{Mm}$, for low energies. The dotted line is a Maxwellian + kappa distribution with $\kappa = 1.8$ and density $N_\kappa = 3 \cdot 10^{-9}\, N_\mathrm{e}$.

the slower electrons are collision dominated. The diffusion of electrons in momentum space due to the Coulomb collisions can also be responsible for the deviation between the electron VDF and the combined core + kappa distribution around $p = 0.12\, m_\mathrm{e}\, c$.

**Results with coronal funnels**

The electrons in the model calculations presented here are confined to a coronal loop. If they approach a loop footpoint, they experience the mirror force in the converging magnetic field towards the footpoint. The force arises from the conservation of magnetic momentum. If the initial pitch-angle is sufficiently large, the electrons are reflected back into the loop. But electrons with small enough pitch-angles can escape from the loop towards the transition region and chromosphere.

So the quality of the magnetic confinement determines what fraction of the electrons can escape the loop at each footpoint. The pitch-angle diffusion of the electrons due to resonant interaction with whistler waves complicates the picture, since it modifies the magnetic momentum, but generally the electrons are better confined if the magnetic field converges more strongly at the footpoints.

The electron pitch-angle diffusion in the wave reference frame, and the associated electron acceleration, can be seen in Fig. 4.11. Electrons with sufficiently large pitch-angles are mirrored back into the loop, as it is evident from Fig. 4.12, that shows the electron VDFs at a slightly larger height in the loop. These electrons move through the interior of the loop, and eventually approach the other footpoint. There they interact with the whistler waves entering at this footpoint. The diffusion and the mirror force in the given magnetic field geometry again determine what fraction of them is reflected back into the loop, and what fraction leaves the loop. Those electrons that are reflected move back towards the first footpoint, where they are again mirrored and diffused, and so on. So electrons can undergo multiple such cycles, and be accelerated at each footpoint

passage. This leads to an enhancement of the suprathermal tails, but eventually an equilibrium with the losses due to imperfect magnetic confinement is reached.

This raises the question of what influence the quality of the confinement, i.e. the increase of the magnetic field toward the loop footpoints, has on the simulation results. To investigate this, the simulation is run again for a loop where the magnetic field increases within 4 Mm of the footpoints to the two-fold value as compared to the previously used loop geometry.

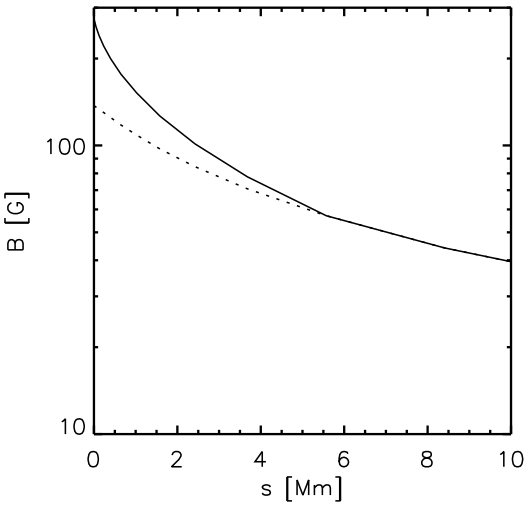


Figure 4.19: Modified loop geometry as a function of the spatial coordinate, $s$, along the loop. Shown are the new, stronger magnetic field, $B$ (solid line), and the previously used model (dashed line). The same increase of the magnetic field is applied to the $s = 210$ Mm footpoint.

Figure 4.19 shows the new magnetic field as a function of the loop length, $s$. For the $s = 210$ Mm footpoint, a similar increase of $B$ is applied. Such a rapid increase of the magnetic field towards the transition region resembles a coronal funnel.

Figure 4.20 displays the simulation result for the new magnetic field geometry in the same style as in Fig. 4.17, together with a power-law fit, $p^{-\alpha}$. The better magnetic confinement in this simulation run might lead to the assumption that the suprathermal tails of the electron VDFs are stronger here. But the somewhat surprising result is that they are actually weaker. The power-law index has increased to a steeper $\alpha = 6.4$, and the overall phase space density is lower.

The fit of the new electron VDF to a combined Maxwellian and kappa distribution in figure 4.21 confirms this finding. The value $\kappa = 2.2$ is in agreement with the power-law index $\alpha = 6.4$ from above, since $\alpha = 2(\kappa + 1)$ according to the definition of the kappa distribution, Eq. (2.3). The density of the kappa population is only $10^{-10}$ of the total electron density, $N_\mathrm{e}$. This is much less than the $3 \cdot 10^{-9}\, N_\mathrm{e}$ in the previous simulation run.

So it has to be concluded that the the electron acceleration is now much less efficient despite the better confinement of the electrons in the loop. The reason for this is the higher magnetic field, $B$, close to the loop footpoints. A higher $B$ leads to a higher electron cyclotron frequency, $\Omega_e = eB/m_\mathrm{e}$, and thus the resonance frequencies of the electrons are also higher. Since the whistler waves enter the simulation box with a power-law spectrum $\propto \omega^{-1.3}$, there is less wave

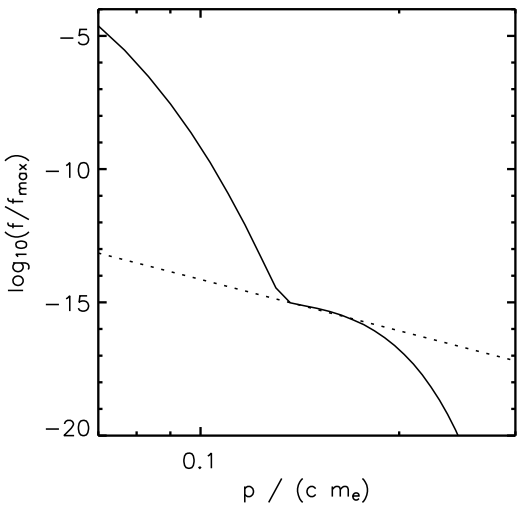


Figure 4.20: Pitch-angle average electron VDF at the loop top, $s = 115\,\mathrm{Mm}$, for low energies. The dotted line is a power-law, $p^{-\alpha}$ with $\alpha = 6.4$.

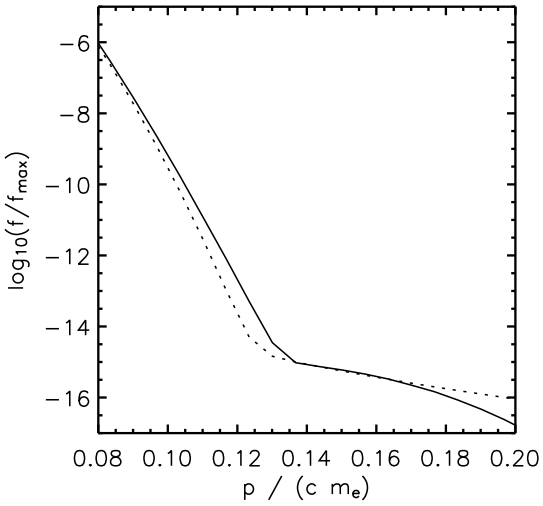


Figure 4.21: Pitch-angle average electron VDF at the loop top, $s = 115\,\mathrm{Mm}$, for low energies. The dotted line is a Maxwellian + kappa distribution with $\kappa = 2.2$ and density $N_\kappa = 1 \cdot 10^{-10}\,N_\mathrm{e}$.

power available for electron acceleration close to the loop footpoints. But the region close to the footpoints is where the wave phase speeds are highest, and high phase speeds are necessary for an efficient electron acceleration from low $p_\perp$ to high $p_\parallel$, cf. Fig. 4.11. The minimum value of $B$ in the simulation box has not been changed, so in total there is not less wave energy available for absorption by the electrons in this simulation run than before, but most of it is shifted now further away from the footpoints, where the acceleration is less effective.

So the weaker electron acceleration cancels the effect of the better magnetic confinement of the suprathermal electrons inside the loop. The reason for the weak acceleration is the strong magnetic field at the footpoints, that leads to low wave power at electron resonance frequencies. To

overcome this issue, another simulation run has been performed, with $B$ reduced by half. So now the magnetic field at the footpoints is the same as in the first simulations, Fig. 4.10 (a), and it is reduced to half of its original value inside the loop. But this simulation also resulted in a lower number of suprathermal electrons as compared to Figs. 4.17 and 4.18. This is due to the reduced wave phase speeds, that decrease rapidly close to the footpoints as $B$ is reduced. Lower wave speeds mean less efficient electron acceleration, and even at low heights in the loop the electrons are pitch-angle scattered, but hardly accelerated.

These studies show that the suprathermal electron population inside the loop does depend on the loop geometry. But there is no simple recipe for strong suprathermal tails. Their formation is a compromise between efficient acceleration, that requires a strong magnetic field for high whistler wave phase-speeds, and available wave power, that requires a not too strong $B$ due the power-law nature of the wave spectrum, which provides less wave energy for higher frequencies.

## 4.5 Conclusions

The simulation results presented in this chapter show that the quiet solar corona is capable of producing pronounced suprathermal tails in electron VDFs. In the open magnetic field geometry of a coronal funnel, the resonant interaction of electrons with whistler waves is capable of increasing the flux of suprathermal electrons in the keV energy range by several orders of magnitude, see Fig. 4.9. This model from chapter 4.3 does not include a mechanism that scatters electrons in interplanetary space, they are just focused into the anti-sunward direction.

But electrons are scattered in interplanetary space, as it has been demonstrated in chapter 2.4. In this kinetic solar wind model, electrons are pitch-angle scattered out of the strahl into an isotropic halo that includes the sunward direction. So suprathermal electrons from the corona can return to the Sun, and undergo multiple acceleration cycles. But a kinetic model run for this would require very long simulation times, with computer costs way too high. In order to study this effect, the kinetic model has been run in chapter 4.4 for the closed volume of a coronal loop. The results as shown above demonstrate that the whistler waves produce suprathermal tails that can be fitted by a power-law, $\propto p^{-\alpha}$. The index $\alpha$ can be as small as $\alpha < 3$. For energies up to 10 keV, the coronal electron VDF can also be fitted with a combined Maxwellian + kappa distribution, with $\kappa$ as small as $\kappa = 1.8$.

The magnetic field geometry also influences the efficiency of suprathermal electron production. Since the whistler waves are assumed to have a power-law spectrum with less energy at higher frequencies, the wave power depends on the electron resonance frequencies, that are close to the gyrofrequency. So a stronger magnetic field leads to less efficient electron acceleration. Furthermore, the variation of the magnetic field inside the simulation box determines the range of the whistler wave spectrum that can provide energy for electron acceleration, and a stronger variation leads to better confinement of the suprathermal electrons in the coronal loop. So a strong variation should lead to more suprathermal electrons. But it has been found that this is not necessarily the case. Either a strong magnetic field at the footpoints leads to less efficient acceleration there, or a low field inside the loop turns the “kinetic shell” formation into mere pitch-angle scattering without much electron acceleration. So a modification of the loop geometry simultaneously has opposite effects on the electron acceleration.

This work focuses on the acceleration process of suprathermal electrons, starting from a nearly Maxwellian VDF. Therefore, a closed volume of coronal plasma is studied. But what are the consequences of these results for solar wind electron VDFs?

Electrons in the fast solar wind originate from open magnetic field geometries like the coronal funnel in chapter 2.4.2, but magnetically closed regions in the corona are the sources of the slow solar wind. Maksimovic et al. (1997) have found pronounced kappa tails not only in fast, but also in slow solar wind electron VDFs. So the simulation results are in agreement with observations so far, although the model does not include any mechanism for releasing suprathermal electrons from the loop into interplanetary space. But no magnetic confinement is perfect, although the details of the escape mechanism can influence the relation between the VDFs of the electrons in a closed loop and of those that escape into the solar corona. As a rough comparison between model calculations and observations, take the density of suprathermal electrons in the model loop, which has been found to be $N_\kappa = 3 \cdot 10^6\,\mathrm{m}^{-3}$. If this population could propagate freely into the solar wind, and if the electron flux is conserved along a magnetic field line, then the electron density would be reduced by the expansion factor of the magnetic field from the corona into the solar wind. The magnetic field in the model corona is 2.4 G, and a typical solar wind magnetic field is $5\,\mathrm{nT} = 5 \cdot 10^{-5}\,\mathrm{G}$. Thus, the solar wind suprathermal electron density would be $60\,\mathrm{m}^{-3}$. This is much less than the $10^5\,\mathrm{m}^{-3}$ found by Maksimovic et al. (1997), but in the dense model loop all electrons with energies below 4 keV are thermalized quickly by Coulomb collisions. This leads to a reduction of the suprathermal electron population in the dense loop studied here.

For electron energies above 10 keV, the electron VDF deviates from the power-law and falls off more rapidly, as can be seen in Figs. 4.17 and 4.20. So the superhalo component of solar wind electron VDFs, as observed by Lin (1998), is not produced here and must have a different origin. The study on flare electron propagation in chapter 3.2.3 leads to the conclusion that these are energetic electrons from flares that stay in the heliosphere for days. The reason for the low number of suprathermal electrons in the range of a few tens of keV found here lies in the velocity dependence of the acceleration mechanism. The efficiency of the acceleration by diffusion along "kinetic shells" depends on the ratio between the wave phase speed, $v_{\mathrm{ph}}$, and electron speed, $v$. As $v$ is increased, this ratio declines, and the diffusion process resembles more and more pure pitch-angle diffusion without much energy gain for the electrons. More wave power does not change the result very much either. As soon as the electron VDF has reached a kinetic shell form, see Fig. 4.11, the acceleration mechanism is saturated. The resulting electron energy spectrum is determined by the electron movement along the loop, together with the spatial variation of the wave phase speeds, and thus of the "kinetic shells". So the loop and magnetic field geometry does influence the details of the result, but the qualitative picture with less efficient acceleration at higher energies is quite robust.

**The main result of this chapter is that the quiet solar corona is capable of producing suprathermal electrons even without any flare activity. The whistler waves responsible for that are the high-frequency tail of a spectrum that is also discussed for coronal heating. Therefore, coronal heating, solar wind acceleration, and production of suprathermal electrons are based on a common mechanism. Since other stars than the Sun also have hot coronae, this is a significant finding for solar-stellar connections.**

# Part II

# Plasma waves and instabilities

# Chapter 5

# Plasma wave growth and damping rates

In the first part of the thesis a kinetic model for electrons in the solar corona and wind has been presented. The model is based on a numerical solution of the Boltzmann-Vlasov equation, including diffusion terms describing the resonant interaction of electrons with whistler waves. The results of this model are electron velocity distribution functions (VDFs) that describe the phase-space density of electrons. The interaction with whistlers shapes the electron VDFs, but the effect of the electrons on the waves has only been considered in the models investigating suprathermal electron production by means of an energy balance that yielded wave absorption rates.

The electron VDFs resulting from the kinetic model can strongly deviate from a simple Maxwellian VDF. A Maxwellian is the VDF with maximum entropy for a given electron density and temperature. So electrons with a non-Maxwellian VDF can not only absorb plasma waves, but could also provide free energy for wave growth. Such microscopic plasma instabilities play an important role in space and laboratory plasmas and are the subject of the second part of this thesis.

## 5.1 Complex dispersion relation and wave growth rates

The starting point for an investigation of plasma instabilities is the calculation of wave growth or damping rates for a given electron VDF. Since electron energies of several tens of keV are to be considered during solar flares, a relativistic description of the electrons is necessary, see e.g. (Melrose, 1980).

### 5.1.1 Dispersion function and growth rates

The wave growth/damping rate, $\gamma$, is described as the imaginary part of the complex frequency

$$\omega = \omega_r + i\gamma \tag{5.1}$$

with $\omega_r$ being the real part of the frequency, and $i^2 = -1$. For a plane wave setup involving a factor $\exp(-i\omega t)$, a negative $\gamma$ corresponds to wave damping and a positive one to wave growth.

Matsuda & Smith (1992) have developed a code for calculating the complex frequency, $\omega$, that aims for a direct solution of the dispersion relation

$$D(\omega, \vec{k}) = 0 \tag{5.2}$$

for a given wave vector, $\vec{k}$. $D(\omega, \vec{k})$ is the plasma dispersion function. The dispersion relation yields both the wave frequency, $\omega_\mathrm{r}$, and the growth rate, $\gamma$.

This method is based on finding a solution of the dispersion relation by varying $\omega$ for a given $\vec{k}$. Matsuda & Smith (1992) apply their program on highly unstable plasmas with $\gamma \approx 10^{-3}\ \Omega_\mathrm{e}$, where $\Omega_\mathrm{e} = eB/m_\mathrm{e}$ is the electron cyclotron frequency in the magnetic field $B$.

In astrophysical plasmas, however, wave growth rates are often found to be much smaller, e.g. $10^{-8}\ \Omega_\mathrm{e}$ as shown below. In such a case, the order-of-magnitude difference between $\gamma$ and a wave frequency near the electron cyclotron frequency is dangerously close to the limited numerical accuracy of a computer, that is typically $10^{-8}$. For an accurate determination of $\gamma$ in such a plasma, a different approach is necessary.

In many textbooks on plasma physics, e.g. (Baumjohann & Treumann, 1996), a Taylor expansion around a solution of the dispersion relation $D(\omega, \vec{k}) = 0$ is presented:

$$\gamma(\omega, \vec{k}) = -\frac{\mathrm{Im}(D(\omega_\mathrm{r}, \vec{k}))}{\partial \mathrm{Re}(D(\omega, \vec{k})/\partial\omega)|_{\gamma=0}}. \tag{5.3}$$

In Eq. (5.3) the numerical accuracy of $\gamma$ is determined by that of the calculation of the real and imaginary parts of the dispersion function, and not by the ratio between $\gamma$ and $\omega_\mathrm{r}$. Furthermore, Eq. (5.3) has the advantage that $D(\omega, \vec{k})$ is only evaluated in the special case $\omega = \omega_\mathrm{r}$, i.e. $\gamma = 0$. This greatly simplifies the numerical procedure for determining $D(\omega, \vec{k})$.

For a study of microscopic plasma instabilities it is necessary to calculate the growth rate, $\gamma$, of a wave with frequency $\omega_\mathrm{r}$ that propagates through a plasma with a given electron VDF. The angle $\theta$ between the wave vector, $\vec{k}$, and the background magnetic field, $\vec{B}$ is also given. Under these constraints, the dispersion function $D(\omega, k\,\vec{e}_\theta)$ is well-defined for any wavenumber $k$, where $\vec{e}_\theta$ is a unit vector that points in the direction indicated by $\theta$. The first step is to find the wavenumber of the wave mode under study, i.e. a zero of $D(\omega, k\,\vec{e}_\theta)$ as a function of $k$. Since only the case of small $\gamma \ll \omega_r$ needs to be considered here, the unknown imaginary part of the complex frequency is neglected, and $\omega$ is replaced by $\omega_\mathrm{r}$. Then, a zero of the real part of the dispersion function is sought:

$$\mathrm{Re}(D(\omega_\mathrm{r}, k\vec{e}_\theta)) = 0. \tag{5.4}$$

It is possible that this equation has several solutions with different wavenumbers $k$ that represent different wave modes. In that case, the wave polarizations of the solutions and the cold plasma dispersion relation can be used to identify the correct mode.

Once the wavenumber $k$ and thus the wave vector $\vec{k}$ has been determined, the real and imaginary parts of the dispersion function $D(\omega, \vec{k})$ need to be evaluated. The frequency derivative of the real part can easily be calculated by finite differences. Equation (5.3) then yields the wave growth rate. In the next sections, the dispersion function $D(\omega, \vec{k})$ for a given electron VDF that covers relativistic energies is presented, and the methods of calculating the numerical values of its real and imaginary parts are explained.

### 5.1.2 Derivation of the dispersion function $D(\omega, \vec{k})$

The derivation of the dispersion function $D(\omega, \vec{k})$ can be found in many textbooks of plasma physics, e.g. (Montgomery & Tidman, 1964; Melrose, 1986). The formulae are presented here in order to provide a self-contained description of the calculations.

The dispersion function can be written as

$$D(\omega, \vec{k}) = \det\left(\frac{c^2}{\omega^2}(\vec{k}\vec{k} - 1k^2) + \epsilon(\omega, \vec{k})\right) \tag{5.5}$$

with the dielectric tensor

$$\begin{aligned}\epsilon(\omega, \vec{k}) = \left(1 - \frac{\omega_\mathrm{p}^2}{\omega^2}\right)1 - \sum_j \frac{2\pi\omega_{\mathrm{p},j}^2}{N_j\omega^2} \sum_{l=-\infty}^{\infty} \int_0^\infty p_\perp dp_\perp \int_{-\infty}^{\infty} dp_\parallel \\ \times\left(k_\parallel \frac{\partial f_j}{\partial p_\parallel} + \frac{lq_jB}{p_\perp}\frac{\partial f_j}{\partial p_\perp}\right)\frac{1}{\gamma_\mathrm{L}}\frac{\mathsf{S}_l(p_\perp, p_\perp)}{k_\parallel p_\parallel + lq_jB - m_j\gamma_\mathrm{L}\omega}\end{aligned} \tag{5.6}$$

and the matrix $\mathsf{S}_l$ defined as:

$$\mathsf{S}_l(p_\parallel, p_\perp) = \begin{pmatrix} \frac{l^2q_j^2B^2}{k_\perp^2}J_l^2 & \mathrm{i}\frac{lp_\perp q_jB}{k_\perp}J_lJ_l' & \frac{lp_\parallel q_jB}{k_\perp}J_l^2 \\ -\mathrm{i}\frac{lp_\perp q_jB}{k_\perp}J_lJ_l' & p_\perp^2(J_l')^2 & -\mathrm{i}p_\parallel p_\perp J_lJ_l' \\ \frac{lp_\parallel q_jB}{k_\perp}J_l^2 & \mathrm{i}p_\parallel p_\perp J_lJ_l' & p_\parallel^2 J_l^2 \end{pmatrix}. \tag{5.7}$$

The lower indices $\parallel$ and $\perp$ denote vector components both parallel and perpendicular to the background magnetic field, respectively. $\gamma_\mathrm{L} = (1 - v^2/c^2)^{-1/2} = (1 + p^2/(m_j^2c^2))^{1/2}$ is the Lorentz factor. The order of the resonance is denoted by $l$, and $J_l$ represents the Bessel function of order $l$, $J_l(x)$. It is evaluated at $x = k_\perp p_\perp/(q_jB)$, while $J_l'$ represents its derivative in $x$. The dielectric tensor contains contributions from all particle species $j$ in the plasma, with charge $q_j$, rest mass $m_j$, and number density $N_j$.

## 5.2 Computation of the dielectric tensor

The dielectric tensor with its integral over momentum space has to be evaluated for given gyrotropic particle VDFs, $f_j(p_\parallel, p_\perp)$. This integration is complicated by the resonance denominator $(k_\parallel p_\parallel + lq_jB - m_j\gamma_\mathrm{L}\omega)^{-1}$ that introduces a singularity for those $(p_\parallel, p_\perp)$ that meet the resonance condition

$$k_\parallel p_\parallel + lq_jB - m_j\gamma_\mathrm{L}\omega = 0. \tag{5.8}$$

### 5.2.1 Split of the dielectric tensor

The Taylor expansion of the dispersion function $D(\omega, \vec{k})$ in Eq. (5.3) only requires an evaluation of the dielectric tensor in the limit $\gamma \to 0$, i.e. $\omega \to \omega_\mathrm{r}$. This greatly simplifies the integration over

momentum space in Eq. (5.6). In this limit, the factor $1/\omega^2$ simply turns into $1/\omega_\mathrm{r}^2$. The resonance denominator $(k_\parallel p_\parallel + l q_j B - m_j \gamma_\mathrm{L} \omega)^{-1}$ needs some more attention. According to (Melrose, 1980), it can be split into its real and imaginary parts:

$$\begin{aligned}\frac{1}{k_\parallel p_\parallel + l q_j B - m_j \gamma_\mathrm{L} \omega} &= \frac{k_\parallel p_\parallel + l q_j B - m_j \gamma_\mathrm{L} \omega_\mathrm{r}}{(k_\parallel p_\parallel + l q_j B - m_j \gamma_\mathrm{L} \omega_\mathrm{r})^2 + m_j^2 \gamma_\mathrm{L}^2 \gamma^2} + \\ &\quad \mathrm{i} \frac{m_j \gamma_\mathrm{L} \gamma}{(k_\parallel p_\parallel + l q_j B - m_j \gamma_\mathrm{L} \omega_\mathrm{r})^2 + m_j^2 \gamma_\mathrm{L}^2 \gamma^2}.\end{aligned} \tag{5.9}$$

In the limit $\gamma \to 0$, the real part simply equals $(k_\parallel p_\parallel + l q_j B - m_j \gamma_\mathrm{L} \omega_\mathrm{r})^{-1}$, but the imaginary part introduces the Dirac delta function:

$$\lim_{\gamma \to 0} \frac{m_j \gamma_\mathrm{L} \gamma}{(k_\parallel p_\parallel + l q_j B - m_j \gamma_\mathrm{L} \omega_\mathrm{r})^2 + m_j^2 \gamma_\mathrm{L}^2 \gamma^2} = \pi \delta(k_\parallel p_\parallel + l q_j B - m_j \gamma_\mathrm{L} \omega_\mathrm{r}). \tag{5.10}$$

Due to this split of the resonance denominator, the sums and integrals in Eq. (5.6) can be evaluated independently for both parts. Thus, it is possible to split the dielectric tensor into a "real" and an "imaginary" part:

$$\epsilon = \mathrm{Re}(\epsilon) + \mathrm{i}\,\mathrm{Im}(\epsilon). \tag{5.11}$$

The terms "real" and "imaginary" are set in parenthesis, since the matrix $\mathsf{S}_l$ still contains complex elements. The parts can be written as:

$$\begin{aligned}\mathrm{Re}(\epsilon) = \left(1 - \frac{\omega_p^2}{\omega_\mathrm{r}^2}\right)\mathsf{1} - \sum_j \frac{2\pi\omega_{\mathrm{p},j}^2}{N_j \omega_\mathrm{r}^2} \sum_{l=-\infty}^{\infty} \int_0^\infty p_\perp dp_\perp \int_{-\infty}^{\infty} dp_\parallel \\ \times \left(k_\parallel \frac{\partial f_j}{\partial p_\parallel} + \frac{l q_j B}{p_\perp} \frac{\partial f_j}{\partial p_\perp}\right) \frac{1}{\gamma_\mathrm{L}} \frac{\mathsf{S}_l}{k_\parallel p_\parallel + l q_j B - m_j \gamma_\mathrm{L} \omega_\mathrm{r}}\end{aligned} \tag{5.12}$$

and

$$\begin{aligned}\mathrm{Im}(\epsilon) = -\sum_j \frac{2\pi\omega_{\mathrm{p},j}^2}{N_j \omega_\mathrm{r}^2} \sum_{l=-\infty}^{\infty} \int_0^\infty p_\perp dp_\perp \int_{-\infty}^{\infty} dp_\parallel \\ \times \left(k_\parallel \frac{\partial f_j}{\partial p_\parallel} + \frac{l q_j B}{p_\perp} \frac{\partial f_j}{\partial p_\perp}\right) \frac{1}{\gamma_\mathrm{L}} \mathsf{S}_l \pi \delta(k_\parallel p_\parallel + l q_j B - m_j \gamma_\mathrm{L} \omega_\mathrm{r}).\end{aligned} \tag{5.13}$$

The "real" part is of Hermitian and the "imaginary" part is of anti-Hermitian structure. They are associated with the reactive and dissipative parts of the plasma's response to the wave field, respectively (Melrose, 1986).

### 5.2.2 Evaluation of the "real" part

The "real" part of the dielectric tensor as defined in Eq. (5.12) is a complicated integral over the whole momentum space that contains momentum derivatives of the particle VDF. It still has a resonance denominator that leads to a singularity if the resonance condition (5.8) is met. It is very complicated to evaluate this integral numerically for an arbitrary VDF.

However, it can be simplified considerably. If the VDF has no short-periodic (in momentum space) variations, the momentum derivatives can be expected to take their highest values if the VDF $f_j(p_\parallel, p_\perp)$ itself has its highest values, i.e. within the thermal core of the VDF. Thus, the thermal core of the distribution dominates the "real" part of the dielectric tensor. In space plasma physics, the thermal core of a particle distribution is typically close to a Maxwellian VDF, even in the tenuous plasma of the solar wind, see Fig. 1.3. Thus, it is reasonable to calculate $\mathrm{Re}(\epsilon)$ for a Maxwellian VDF that has the same particle number density and temperature as the VDF $f_j(p_\parallel, p_\perp)$.

The fact that the thermal speed is nonrelativistic, $v_{\mathrm{th}} \ll c$, even for electrons in the solar corona, further simplifies Eq. (5.12). The electron thermal speed for electrons with a temperature of, e.g., $T = 1.4 \cdot 10^6\,\mathrm{K}$ is $v_{\mathrm{th}} = 4600\,\mathrm{km\,s^{-1}}$. Thus, the thermal core and its contribution to $\mathrm{Re}(\epsilon)$ can be described in the nonrelativistic limit with a Lorentz factor $\gamma_{\mathrm{L}} = 1$. This simplifies Eq. (5.12) considerably, since it removes a complicated dependence on the momentum coordinate and enables an analytic solution of the integral for a Maxwellian VDF.

Inserting a Maxwellian VDF, $f_{j,\mathrm{M}}(p_\parallel, p_\perp) \propto \exp(-(p_\parallel^2 + p_\perp^2)/(2p_{\mathrm{th}}^2))$, into Eq. (5.12) enables further analytic treatment of $\mathrm{Re}(\epsilon)$, since

$$\left(k_\parallel \frac{\partial f_{j,\mathrm{M}}}{\partial p_\parallel} + \frac{l q_j B}{p_\perp} \frac{\partial f_{j,\mathrm{M}}}{\partial p_\perp}\right) = -\frac{f_{j,\mathrm{M}}}{p_{\mathrm{th}}^2}(k_\parallel p_\parallel + l q_j B) \tag{5.14}$$

and the corresponding factor in equation (5.12) becomes

$$-\frac{f_{j,\mathrm{M}}}{p_{\mathrm{th}}^2} \frac{k_\parallel p_\parallel + l q_j B}{k_\parallel p_\parallel + l q_j B - m_j \omega_{\mathrm{r}}} = -\frac{f_{j,\mathrm{M}}}{p_{\mathrm{th}}^2}\left(1 - \frac{m_j \omega_{\mathrm{r}}}{k_\parallel p_\parallel + l q_j B - m_j \omega_{\mathrm{r}}}\right) \tag{5.15}$$

The momentum-space integral in Eq. (5.12) still has a singularity when $p_\parallel$ meets the resonance condition, but the integral now has the form of the well-known plasma dispersion function

$$Z(\zeta) = \frac{1}{\sqrt{\pi}} \int_\infty^\infty \frac{\exp(-t^2)}{t - \zeta}\, dt \tag{5.16}$$

that yields well-defined values for all matrix elements of $\mathrm{Re}(\epsilon)$.

### 5.2.3 Evaluation of the "imaginary" part

The evaluation of the "imaginary" part of the dielectric tensor, Eq. (5.13), is simplified considerably by the Dirac delta distribution. The 2-dimensional integral over momentum space is reduced to a line integral along the solution of the resonance condition, Eq. (5.8). It is noteworthy that the geometry of the line $p_\perp(p_\parallel)$ is that of a conic section (see e.g. Melrose Melrose (1986)). This could be an ellipse, parabola, or hyperbola, depending on whether the wave phase speed $v_{\mathrm{ph}}$ is greater, equal, or less than $c\cos\theta$, respectively, with light speed $c$ and wave propagation angle $\theta$ relative to the background magnetic field.

In velocity space, the corresponding line $v_\perp(v_\parallel)$ always has the geometry of a resonance ellipse

$$\frac{(v_\parallel - v_0)^2}{a_\parallel^2} + \frac{v_\perp^2}{a_\perp^2} = 1 \tag{5.17}$$

with ellipse axes

$$a_{\parallel} = \frac{\xi c}{\sqrt{k_{\parallel}^2 c^2 + l^2 \Omega_{j,0}^2}}, \qquad a_{\perp} = \frac{\xi c}{l \Omega_{j,0}} \tag{5.18}$$

and a center location

$$v_0 = \frac{k_{\parallel} \omega_{\mathrm{r}} c^2}{k_{\parallel}^2 c^2 + l^2 \Omega_{j,0}^2} \tag{5.19}$$

$\Omega_{j,0} = q_j B / m_j$ is the electron cyclotron frequency in the non-relativistic limit, and $\xi$ is defined as:

$$\xi = \sqrt{l^2 \Omega_{j,0}^2 - \omega_{\mathrm{r}}^2 + \frac{k_{\parallel}^2 \omega_{\mathrm{r}}^2 c^2}{k_{\parallel}^2 c^2 + l^2 \Omega_{j,0}^2}} \tag{5.20}$$

For a given $(\omega_r, \vec{k})$, only the part of the VDF along the line $p_{\perp}(p_{\parallel})$ contributes to $\mathrm{Im}(\epsilon)$. An important consequence is that the integration path might avoid the thermal core of the VDF, and cross a structure of the distribution that provides free energy for wave growth, e.g. a loss cone. In that case, the integral is not affected by the much higher phase-space density of the thermal core, and numerical errors due to the orders-of-magnitude difference between the phase-space densities cannot occur. This is why the method presented here enables an accurate treatment of small wave growth/damping rates.

## 5.3 Calculation of the dispersion function

With the numerical values for the dielectric tensor at hand, the dispersion function, Eq. (5.5), can now be calculated easily for a given $(\omega_r, \vec{k})$ and particle VDFs $f_j(p_{\parallel}, p_{\perp})$. Inserting the results into Eq. (5.3) finally yields the wave growth rate.

It turns out that the imaginary part of the dispersion function, $\mathrm{Im}(D)$, is of first order in the "imaginary" part of the dielectric tensor. Thus, if the resonance line through momentum space only traverses regions with low values of the VDF, $\mathrm{Im}(D)$, and by means of Eq. (5.3) the wave growth rate, will also be low.

On the other hand, the real part of the dispersion function, $\mathrm{Re}(D)$, is of second order in the "imaginary" part of the dielectric tensor. Since this term is small for small wave growth rates, this justifies the use of the real part of the dispersion function as a substitute for finding a zero of the dispersion function in Eq. (5.4) for calculating the wavenumber of the wave mode under consideration.

In the following chapters, this method will be applied on wave generation from loss-cone distributions of electrons in the solar corona. This could be either electron cyclotron maser or whistler wave emission, depending on the ratio of plasma frequency to electron cylcotron frequency, $\omega_{\mathrm{p}}/\Omega_{\mathrm{e}}$.

# Chapter 6

# Electron cyclotron maser emission from solar coronal funnels

The generation of electromagnetic waves through the electron cyclotron maser mechanism is well known as a source of planetary radio emission like Earth's auroral kilometric radiation (Wu & Lee, 1979) or Jupiter's decametric radiation (Wu & Freund, 1977).

The electron cyclotron maser is based on the conversion of free energy provided by a loss cone distribution of the electrons into X-mode plasma waves and can be active in a plasma with a plasma frequency well below the electron cyclotron frequency, $\omega_p \ll \Omega_e$ (Melrose et al., 1984). The X-mode waves are emitted nearly perpendicular to the background magnetic field (Wu & Lee, 1979; Omidi et al., 1984; Ladreiter, 1991).

The electron cyclotron maser theory has not only been applied on planetary magnetospheres, but also on solar flares (Melrose, 1982; Conway & Willes, 2000). Energetic electrons are injected near the looptops during the flare, propagate downwards and are mirrored in the magnetic field geometry that converges towards the footpoints. Electrons with low pitch angles penetrate deep into this magnetic mirror configuration. They are scattered in the cooler and denser medium of the transition region and do not return into the loop. Thus, the electron velocity distribution function (VDF) can form a loss cone in a flaring loop.

But it is possible that electron loss cone VDFs can be formed in the solar atmosphere also under quiet conditions without any flare activity. Coronal funnels (Gabriel, 1976) are magnetic structures that are open towards the interplanetary medium. They are characterized by a rapid expansion of magnetic flux tubes in the transition region from the chromosphere towards the corona. On the one hand, in the chromosphere and below the gas pressure is much larger than the magnetic field energy density. Consequently, the convective motion of the supergranular cells accumulates the magnetic field at the borders of these cells. On the other hand, in the corona the magnetic field energy density is much larger than the gas pressure of the tenuous coronal plasma. This configuration leads to a rapid expansion of magnetic flux tubes in the transition region.

Such a magnetic field configuration acts as a magnetic mirror for coronal electrons that move sunwards. Electrons with small enough pitch angles penetrate deep into the funnel and reach the cooler and denser medium of the transition region or chromosphere. This electron population is

scattered and subsequently thermalized there. It does not return into the corona, resulting in a loss cone distribution in the low corona.

It is shown in the next section that the condition $\omega_p < \Omega_e$ for the electron cyclotron maser can be fulfilled in a coronal funnel. Therefore, Vocks & Mann (2004) have addressed the question whether the quiet sun can be a source of radio emission through the electron cyclotron maser mechanism. There is some observational evidence for radio emission from the chromospheric network. Kosugi et al. (1986) report higher brightness temperatures in coronal holes at a frequency of 36 GHz that is not found at a higher frequency of 98 GHz. Gopalswamy et al. (1999) analyze 17 GHz observations and find a temperature enhancement of the chromosphere below coronal holes. They discuss the relation between enhanced brightness temperatures and unipolar regions. Moran et al. (2001) observed enhanced 17 GHz radio emission from magnetic field concentrations.

The observed frequencies are well above typical electron cyclotron frequencies in coronal funnels, e.g. 560 MHz for a magnetic field of $B = 0.02\,\mathrm{T}$ (200 G). But nevertheless, these observations further motivate the study whether coronal funnels are capable of emitting radio waves through the cyclotron maser mechanism even under quiet solar conditions.

Vocks & Mann (2004) have applied the kinetic model for electrons in the solar corona and wind on the transition region and low corona to study the loss cone formation in detail. The kinetic model yields the electron VDF for each spatial location within the computation box. With these simulation results at hand it is possible to investigate, by means of the method presented in the previous chapter, whether the low coronal plasma is capable of emitting X-mode waves in an efficient way.

## 6.1 Electron loss-cone VDF in a coronal funnel

The electron kinetic model of Vocks & Mann (2003), as described in Sections 2.4 and 4.3, is applied on the plasma of a coronal funnel that is located in the transition region and low corona of the Sun. The magnetic field geometry of the coronal funnel is adopted from the coronal funnel model of (Hackenberg et al., 2000). The kinetic model includes the effects of the gravitational and the charge separation electric fields, the diverging geometry of the coronal funnel, as well as Coulomb collisions.

### 6.1.1 The simulation box

The lower boundary of the simulation box is located in the transition region at a temperature level of $2 \cdot 10^5$ K. It extends over 20 000 km into the low corona. Due to the assumption of a gyrotropic electron VDF, the simulation box has only one spatial coordinate $s$ along the background magnetic field, $\vec{B}$. The value $s = 0$ corresponds to the lower bound of the simulation box. The velocity coordinates $v_\parallel$ and $v_\perp$ parallel and perpendicular to $\vec{B}$, respectively, cover electron speeds up to $4.3 \cdot 10^4\,\mathrm{km\,s^{-1}}$.

Figure 6.1 shows the background plasma conditions within the simulation box. The rapid expansion of the magnetic field geometry can clearly be seen in Fig. 6.1a as a strong decrease of

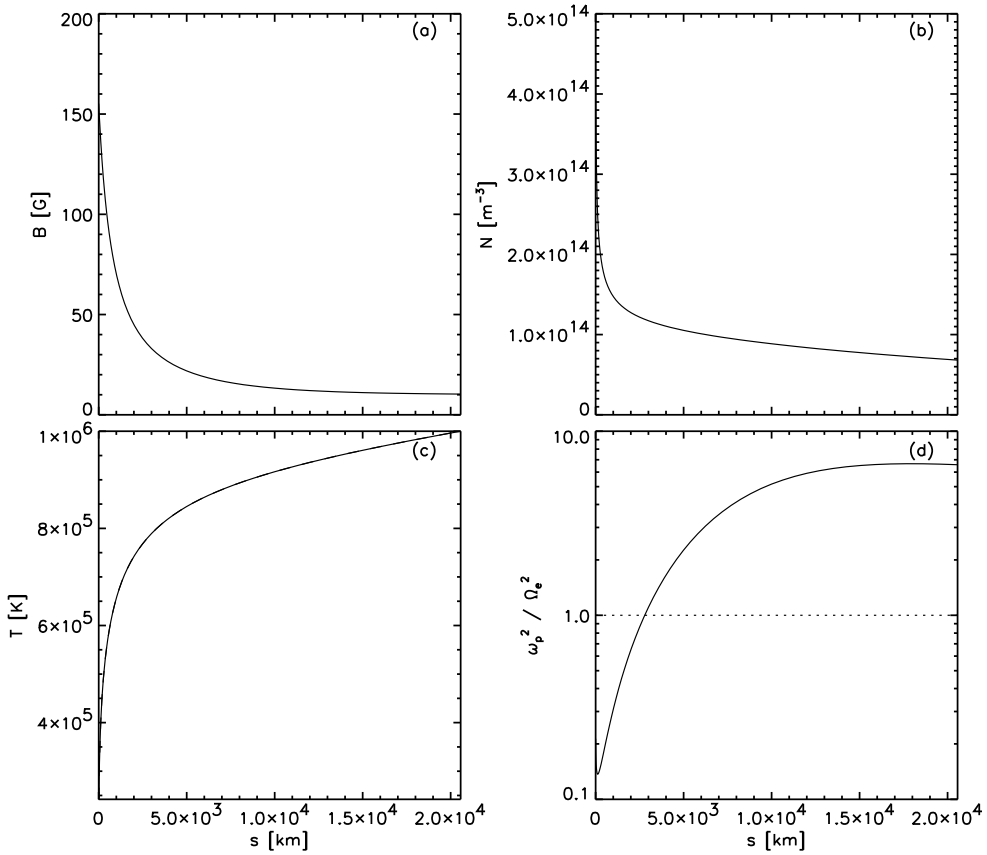


Figure 6.1: Background plasma conditions for the kinetic model as functions of the height, $s$, within the simulation box. Shown are (a) magnetic field, (b) number density, (c) temperature, and (d) ratio $\omega_p^2/\Omega_e^2$. Protons and electrons have the same number densities and temperatures.

the magnetic field within the lowest 5000 km. Figs. 6.1b and 6.1c show the strong density and temperature gradients of the transition region.

In Fig. 6.1d, the square of the ratio between the plasma frequency, $\omega_p$, and the electron cyclotron frequency, $\Omega_e$, is plotted. The plot shows that the necessary condition for the cyclotron maser mechanism, $\omega_p < \Omega_e$, is fulfilled within the coronal funnel and in the lowest corona, but not at larger heights in the corona.

### 6.1.2 Simulation results

The electron VDF is now computed inside this simulation box. As initial condition a Maxwellian electron VDF with the same density and temperature as in the background condition is defined. The temporal evolution of the electron VDF is computed until a final steady state has been reached.

The simulation results indeed show the formation of a loss cone. It is most pronounced in the strong gradients of the transition region and fades away with height in the low corona. This result is expected, since electrons that move sunwards with small pitch angles, i.e. nearly parallel to the background magnetic field, penetrate deep into the lower transition region where the density is

higher and the temperature is lower. They are scattered and thermalized there, while electrons with larger pitch angles are reflected at larger heights in the magnetic mirror of the coronal funnel. As a result, in the upper transition region and lowest portions of the corona the phase space density of electrons moving anti-sunwards with small pitch angle is reduced compared to that of electrons with larger pitch angles. Thus, a loss cone is formed. At larger heights in the corona, the Coulomb collisions fill up the loss cone, so it becomes less pronounced with height.

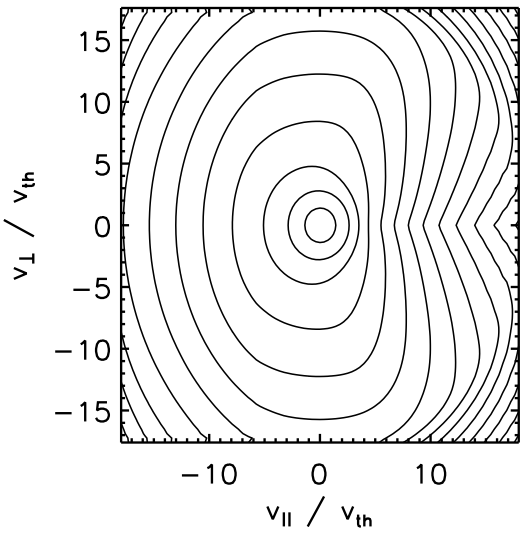


Figure 6.2: Electron VDF at a height of $s = 96\,\mathrm{km}$. The electron temperature at this height is $T_\mathrm{e} = 3.88 \cdot 10^5\,\mathrm{K}$, and the electron thermal speed thus $v_\mathrm{th} = 2420\,\mathrm{km\,s^{-1}}$ The isolines are chosen in such a way that they would form equidistant circles for a Maxwellian VDF.

Figure 6.2 shows the electron VDF at a height of $s = 96\,\mathrm{km}$ in the simulation box. This height level is located in the transition region at an electron temperature of $T_\mathrm{e} = 3.88 \cdot 10^5\,\mathrm{K}$, corresponding to an electron thermal speed of $v_\mathrm{th} = 2420\,\mathrm{km\,s^{-1}}$. The loss cone is clearly visible, but it is restricted to speeds $v_\parallel > 4\,v_\mathrm{th}$, with $v_\mathrm{th}$ being the electron thermal speed. At lower speeds, a thermal core dominates.

The restriction of the loss cone to higher speeds of several thermal speeds has the consequence that only a small fraction of electron kinetic energy is available for radio wave emission. But the total number density of the electrons, $N_\mathrm{e} = 2 \cdot 10^{14}\,\mathrm{m^{-3}}$, is high enough to justify the assumption that the available free energy density is still capable of emitting significant radio wave power.

## 6.2 X-mode wave growth and absorption in the low corona

In the previous chapter a method has been presented for calculating plasma wave growth/damping rates for electron VDFs that are yielded by the kinetic model. It enables an evaluation of the dispersion function, Eq. (5.5), and thus with Eq. (5.3) of the wave growth rates, $\gamma$. For the X-mode, the resonance ellipse, Eq. (5.17) that describes the line integral in velocity space for the "imaginary" part of the dielectric tensor, can become rather small. Therefore, it differs significantly from

the straight line in momentum space that results from the non-relativistic resonance condition and its resonance speed, $v_{\parallel}$, independent of $v_{\perp}$:

$$v_{\parallel} = \frac{(\omega - l\Omega_e)}{k_{\parallel}} \tag{6.1}$$

This is essential for the cyclotron maser mechanism (Wu & Freund, 1977) and the reason why a relativistic effect is so important for electron energies of just a few keV and below, as they are discussed here.

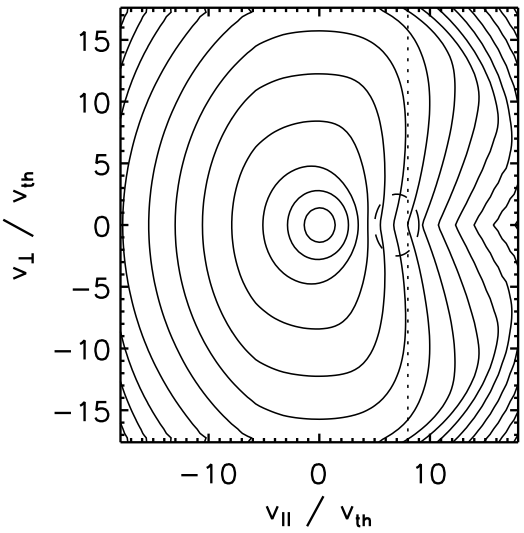


Figure 6.3: Electron VDF at a height of $s = 96\,\mathrm{km}$, as in Fig. 6.2. Shown are also a sketch of a resonance ellipse (dashed line) and an integration path for the nonrelativistic theory (dotted line).

Figure 6.3 shows the plot of the electron VDF from Fig. 6.2 together with a sketch of a resonance ellipse and the nonrelativistic integration path according to Eq. (6.1). The difference between relativistic and nonrelativistic case is considerable, in the relativistic case the whole integration path is located inside the loss cone.

Now X-mode wave growth rates, $\gamma$ are determined for the transition region electron VDF obtained by the kinetic model. The growth rates are calculated as functions of the wave frequency $\omega$ and the angle $\theta$ between the wave vector and the background magnetic field. This requires the determination of a wave number, $k$, for each $(\omega, \theta)$ by the dispersion relation, Eq. (5.2). Only waves propagating away from the sun are considered, i.e. with $k_{\parallel} \geq 0$, that possibly could be observed in interplanetary space or on Earth.

Figure 6.4 shows the dispersion relation of X-mode waves propagating perpendicular to the background magnetic field. The ratio between plasma frequency and electron cyclotron frequency has been chosen as $\omega_p^2/\Omega_e^2 = 0.25$, which is a typical value for the coronal funnel, see Fig. 6.1d.

The necessary condition for cyclotron maser emission, $\omega_p^2 < \Omega_e^2$, is fulfilled, but not $\omega_p^2 \ll \Omega_e^2$ (Ladreiter, 1991). This has an important influence on the dispersion relation. The X-mode branch does not start at $\omega = \Omega_e$, but well above $\Omega_e$. Since the wave emission at the resonance of the

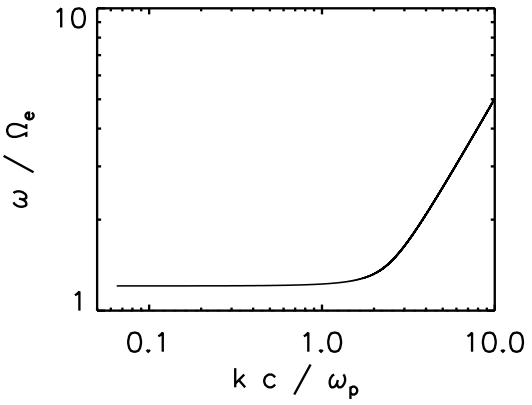


Figure 6.4: Dispersion relation of the X-mode propagating perpendicular to the background magnetic field in a plasma with $\omega_p^2/\Omega_e^2 = 0.25$

order $l$ is restricted to a small region around $l\Omega_e$ by the resonance condition, Eq. (5.8), no wave generation on the fundamental mode, $l = 1$, is possible in the coronal funnel.

### 6.2.1 Wave emission at $\omega \approx 2\,\Omega_e$

For this reason, wave emission is only possible at the order $l = 2$ or higher. So the case $l = 2$ is now considered and wave growth rates are calculated for the electron VDF in the coronal funnel from Fig. 6.2.

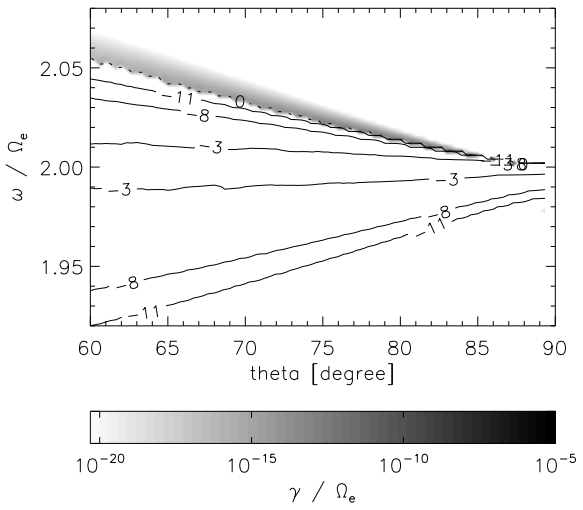


Figure 6.5: Growth rates of X-mode waves in the coronal funnel at $s = 96\,\mathrm{km}$ as function of wave frequency, $\omega$, and propagation angle, $\theta$. Positive growth rates, $\gamma > 0$, are displayed as a greyscale plot, and negative growth rates, $\gamma < 0$, by isolines marked with numbers that denote an exponent, e.g. -3 corresponds to $\gamma/\Omega_e = -10^{-3}$.

Figure 6.5 displays the wave growth rates that result from this electron VDF. $\gamma$ has positive values in a small region in frequency space. This region extends over all propagation angles $\theta$, and the maximum values of $\gamma$ increase with $\theta$. Thus waves propagating nearly perpendicular to the background magnetic field are generated preferredly, as it is expected for the cyclotron maser mechanism. But as $\theta \rightarrow 90°$, the frequency range of the wave generation region becomes very small and falls below the differences in resonance frequency that correspond to adjacent points in velocity space of the computational grid of the kinetic model for the electrons. This plot shows that the electron cyclotron maser mechanism is active and can produce X-mode waves in a coronal funnel under quiet solar conditions.

The split of the frequency space into a region with wave growth at high frequencies and into a region with wave absorption around and below the twofold electron cyclotron frequency is a consequence of the resonance condition, Eq. (5.8). The resonance frequency, $\omega_{\mathrm{res}}$, is determined by:

$$\omega_{\mathrm{res}} = l\Omega_{\mathrm{e}} + k_{\parallel} v_{\parallel} \tag{6.2}$$

The higher $v_{\parallel}$, the higher is $\omega_{\mathrm{res}}$. The plot of the electron VDF, Fig. 6.2, shows that the loss cone and thus the region in velocity space that provides free energy to the electron cyclotron maser mechanism, is restricted to high positive $v_{\parallel}$. This is the reason for the wave growth at high frequencies. This wave growth region is restricted towards even higher frequencies by the decrease of the phase space density of the electron VDF at the correspondingly high $v_{\parallel}$.

Waves with lower frequencies $\omega \approx 2\,\Omega_{\mathrm{e}}$ interact with electrons with lower $v_{\parallel}$, where the VDF is close to a Maxwellian or Bi-Maxwellian. This portion of the VDF provides no energy for wave growth. Therefore, such waves suffer relatively strong damping with $|\gamma| > 10^{-3}\,\Omega_{\mathrm{e}}$, as can be seen in Fig. 6.5.

This wave damping at frequencies $\omega \approx 2\,\Omega_{\mathrm{e}}$ and below does not prevent the waves generated at higher frequencies from escaping into interplanetary space. In a coronal funnel and in the corona, the magnetic field decreases with height and thus along the path of wave propagation. So the frequency of a wave that is generated by the cyclotron maser mechanism, and propagates away from the sun, increases in units of the local electron cyclotron frequency. This has the consequence that the wave leaves the region of positive $\gamma$ in Fig. 6.5 towards a frequency domain where no wave-particle interaction and thus no absorption takes place.

However, the positive $\gamma$ in Fig. 6.5 are very small, with a maximum of $10^{-8}\,\Omega_{\mathrm{e}}$. This is due to the restriction of the loss cone in Fig. 6.2 to higher electron speeds of several $v_{\mathrm{th}}$. At the speeds where the loss cone appears, the phase space density of the electrons is already small compared to the thermal bulk. This results in only a few electrons contributing to the wave growth. So only weak wave emission can be expected from this electron cyclotron maser.

### 6.2.2 Wave emission and absorption at $\omega \approx 3\,\Omega_e$

As a wave that has been generated by the $l = 2$ resonance propagates further up into the corona, its frequency $\omega$ remains constant, but the magnetic field and thus $\Omega_{\mathrm{e}}$ continue to decrease. At a certain height, the condition $\omega = 3\,\Omega_{\mathrm{e}}$ is fulfilled. For waves emitted at $s = 96\,\mathrm{km}$, this is the case at a height of $s = 513\,\mathrm{km}$.

Now the wave interacts with the electrons through the $l = 3$ resonance. Since the magnetic field and $\Omega_e$ continuously vary with height, the wave successively passes layers where its frequency is slightly below, equal to, and slightly above $3\,\Omega_e$.

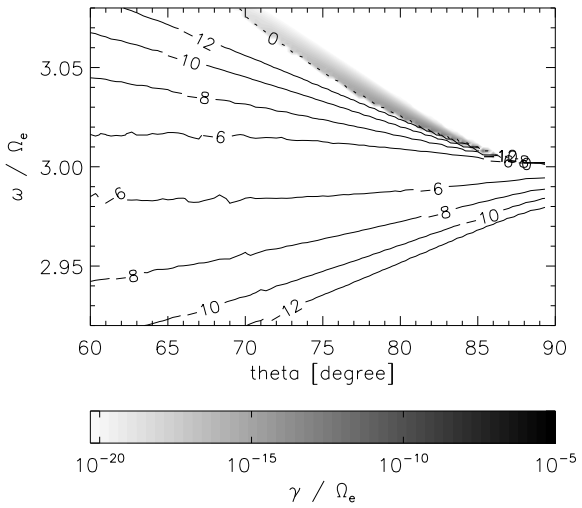


Figure 6.6: Growth rates of X-mode waves in the coronal funnel at $s = 513\,\mathrm{km}$ as function of wave frequency, $\omega$, and propagation angle, $\theta$. Positive growth rates, $\gamma > 0$, are displayed as a greyscale plot, and negative growth rates, $\gamma < 0$, by isolines marked with numbers that denote an exponent, e.g. -6 corresponds to $\gamma/\Omega_e = -10^{-6}$.

Figure 6.6 shows the wave growth rates for $l = 3$ at a height of $s = 513\,\mathrm{km}$. At a first glance, the picture looks similar to Fig. 6.5 for $l = 2$ and $s = 96\,\mathrm{km}$. At higher frequencies waves are generated, since the loss cone in the electron VDF is still present. But due to the lower density at $s = 513\,\mathrm{km}$ and the lower efficiency of the wave-particle interaction at $l = 3$ both the wave absorption rates as well as the wave growth rates are smaller here.

Nevertheless, the wave absorption rate at $\omega = 3\,\Omega_e$ is still some orders of magnitude higher than the maximum wave growth rate in the $l = 2$ case. The wave absorption at $l = 3$ is much stronger than the emission at $l = 2$. It follows that a wave that is emitted in the coronal funnel by the $l = 2$ resonance can be damped at $l = 3$ down to a level below the initial background fluctuation that started growing at $l = 2$ through the cyclotron maser mechanism.

Figure 6.6 shows some weak wave emission at frequencies little above $3\,\Omega_e$, but these waves also will interact with the next higher, i.e. $l = 4$, resonance at some larger height. There, the wave absorption again will exceed the emission at $l = 3$, so that these waves also cannot escape into interplanetary space. If the electron VDF still has the loss cone at the $l = 4$ level, some wave emission might be possible, but these waves are absorbed at $l = 5$, and so forth. The loss cone disappears with height above the coronal funnel, and the plasma frequency, $\omega_p$, eventually becomes larger than $\Omega_e$ at a certain level, see Fig. 6.1. Since the necessary condition $\omega_p < \Omega_e$ is not fulfilled, no wave generation is possible above this level.

To summarize, these model calculations show that X-mode wave generation through the cyclotron maser mechanism is possible in a coronal funnel. But higher-order resonances absorb these waves at larger heights in the corona, so they cannot escape into interplanetary space.

## 6.3 Summary

The rapidly opening magnetic structure of a coronal funnel provides the geometry of a magnetic mirror, and the condition $\omega_p < \Omega_e$ is found to be fulfilled in the transition region and low corona within this funnel. So it is reasonable to suppose and worth to investigate whether the quiet solar atmosphere is capable of generating radio waves through the electron cyclotron maser mechanism in coronal funnels. The electron cyclotron maser mechanism is well known to be active in other space plasmas, as it generates Jupiter's decametric radiation (Wu & Freund, 1977) or Earth's auroral kilometric radiation (Wu & Lee, 1979).

The electron VDF in a coronal funnel is calculated by the kinetic model that solves the Boltzmann-Vlasov equation for the electrons. The VDF shows the expected loss cone. The condition $\omega_p < \Omega_e$ is also fulfilled at the same height within the funnel, so the cyclotron maser mechanism can be active. The question is: Is it efficient enough to produce significant wave power that could be observed?

To answer this question, the method described in chapter 5 of deriving the wave growth rate $\gamma$ from an electron VDF is used. The application of this method on the coronal funnel plasma shows that the electron cyclotron maser mechanism is indeed active at the resonance orders $l = 2$ and higher, but the wave growth rates are small. The waves can escape from the site of their generation, but they are absorbed at a height level where they interact with the plasma through the resonance of next higher order. Thus, an emission of X-mode waves from coronal funnels at the borders of the supergranular network seems not to be possible.

The reason for the low wave growth rates, that are smaller than the absorption rates at the next higher resonance, is the low phase space density of that portion of the electron VDF that shows the loss cone. The loss cone is restricted to higher speeds $v_\parallel$ as can be seen in Fig. 6.2, so its phase space density is much smaller than that of the thermal bulk, that is mainly responsible for the wave absorption at the next higher resonance.

Of course the exact shape of the electron VDF depends on the coronal funnel model assumptions and parameters. However, due to the strong dependence of the Coulomb collision frequency on the electron velocity, that scales with $v^{-3}$, it cannot be expected that it is possible to extend the loss cone significantly towards the thermal core, and thus to enhance the wave growth rates by modifying the funnel geometry.

In a solar flare the conditions may be different and enable more efficient wave generation through the injection of energetic electrons from the tops of the flaring loop, as it is described by (Melrose, 1982). Thus the Sun could produce radio waves through the cyclotron maser mechanism. However, under quiet solar conditions the condition $\omega_p \ll \Omega_e$ for wave generation on the fundamental mode is not fulfilled, nor is the loss cone in the electron VDF located in a region with a high phase space density sufficiently high for efficient wave production.

So it has to be concluded that the electron cyclotron maser mechanism is not able to provide significant radio wave emission from coronal funnels at the supergranular network, despite the fulfillment of the necessary conditions for the cyclotron maser mechanism.

# Chapter 7

# Whistler wave excitation by relativistic electrons during solar flares

The generation of X-mode waves that has been discussed in the previous chapter requires a plasma frequency smaller than the electron cyclotron frequency, $\omega_p \ll \Omega_e$, i.e. low density and strong magnetic fields. This condition is only met at the bottom of coronal funnels, where the magnetic field rapidly expands towards coronal holes with low plasma density. But this is the exception in the corona, as readily seen in Fig. 6.1d. Especially in closed structures as coronal loops, the opposite criterion $\omega_p \gg \Omega_e$ is fulfilled. In such a plasma, a loss-cone distribution leads to the emission of whistler rather than X-mode waves. Due to the higher density that quickly thermalizes electrons below the keV energy range, see chapter 4.4.2, loss-cone distributions are less prominent in closed loops than in coronal funnels under quiet solar conditions. But if energetic electrons are injected into the loop during a solar flare, then loss-cones can form and whistler waves are generated. Wave packets propagating along magnetic loops are the standard model for the generation of so-called fiber bursts that are observed in dynamical radio spectra during solar flares. Vocks & Mann (2006) have studied this whistler wave production in detail.

## 7.1 Solar flare electrons

Solar flares accelerate electrons to high energies (Lin, 1974) and lead to the generation of various types of radio emission, see e.g. Warmuth & Mann (2004) as a review. Figure 7.1 shows a hard X-ray photon spectrum of the flare of 28 October 2003 as observed by the RHESSI satellite (Lin et al., 2002). The photon spectrum clearly shows the presence of a nonthermal power-law component and additionally thermal emission. Supposing thick target bremsstrahlung (Brown, 1971), an injected electron-flux spectrum with a power-law index of typically $\delta = 3.8$ can be derived from the photon spectrum (for the method, see e.g. Holman et al. (2003)). Such values are typical of solar flares, see chapter 3.1.1.

These highly energetic electrons can be trapped in coronal loops. They are mirrored at the loop footpoints and can establish a loss-cone distribution (Croley et al., 1978). Such a distribution is unstable and gives rise to whistler wave excitation (Scharer & Trivelpiece, 1967; Mann et al.,

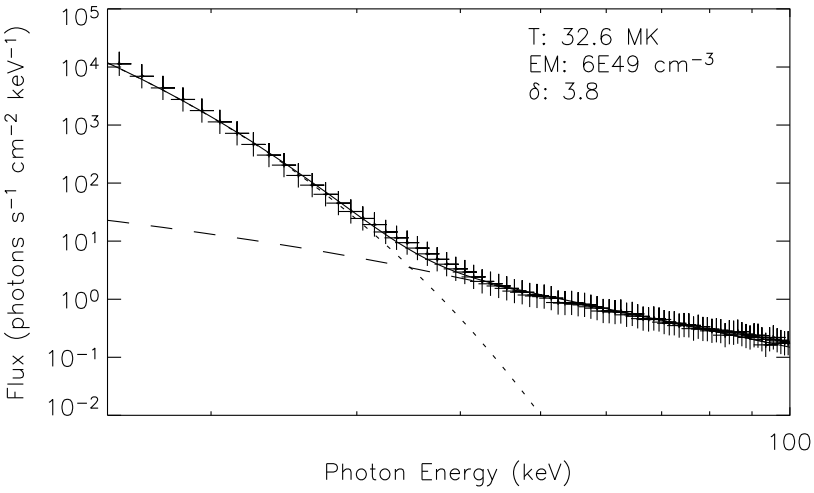


Figure 7.1: Hard X-ray photon spectrum of the flare on 28 October 2003, 11:17:00 – 11:17:20 UT, as observed by the RHESSI satellite. The spectrum shows a thermal (dotted line) and nonthermal power-law component (dashed line), as well as the power-law index $\delta = 3.8$ of the derived electron-flux spectrum.

1989). If these whistlers nonlinearly coalescence with high-frequency plasma waves, e.g. Langmuir waves, into radio waves, they can be observed as fiber (or intermediary drift) bursts (Kuijpers, 1975; Mann et al., 1987; Benz & Mann, 1998; Aurass et al., 2005) in the solar radio radiation, e.g. within type IV radio bursts.

Figure 7.2 shows fiber bursts in the dynamical radio spectrum that was recorded by the Observatory of Solar Radioastronomy of the Leibniz-Institut für Astrophysik Potsdam (Mann et al., 1992) during the event of 28 October 2003 at the same time as the photon spectrum from Fig. 7.1 was taken. Fiber bursts appear as stripes of enhanced radio emission in the dm-range ($\approx 400 - 800$ MHz) in dynamical radio spectra. They are drifting from high to low frequencies with (intermediate) drift rates between those of type II and type III radio bursts (Kuijpers, 1975).

In previous studies, e.g. (Scharer & Trivelpiece, 1967; Mann et al., 1989), the energetic electrons are considered to be non-relativistic. The recent paper by Aurass et al. (2005) shows that the whistler waves associated with fiber bursts are generated by relativistic electrons. These results have motivated the study of Vocks & Mann (2006), which requires treating the whistler wave excitation within a relativistic framework that is provided by the method described in chapter 5.

## 7.2 Whistler-wave generation in flaring loops

### 7.2.1 Loss cone distributions

The electrons that are injected into the magnetic loop propagate along the magnetic field lines down to the loop footpoints. The magnetic field increases towards the footpoints, and due to

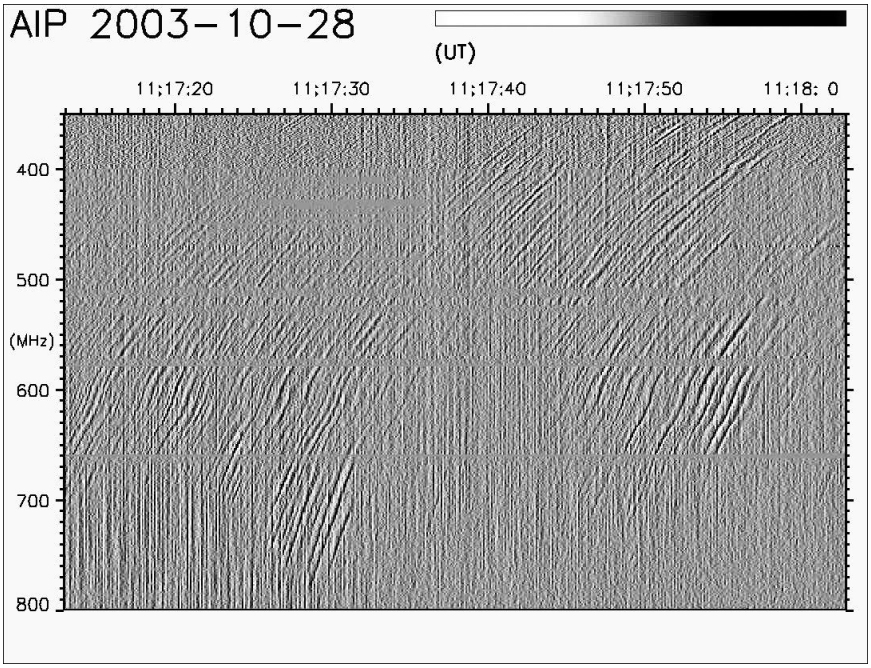


Figure 7.2: A typical part of a patch of fiber bursts in the dynamical radio spectrum of 28 October 2003. The image shows the spectrum's temporal derivative. The data were recorded by the Observatory of Solar Radioastronomy of the Leibniz-Institut für Astrophysik Potsdam.

conservation of magnetic moment the electrons are mirrored close to the footpoint and reflected back into the loop.

But the smaller the initial electron pitch angle, the further an electron can go down the loop before it is mirrored. Electrons with sufficiently small pitch angles can penetrate deep into the solar atmosphere and are scattered and thermalized in the cool and dense transition region and chromosphere. Since these electrons are not reflected back into the corona, a loss-cone electron distribution forms in the flaring loop. Loss-cone distributions are well known for emitting whistler waves, as observed in the solar corona (Kuijpers, 1975), as well as in Earth's (Helliwell, 1975), and Jupiter's (Xiao et al., 2003) magnetosphere.

The objective now is to calculate whistler-wave growth rates for a loss-cone distribution that is typical of a flaring loop, and to investigate whether the wave growth is fast enough to account for the fiber-burst observations.

The model electron VDF has two components, the thermal background plasma of the solar corona and a hot, nonthermal component that has been produced by the flare. The background plasma has a Maxwellian VDF, $f_\mathrm{b}(p)$, with a temperature of $T_\mathrm{b} = 1.4 \cdot 10^6\,\mathrm{K}$ and a density of $N_\mathrm{b} = 1.33 \cdot 10^{15}\,\mathrm{m}^{-3}$, which corresponds to a plasma frequency of $f_\mathrm{p} = 327\,\mathrm{MHz}$ where fiber bursts usually are observed (Aurass et al., 2005). The magnetic field has been set to $B = 3 \cdot 10^{-4}\,\mathrm{T}$ (3 G), in agreement with the data analysis of Aurass et al. (2005). These plasma conditions correspond to a ratio of $\omega_\mathrm{p}/\Omega_\mathrm{e} = 39$ between the plasma frequency and the electron cyclotron frequency. Such high values of $\omega_\mathrm{p}/\Omega_\mathrm{e} \gg 1$ are typical of the solar corona (Vocks & Mann, 2004). The nonthermal

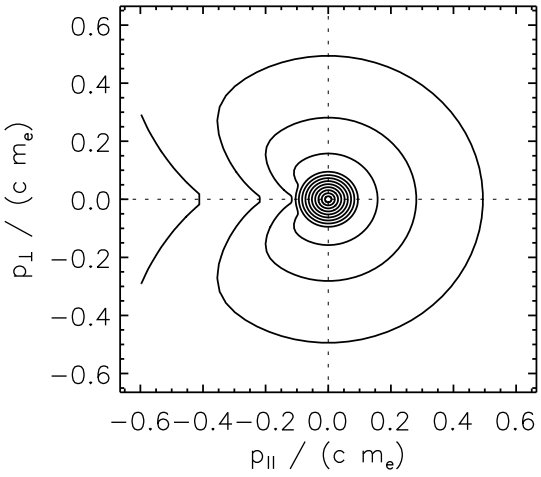


Figure 7.3: Electron model VDF for a loss-cone opening angle $\theta_\mathrm{L} = 40°$.

component of the electron VDF has a kappa distribution

$$f_\mathrm{h}(p) = \frac{N_\mathrm{h}\Gamma(\kappa+1)}{(\pi(2\kappa-3)p_\mathrm{th}^2)^{3/2}\Gamma(\kappa-1/2)}\left(1+\frac{p^2}{(2\kappa-3)p_\mathrm{th}^2}\right)^{-(\kappa+1)} \tag{7.1}$$

that results in a power law spectrum for high energies, where $p_\mathrm{th} = \sqrt{k_\mathrm{B}T_\mathrm{h}m_\mathrm{e}}$ is the "thermal momentum" of the electrons, and $\Gamma(x)$ the gamma function. For the calculations presented here, a value $\kappa = 4$ is chosen. This choice provides strong suprathermal tails of the VDF and agrees well with the power law coefficient $\delta = 3.8$ that can be derived (Brown, 1971) from the electron-flux spectrum in Fig. 7.1. The numerical values for the temperature and density of the hot component, $T_\mathrm{h} = 10^7$ K and $N_\mathrm{h} = 1.33 \cdot 10^9\,\mathrm{m}^{-3} = 10^{-6}\,N_\mathrm{b}$, are chosen in agreement with the RHESSI data.

Within the loss cone, the hot component vanishes. With $\theta_\mathrm{L}$ being the loss cone opening angle and $\Delta\theta$ the width of the transition from the loss cone to the undisturbed hot component, the total model electron VDF is defined as:

$$f(p,\theta) = f_\mathrm{b}(p) + \frac{1}{2}\left(1+\tanh\left(\frac{(\pi-\theta_\mathrm{L})-\theta}{\Delta\theta}\right)\right)f_\mathrm{h}(p). \tag{7.2}$$

The coordinate system is defined in such a way that the coordinate axis parallel to the background magnetic field points towards the loop footpoint where the mirroring and loss-cone formation takes place. This is why the loss cone is in the range of high pitch angles $\theta \approx \pi$, i.e. at negative $p_\parallel$. A loss-cone transition width $\Delta\theta = 10°$ is used here.

Figure 7.3 shows the model electron VDF for a loss-cone opening angle of $\theta_\mathrm{L} = 40°$. The thermal core and the extended hot component are both clearly visible, as is the loss cone. The model VDF covers electron energies up to 100 keV, that require the relativistic method for calculating wave growth rates.

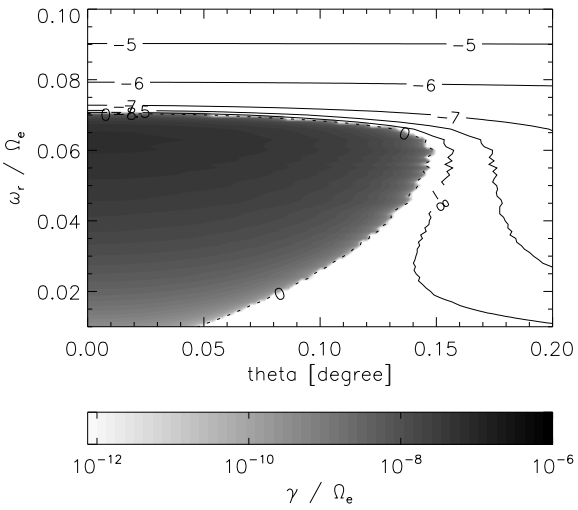


Figure 7.4: Growth rates for whistler waves as a function of wave frequency, $\omega_r$, and propagation angle, $\theta$. Positive growth rates, $\gamma > 0$, are displayed as a greyscale plot, and wave damping rates, $\gamma < 0$, by isolines marked with numbers that denote an exponent, e.g. -7 corresponds to $\gamma/\Omega_e = -10^{-7}$.

### 7.2.2 Whistler-wave growth rates

With this model electron VDF, it is possible to apply the method from chapter 5 to calculate the growth rates, $\gamma$, for whistler waves as a function of wave frequency, $\omega_r$, and wave propagation angle, $\theta$.

Figure 7.4 displays the whistler-wave growth rates that result from the electron VDF in Fig. 7.3. An area with positive $\gamma$, i.e. whistler-wave generation, can be seen clearly. But this area is limited both in frequency and wave-propagation angle. The frequencies with wave growth have an upper limit of approximately $\omega_{r,max} = 0.07\,\Omega_e$. The limit on the wave-propagation angle, $\theta < 0.15°$, is even more restrictive. Only whistlers that propagate almost parallel to the background magnetic field are generated.

These limits on $(\omega_r, \theta)$ are due to the shape of the electron VDF and the resonance condition, Eq. (5.8). The sign of the electron charge has been considered in the definition of the dielectric tensor in Eq. (5.6), $q_j = -e$. For waves that propagate parallel to the background magnetic field, the perpendicular wave number vanishes, $k_\perp = 0$. For these waves, only the resonance order $l = -1$ provides a contribution to the dispersion function, Eq. (5.5). For $l = -1$, it follows from the resonance condition, Eq. (5.8), that the momentum coordinate parallel to the background magnetic field, $p_\parallel$, is negative for an electron that is in resonance with a whistler wave with frequency $\omega_r$. The absolute value of $p_\parallel$ decreases as $\omega_r$ increases. At a frequency of $\omega_r = 0.07\,\Omega_e$ the resonance momentum $p_\parallel$ leaves the loss cone and enters the thermal core of the electron VDF that is clearly visible in Fig. 7.3. Since the electron VDF is Maxwellian there, there is no free energy available for wave growth, and the wave is strongly damped.

The resonance condition and the structure of the dielectric tensor is also the reason for the strict limitation of the wave growth to very small propagation angles $\theta < 0.15°$. For $k_\perp = 0$, only the

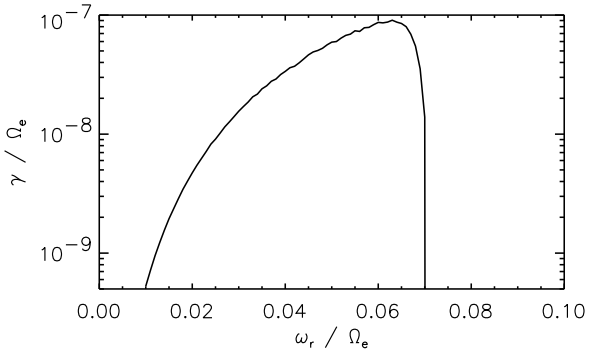


Figure 7.5: Wave growth rate, $\gamma$, as a function of the wave frequency, $\omega_r$, for waves propagating parallel to the background magnetic field.

resonance order $l = -1$ contributes to the dispersion function, but for $k_\perp \neq 0$, all $l = 0, \pm 1, \pm 2, \ldots$ provide a contribution. These contributions are of first or higher order in $k_\perp$ and thus seem to be small for small $k_\perp$, but nevertheless they can dominate the resulting wave growth rate. For $l = 0$, the nonrelativistic resonance condition simply reads $v_\parallel = \omega_r / k_\parallel \approx v_{\mathrm{ph}}$. Thus, an electron that moves with the wave phase speed is in the $l = 0$ resonance. For the model plasma, this speed corresponds to less than one electron thermal speed. Thus, the nonrelativistic limit may be used here, and the wave is in resonance with the thermal core of the electron VDF.

The integration over the resonance line in momentum space that leads to the "imaginary" part of the dielectric tensor, Eq. (5.13), now traverses the thermal core of the electron VDF for $l = 0$. The phase-space density is many orders of magnitude higher than in the loss cone where the integration path of the $l = -1$ resonance is located. As a result, the wave damping by the thermal core dominates the result for the wave growth rate, $\gamma$, even for very small propagation angles $\theta \approx 0.15°$.

### 7.2.3 Maximum wave growth rates

Due to this influence of other resonance orders than $l = -1$ for wave propagation angles $\theta > 0$, waves that propagate strictly parallel to the background magnetic field ($\theta = 0$) have the highest growth rates. In order to determine the maximum growth rate, $\gamma$ can be plotted as a function of the wave frequency, $\omega_r$, for a wave propagation angle $\theta = 0$. Figure 7.5 shows the wave growth rate for $\theta = 0$. For low frequencies, $\gamma$ increases with $\omega_r$. At $\omega_r = 0.063\,\Omega_\mathrm{e}$ it reaches a maximum and drops sharply at higher frequencies. This is due to the turn to negative $\gamma$ at $\omega_r = 0.07\,\Omega_\mathrm{e}$ that can be seen in Fig. 7.4.

The reason for this behavior is the above mentioned dependence of the resonance frequency on the electron speed or momentum coordinate parallel to the background magnetic field. The higher the wave frequency, the lower the absolute value of $p_\parallel$ ($p_\parallel < 0$). Thus, the integration path in the formula for the "imaginary" part of the dielectric tensor, Eq. (5.13), traverses regions with higher phase-space density as $\omega_r$ increases. Within the loss cone, this leads to an increase in the imaginary part of the dispersion function, and by means of Eq. (5.3) the wave growth rate increases. The maximum of $\gamma$ is reached when the resonance velocity enters the thermal core where there is no

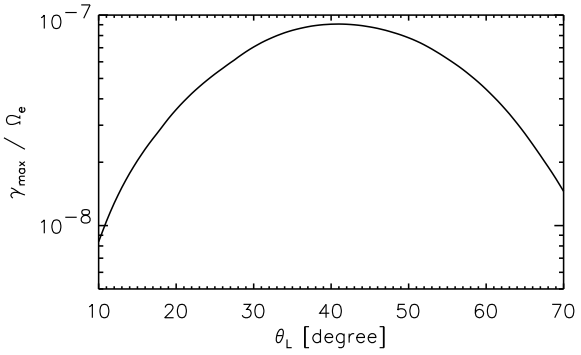


Figure 7.6: Maximum wave growth rate, $\gamma_{\max}$, as a function of the loss-cone opening angle, $\theta_{\mathrm{L}}$.

more loss cone VDF. For the model VDF, Fig. 7.3, this is the case for $p_{\parallel,\mathrm{res}} = 0.1\, m_{\mathrm{e}} c$. For higher frequencies, the waves interact with the thermal core and are damped, as described in the previous subsection.

Since the loss cone provides the free energy for whistler-wave growth, its opening angle is a critical parameter. In a coronal loop, the angle depends on the position along the loop and the magnetic-field structure of the loop. The results that have been presented so far have been calculated for an opening angle of $\theta_{\mathrm{L}} = 40°$. Figure 7.6 shows the maximum wave growth rate as a function of the loss-cone opening angle. It is no surprise that the wave growth vanishes if the loss cone disappears, $\theta_{\mathrm{L}} \to 0$. With growing $\theta_{\mathrm{L}}$, the maximum wave growth rate increases and reaches a maximum for $\theta_{\mathrm{L}} = 41°$. For even higher $\theta_{\mathrm{L}}$, the maximum $\gamma$ decreases. For very wide loss cones, there is a low phase-space density in a wide area of the momentum space, $p_{\parallel} < 0$, and Eq. (5.13) yields a smaller $\mathrm{Im}(\epsilon)$ and thus $\gamma$.

The results presented in this section show that whistler-wave generation by loss-cone distributions in flaring loops is well possible. The waves are generated with frequencies of less than one tenth of the electron cyclotron frequency. The corresponding wave velocities are in agreement with the observed intermediate frequency drift rates of fiber bursts (Kuijpers, 1975; Benz & Mann, 1998). Thus, whistler waves originating from electron loss cone VDFs can lead to the emission of fiber bursts.

Figure 7.6 also allows for a determination of the maximum wave growth rate, which is possible in the model plasma. This maximum value is $\gamma_{\max} = 9.1 \cdot 10^{-8}\, \Omega_{\mathrm{e}} = 4.8\, \mathrm{s}^{-1}$. This corresponds to a wave-growth timescale of a few tenths of a second. It is noteworthy that this result is based on the model assumption that the hot electron component has a number density of $N_{\mathrm{h}} = 10^{-6}\, N_{\mathrm{b}}$, with $N_{\mathrm{b}}$ being the density of the thermal background plasma. From the structure of the "imaginary" part of the dielectric tensor, Eq. (5.13), it follows that $\mathrm{Im}(\epsilon)$ is proportional to $N_{\mathrm{h}}$. Since it was found at the end of chapter 5 that the imaginary part of the dispersion function, $\mathrm{Im}(D)$, is of first order in $\mathrm{Im}(\epsilon)$, $\mathrm{Im}(D)$ and thus $\gamma$ scale linearly with $N_{\mathrm{h}}$. Thus, the assumption of e.g. $N_{\mathrm{h}} = 10^{-5}\, N_{\mathrm{b}}$ would result in a maximum wave growth rate of $48\, \mathrm{s}^{-1}$.

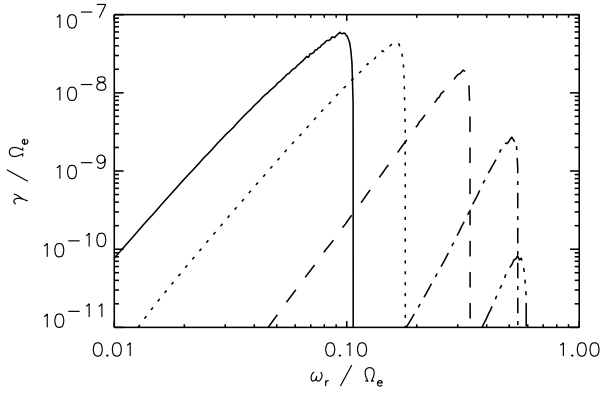


Figure 7.7: Wave growth rate, $\gamma$, as a function of the wave frequency, $\omega_r$, for a loss-cone opening angle $\theta_L = 40°$. The background magnetic field is $B = 4\,\mathrm{G}$ (solid line), $B = 6\,\mathrm{G}$ (dotted line), $B = 12\,\mathrm{G}$ (dashed line), $B = 29\,\mathrm{G}$ (dash-dotted line), and $B = 58\,\mathrm{G}$ (dash-dot-dotted line).

### 7.2.4 Magnetic field dependence

The results in the previous section have been calculated for a background magnetic field of $B = 3 \cdot 10^{-4}\,\mathrm{T}(3\,\mathrm{G})$ that is typical of the height within a coronal loop where the electron background density is $N_b = 1.33 \cdot 10^{15}\,\mathrm{m}^{-3}$, which corresponds to a plasma frequency of $f_p = 327\,\mathrm{MHz}$ where fiber bursts are usually observed (Aurass et al., 2005). This magnetic field and plasma density lead to a ratio of $\omega_p/\Omega_e = 39$ that is normal for the solar corona (Vocks & Mann, 2004).

The choice of $B$ and therefore $\Omega_e$ determines an important plasma parameter. Thus it is worthwhile to study the effect of this choice on the efficiency of the whistler-wave generation. Since the frequency of fiber bursts corresponds to the local plasma frequency at their source region (Kuijpers, 1975), $\omega_p/\Omega_e > 1$ is a necessary condition for their generation and subsequent observation on Earth, which imposes an upper limit on the magnetic field. On the other hand, the stability of the magnetic loop requires that the ratio between the plasma's thermal gas pressure and the energy density of the magnetic field, i.e. the plasma beta, is less than unity, $\beta < 1$. This leads to a lower limit for $B$. In the model plasma, $\beta \approx 1$ for $B = 3 \cdot 10^{-4}\,\mathrm{T}$, or 3 G, so only stronger $B$ and thus lower ratios $\omega_p/\Omega_e$ are studied here. Since it has been found above that the whistler-wave growth is strongest for waves propagating parallel to the background magnetic field, only this propagation direction is considered.

A series of calculations is performed with magnetic fields of $B = 4$, 6, 12, 29, and 58 G, that correspond to ratios $\omega_p/\Omega_e = 30$, 20, 10, 4, and 2; see also Table 7.1 below. The electron VDF is in all cases the one from Eq. 7.2 with a thermal background component and a hot, nonthermal component with a loss cone that has an opening angle of $\theta_L = 40°$. The VDF has been plotted in Fig. 7.3.

Figure 7.7 displays the growth rates of whistler waves for the different magnetic fields as functions of the wave frequency. It is evident that the wave frequencies shift towards the electron cyclotron frequency, $\Omega_e$, with increasing $B$. This is a consequence of the whistler-wave phase speed increasing with $B$. It was noted in the previous section that the maximum wave growth rate is reached for waves that are in resonance with electrons with a momentum of $p_\parallel = 0.1 m_e c$. For a given $p_\parallel$, the

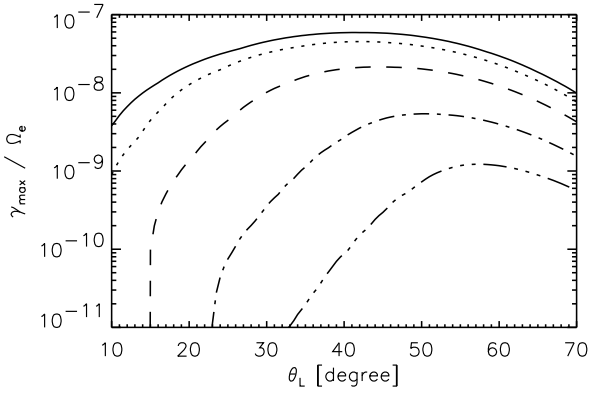


Figure 7.8: Maximum wave growth rate, $\gamma_{\max}$, as a function of the loss-cone opening angle, $\theta_{\rm L}$, for background magnetic fields of $B = 4\,{\rm G}$ (solid line), $B = 6\,{\rm G}$ (dotted line), $B = 12\,{\rm G}$ (dashed line), $B = 29\,{\rm G}$ (dash-dotted line), and $B = 58\,{\rm G}$ (dash-dot-dotted line).

Doppler shift of the resonance frequency, $\omega_{\rm res}$, decreases with increasing wave phase speed, and thus $\omega_{\rm res}$ approaches $\Omega_{\rm e}$ as $B$ increases.

From Fig. 7.7 it also can be seen that the maximum values of $\gamma/\Omega_{\rm e}$ only slightly decrease with $B$ for the first three values of $B$, where the limit $\omega_{\rm p}/\Omega_{\rm e} \gg 1$ is still a valid approximation. But for $B = 29\,{\rm G}$ and even more for $B = 58\,{\rm G}$, i.e. $\omega_{\rm p}/\Omega_{\rm e} = 2$ and thus close to unity, the growth rate drops sharply. So the whistler-wave generation mechanism seems to be less efficient for small $\omega_{\rm p}/\Omega_{\rm e}$.

The results shown in Fig. 7.7 were obtained for a loss-cone opening angle of $\theta_{\rm L} = 40^\circ$. It is interesting to investigate the dependence of the maximum wave growth rate on $\theta_{\rm L}$ as $B$ is varied. Figure 7.8 shows these rates for the different magnetic fields as functions of the loss-cone opening angle. It is found again that for weak magnetic fields and thus high $\omega_{\rm p}/\Omega_{\rm e} \gg 1$ there is little variation with $B$. The overall maximum of $\gamma$ is reached for loss-cone opening angles in the range $\theta_{\rm L} = 40 - 50^\circ$, and $\gamma_{\max}/\Omega_{\rm e}$ decreases slightly with $B$. But as soon as the limit $\omega_{\rm p}/\Omega_{\rm e} \gg 1$ is no longer valid, i.e. for $B = 29\,{\rm G}$ and higher, $\gamma_{\max}$ drops sharply. The decrease is stronger for small opening angles, $\theta_{\rm L} < 40^\circ$, than for large angles, $\theta_{\rm L} > 50^\circ$. As a consequence, the maximum value of $\gamma_{\max}$ shifts towards higher $\theta_{\rm L}$.

In Figs. 7.7 and 7.8 the maximum wave growth rate has been displayed in a normalized form, $\gamma_{\max}/\Omega_{\rm e}$. But since $\Omega_{\rm e}$ is proportional to $B$, it is illustrative to look at the maximum wave growth rate that is possible in the model plasma in absolute units. Table 7.1 shows the maximum values for $\gamma_{\max}$ for the different magnetic fields. For small $B$ and correspondingly high $\omega_{\rm p}/\Omega_{\rm e}$, $\gamma_{\max}$ has values around $4.5\,{\rm s}^{-1}$. These numbers agree with the $\gamma_{\max} = 4.8\,{\rm s}^{-1}$ that has been found in the previous section for $B = 3\,{\rm G}$, so the increase in $\Omega_{\rm e}$ with increasing $B$ compensates the slight decrease of $\gamma_{\max}/\Omega_{\rm e}$ for small $B$ in Fig. 7.8. It can thus be concluded that the wave growth rates are fairly insensitive to the magnetic field of the loop. But for higher $B$, where $\omega_{\rm p}/\Omega_{\rm e}$ approaches unity, the maximum wave growth rate still drops with increasing $B$, albeit not as strongly as indicated by Fig. 7.8. The whistler-wave generation mechanism becomes less efficient for small $\omega_{\rm p}/\Omega_{\rm e}$.

Table 7.1: Maximum wave growth rates, $\gamma_{max}$, for different $B$

| $B$(G) | $\omega_p/\Omega_e$ | $\gamma_{max}(s^{-1})$ |
|---|---|---|
| 4 | 30 | 4.2 |
| 6 | 20 | 4.8 |
| 12 | 10 | 4.5 |
| 29 | 4 | 2.8 |
| 58 | 2 | 1.2 |

## 7.3 Conclusions and summary

In this chapter the generation of whistler waves by electron loss-cone distributions, as they form in coronal loops during solar flares, has been studied. The main objective was to investigate whether the resulting whistler-wave growth is fast enough to account for the generation of fiber bursts as they are observed in solar dynamic radio spectra during such events. The wave growth rates, $\gamma$, that are caused by a given electron VDF, were determined as a function of the wave frequency, $\omega_r$, and propagation angle, $\theta$, towards the background magnetic field. Due to the Taylor expansion of the dispersion function, Eq. (5.3), this method is especially appropriate for low wave growth rates, $\gamma \ll \omega_r$.

Plotting the wave growth rate as a function of $\omega_r$ and $\theta$ clearly shows a region of wave growth. Investigation of the dependence of $\gamma$ on the propagation angle is especially interesting. It demonstrates the important role of higher order resonances even for very small $\theta$. An analytical calculation that considers only the case $\theta = 0$ cannot reveal this restriction on the whistler-wave growth.

This result has some implications for the standard model of fiber-burst generation. If a whistler wave has been generated with a propagation angle $\theta = 0$, where the wave growth is strongest, it propagates along the background magnetic field. But the loop is curved, so that a wave vector that is initially parallel to the magnetic field will deviate from $\vec{B}$ some time later. But if the index of refraction inside the loop decreases towards the lateral boundary of the loop (Kuijpers, 1975; Roberts, 2000), the wave is refracted back towards the magnetic-field lines. Thus, the whistler wave is forced along the loop, and the wave growth can continue for a sufficient time despite the strong limitation to small propagation angles.

Since whistler waves that propagate along the background magnetic field with $\theta = 0$ have the highest growth rates, it is sufficient to study this case while looking for the maximum value of $\gamma$ in the model plasma. At low frequencies, $\gamma$ increases with increasing $\omega_r$ since the electron momentum needed to fulfill the resonance condition, Eq. 5.8, decreases. In momentum space, the resonance moves towards regions with higher electron phase-space density. But as soon as the resonance reaches the thermal core of the VDF, the growth rate reaches a maximum value $\gamma_{max}$ and drops sharply at higher frequencies. This course defines the maximum wave growth rate for the given electron distribution.

The maximum value of $\gamma$ that is found in the model plasma varies with the opening angle of the loss cone. The absolute maximum is reached at 41°, with $\gamma_{max} = 9.1 \cdot 10^{-8}\,\Omega_e = 4.8\,s^{-1}$, where $\gamma_{max}$ has values of more than $4\,s^{-1}$ over a wide range of loss cone opening angles from $32° - 50°$. Since

fiber bursts are believed to be generated by the interaction between whistlers and electrostatic modes, their pulse duration at a fixed frequency should not be less than the growth time of the whistler wave. Observations (Aurass et al., 2005) show pulse durations of some tenths of a second at 327 MHz . Thus, the values of $\gamma_{\max}$ indicate a whistler-wave growth that is fast enough to account for the observed pulse durations. These values are based on the assumption that the hot, nonthermal component of the electron distribution has a low number density $N_{\rm h} = 10^{-6}\, N_{\rm b}$, with $N_{\rm b}$ being the density of the background electrons. A higher $N_{\rm h}$ would lead to higher growth rates.

A study of the whistler wave generation for different magnetic fields shows that the maximum wave growth rate is fairly independent of $B$ as long as $B$ is small enough so that $\omega_{\rm p}/\Omega_{\rm e} \gg 1$ is a valid assumption. The dependence of $\gamma_{\max}$ on the loss-cone opening angle also hardly depends on $B$ in this regime. But for higher $B$ with $\omega_{\rm p}/\Omega_{\rm e} \approx 1$, the growth rates decrease rapidly. However, this finding has no implications for the wave generation in the solar corona where the condition $\omega_{\rm p}/\Omega_{\rm e} \gg 1$ is normally met. Thus, the wave generation does not depend critically on the actual value of the background magnetic field. The whistler-wave growth is fast enough to account for the observed fiber bursts over a wide range of magnetic fields and loss-cone opening angles. This result corroborates the present model (Aurass et al., 2005) of fiber bursts as being caused by whistler-wave packets traveling along a magnetic loop.

# Part III

# Conclusions and future perspectives

# Chapter 8

# Conclusions

## 8.1 Electron kinetics in the solar corona and wind

The topic of this thesis is the pivotal role of electron kinetics for the physical processes in the solar corona and wind. The low density of the plasma leads to weak coupling between particles, both electrons and ions, due to Coulomb collisions, and thereby enables the formation of states far away from local thermodynamic equilibrium and its nearly Maxwellian velocity distribution functions (VDFs). In the solar corona, this can be observed as differential heating of ion species, accompanied by strong temperature anisotropies. In the solar wind, in-situ observations reveal VDFs that differ significantly from Maxwellians. Therefore, a fluid description of the plasma is not able to provide an adequate description of the underlying physical processes.

Instead of fluid models, kinetic theory that considers electron VDFs is needed. The comparison of simple exospheric kinetic solar wind models with observational data reveals that solar wind electrons must experience some pitch-angle scattering. The conservation of magnetic momentum on their way from the corona into interplanetary space would otherwise focus all solar wind electrons into an extremely narrow beam. This is in contrast to the observations of a thermal core, an extended isotropic halo, and anisotropic, anti-sunward "strahl" in the solar wind. The kinetic model presented in chapter 2.4 provides this electron diffusion by means of resonant interaction with whistler waves. The whistler wave spectrum is based on observations of power spectra of magnetic field fluctuations in interplanetary space. The interaction between electrons and whistlers is described within the framework of quasi-linear theory. The main effect of a given wave spectrum on an electron VDF is pitch-angle scattering in the wave reference frame. This is a fundamental process with many implications in space plasma physics, as shown in the subsequent chapters of this thesis. The electron VDFs found by the model reproduce the typical features of observed solar wind VDFs, i.e. the thermal core, isotropic suprathermal halo, and "strahl" directed away from the Sun.

So scattering of electrons by plasma waves is an important process in the solar wind that shapes interplanetary electron VDFs. But this should not only affect thermal and suprathermal electrons in the quiet solar wind, but also the energetic eletrons that are produced and released in solar flares. These electrons propagate through interplanetary space where they can be observed in-situ, often by satellites at 1 AU. It is a straightforward expectation that scattering by whistler waves delays

their arrival times at the spacecraft. Since inferred release times at the Sun are based on velocity-dependent arrival times, one might assume that scattering could explain the time differences of up to 10 minutes between the onset of X-ray and radio emission of a flare, that reveals energetic electron production, and the inferred release times in the solar corona. But on the other hand, the energy dependence of electron arrival times at 1 AU is often found to be in agreement with free electron propagation. In chapter 3 a detailed study on the influence of whistler wave scattering on flare electrons has been presented. The results show that pitch-angle scattering by whistler waves can delay electron arrival times up to 1 minute. However, the whistlers also re-distribute electrons from higher to lower energies, thereby leading to apparent early arrival of electrons with a given energy, as compared to the free-flight arrival time. Both effects have been found to just compensate each other under typical solar wind conditions. This result offers an explanation why the assumption of free electron propagation in interplanetary space seems to work well in analyzing solar energetic particle data, despite the strong scattering they encounter on their way from the Sun to the Earth.

This electron diffusion in energy is a first hint on the importance of the difference between the wave and the plasma reference frame. The whistler - electron interaction leads to pitch-angle diffusion of electrons in the wave frame, with no change of electron speed, i.e. energy. But the wave frame differs from the plasma frame by the wave phase speed. In the plasma frame, the diffusion does change electron energies. In the solar wind with its low whistler phase speed this was a small, but nevertheless important effect.

The energy change becomes stronger when whistler phase speeds are higher. This is the case in the solar corona where whistlers can bring electrons from low speeds parallel to the background magnetic field to high speeds perpendicular to it. This has the consequence that a whistler wave spectrum can produce a suprathermal electron population even under quiet solar conditions. In chapter 4.3 it has been studied how this effect increases the flux of suprathermal electrons in the solar wind, and in chapter 4.4 detailed simulations of suprathermal electron production in the almost closed plasma volume of a coronal loop have been presented. The results show that electron acceleration takes place near the loop footpoints where wave phase speeds are highest, while pure pitch-angle diffusion dominates near the loop top. The initially Maxwellian electron VDF develops suprathermal tails in the energy range of several keV, that can be fitted by a kappa distribution.

The whistler wave spectrum fed into the corona is closely related to the waves that are expected to be responsible for coronal heating and also play a role in solar wind acceleration. So the main result of this thesis is that the processes of coronal heating, solar wind acceleration, and suprathermal electron production are based on a common mechanism. It can be expected to operate in any star that has a hot corona, not only the Sun. This kinetic process is of general significance for solar-stellar connections.

## 8.2 Kinetic plasma instabilities

Kinetic models like the Vlasov code presented above provide detailed information on electron VDFs in a plasma. They allow for a description of states far away from thermal equilibrium, with non-Maxwellian VDFs. With electron VDFs at hand, the stability properties of a plasma

can be investigated by calculating wave growth and damping rates. Methods of doing so are well known, mainly by calculating the complex dispersion function of waves in the plasma. An implementation of such a method has been presented in this thesis. It covers relativistic electron energies and yields wave growth/damping rates as functions of frequency or wavenumber and wave propagation direction.

As examples, instabilities related to electron loss-cone VDFs have been investigated. A loss-cone VDF forms when electrons move sunwards in the corona. As they go down, the local magnetic field increases. Due to the conservation of magnetic moment they are mirrored and reflected back upwards. The smaller the initial pitch-angle of the electron, the deeper an electron can penetrate into the lower solar atmosphere. Those with the smallest pitch-angles can reach the cooler and denser transition region or even the chromosphere, where they are scattered and thermalized by Coulomb collisions with the ambient plasma. Thus, they don't return into the corona. This forms a "loss cone" in the reflected part of the electron distribution that is characterized by a reduced phase-space density for small pitch-angles. Loss-cone VDFs provide free energy for wave growth, i.e. plasma instabilities.

An important parameter for this wave growth is the ratio $\omega_p/\Omega_e$ between the plasma and electron cyclotron frequency. Wheter it is greater or less than unity determines which wave modes are excited.

At first, the case $\omega_p/\Omega_e < 1$ is studied. In such a plasma, the electron cyclotron maser mechanism can lead to X-mode emission directed nearly perpendicular to the background magnetic field. Such waves are well known from planetary radio emission, e.g. Jupiter's dekametric radio bursts or Earth's auroral kilometric radiation. In chapter 6 it has been investigated if this also can happen in the solar corona.

A loss-cone VDF can form under quiet solar conditions in the opening magnetic field structure of a coronal funnel, that is located in the low corona directly above the transition region where the magnetic field rapidly expands from the borders of supergranular cells. Near the coronal base, the magnetic field is still strong, so that the $\omega_p/\Omega_e < 1$ condition is met in the lowest part of the funnel. The loss-cone VDF there can be calculated by the kinetic model presented in the first part of this thesis.

The results of the stability analysis show no wave generation on the fundamental mode, $\omega = \Omega_e$, since this requires $\omega_p/\Omega_e \ll 1$ that is not met here. But some emission at the first harmonic, $\omega = 2\,\Omega_e$, has been found, although it was very weak. The X-mode wave is an electromagnetic wave that in principle could freely propagate away from the corona and be observed on Earth. However, as the wave propagates upward in the corona, it traverses regions with lower magnetic field. So eventually it meets the next higher resonance condition, $\omega = 3\,\Omega_e$, where it suffers absorption by the thermal core of the local electron VDF. The wave damping rate there is much higher than the growth rate in the source region, so the wave is completely absorbed. It has to be concluded that cyclotron maser emission from the Sun cannot be observed under quiet solar conditions.

This is different for the $\omega_p/\Omega_e > 1$ case. In such a plasma, an electron loss-cone VDF leads to the emission of whistler waves. $\omega_p/\Omega_e > 1$ is more typical for the solar corona outside coronal funnels. A loss-cone VDF there can form during solar flares, when e.g. a coronal loop is filled with

electrons in the energy range of 10s of keV, that are not as quickly thermalized as the suprathermal electrons discussed in the $\omega_p/\Omega_e < 1$ case. Whistler waves can only propagate within their plasma environment, so coronal whistlers cannot be directly observed from Earth. But they reveal their existence through so-called fiber bursts, that are fine structures in solar dynamic radio spectra during flares, with frequency drift rates in agreement with the group velocities of whistlers propagating through the corona. In chapter 7 a study on the growth rates of whistlers in a flare electron VDF based on X-ray data for different magnetic fields and loss-cone opening angles has been presented. Whistler wave growth is restricted to small angles between the wave vector and the magnetic field, but this is not a problem since whistlers propagating in a coronal loop can be refracted towards the loop center. The highest wave growth rates are found for intermediate loss-cone opening angles, which is not a suprise since this maximizes the available free energy. The maximum wave growth rates found in the plasma are suprisingly insensitive to the magnetic field. With gamma of the order of $4\,s^{-1}$, the wave growth is fast enough to account for the observed fiber burst pulse durations of a few tenths of seconds.

These examples of loss-cone related plasma instabilities show that the combination of kinetic simulations, yielding information on electron VDFs in space plasmas inaccessible to in-situ observations, with studies of kinetic instabilities offers fundamental new insights into the micro-physical plasma processes in stellar atmospheres and interplanetary space.

# Chapter 9

# Future perspectives

The combination of kinetic models based on a Boltzmann-Vlasov code with analyses of plasma instabilities is a versatile tool that offers many possibilities for further investigation of space plasma processes on a microscopic scale. It is a significant step beyond fluid descriptions of the plasma, like MHD, and is well suited for studies of the solar atmosphere.

## 9.1 Solar wind models

The strongest model assumption in the kinetic solar wind model presented in this thesis is the exclusive consideration of waves propagating parallel to the background magnetic field. It leads to the problem of low diffusion across $p_{\parallel} = 0$, where the resonance frequency of electrons equals the electron cyclotron frequency. This assumption can be overcome by the inclusion of oblique waves. However, this leads to an integral over wave-vector space that is not practical for numerical methods (Marsch & Tu, 2001). So alternative approaches are necessary.

Adopting the diffusion coefficients from more general plasma turbulence models seems to be a promising avenue (Pierrard et al., 2011). These coefficients for the solar wind could e.g. be derived from cosmic ray studies (Schlickeiser, 2002). Such an improved model can be applied on studies of both the quiet solar wind and flare electron propagation in interplanetary space.

## 9.2 Solar energetic electrons

For the propagation of solar energetic electrons in interplanetary space, the influence of Coulomb collisions on electrons with energies of just a few keV is an interesting research subject of its own. The scattering of these electrons reduces their energy, thus leading to an apparent early arrival in the same way as does the scattering by whistlers waves, that compensates the delay caused by pitch-angle scattering.

An important improvement of the flare electron propagation model is the inclusion of Langmuir waves. The interplanetary electron VDFs found in the simulation with flare electrons already being

present at higher energies and just the thermal background at lower energies show a strong positive slope $\partial f/\partial p_{\|}$ that is unstable towards the generation of Langmuir waves. These electrostatic waves act back on the electron VDF by effectively transporting electrons to lower energies and eroding the region of the VDF with $\partial f/\partial p_{\|} > 0$, thus forming a plateau of constant phase-space density. The effects of plateau formation and electron beam regeneration due to velocity dispersion compete with each other, thereby determining the production rate of Langmuir waves.

The Langmuir waves are electrostatic oscillations that only can be observed in-situ but not remotely from Earch. However, they can couple to low-frequency plasma waves, leading to the emission of electromagnetic waves that are observed as type III radio bursts (Suziki & Dulk, 1985). With such an extension, the kinetic model of flare electron propagation can be used for detailed studies of type III radio bursts.

## 9.3 Plasma instabilities

Calculating the growth of Langmuir waves is just one example for studies of plasma instabilities. The method of calculating plasma wave growth and damping rates presented in chapter 5 is a general-purpose tool that can be applied on many space plasmas with free energy available for wave generation. The generation of electromagnetic waves due to electron loss-cone distributions for different plasma environments has been discussed as examples in this thesis.

Future applications include studies relevant for the particle acceleration mechanism in solar flares. This includes the investigation of possible whistler-wave production by flare-generated protons, or the role of ion-acoustic waves after shock-drift acceleration of protons (Miteva et al., 2007).

This tool enables estimates of the efficiency of wave generation whenever an observed or model particle VDF is available. This is useful for a combined analysis of data from different wavelengths. X-ray observations, e.g. by RHESSI or the STIX imager onboard the upcoming Solar Orbiter, reveal the existence of energetic electrons in the corona. Observations at optical wavelengths, e.g. with the new GREGOR telescope, show their effect on the chromosphere and photosphere, while radio maps of the Sun, e.g. by the LOFAR (LOw Fequency ARray) telescope, allow for modeling the propagation of flare electrons and the instabilities that lead to radio wave emission.

With these new methods and observations at hand, exciting new discoveries are waiting to be made.

# Bibliography


Aurass, H., in *Coronal Physics from Radio and Space Observations*, Ed. G. Trottet, Lecture Notes in Physics, Springer, Heidelberg (1996)

Aurass, H., Rausche, G., Mann, G., and Hofmann, A., Astron. Astrophys., **435**, 1137 (2005)

Baumjohann, W. and Treumann, R. A., Basic Space Plasma Physics, Imperial College Press, London (1996)

Benz, A. O. and Mann, G., Astron. Astrophys, **333**, 1034 (1998)

Bieber, J. W., Matthaeus, W. H., Smith, C. W., Wanner, W., Kallenrode, M.-B., and Wibberenz, G., Astrophys. J., **420**, 294 (1994)

Brown, J. C., Solar Phys., **18**, 489 (1971)

Cane, H. V., Astrophys. J., **598**, 1403 (2003)

Classen, H. T., Mann, G., Klassen, A., and Aurass, A., Astron. Astrophys, **409**, 309 (2003)

Conway, A. J. and Willes, A. J., Astron. Astrophys., **355**, 751 (2000)

Cranmer, S. R., Field, G. B., and Kohl, J. L., Astrophys. J., **518**, 937 (1999)

Croley, D. R., Jr., Mizera, P. F., Fennell, J. F., J. Geophys. Res., **83**, 2701 (1978)

Dorelli, J. C. and Scudder, J. D., J. Geophys. Res. **108**, doi: 10.1029/2002JA009484 (2003)

Dröge W., Astrophys. J., **589**, 1027 (2003)

Esser, R., and Edgar, R. J., Astrophys. J., **532**, L71 (2000)

Gabriel, A. H., Phil. Trans. R. Soc. London, Ser. A, **281**, 339 (1976)

Gopalswamy, N., Shibasaki, K., Thompson, B. J., Gurman, J. B, and Deforest, C. E. 1999, in *In Proceedings of the Ninth International Solar Wind Conference*, AIP Conference Proceedings, p. 277 (1999)

Hackenberg, P., Marsch, E., and Mann, G., Astron. Astrophys. **360**, 1139 (2000)

Haggerty, D. K. and Roelof, E. C., Astrophys. J., **579**, 841 (2002)

Hammond, C. M., Feldman, W. C., McComas, D. J., Phillips, J. L., and Forsyth, R. J., Astron. Astrophys. **316**, 250 (1996)

Hansteen, V.H. and Leer, E., J. Geophys. Res. **100**, 21577 (1995)

He, J.-S., Tu, C.-Y., and Marsch, E., Solar Phys. **250**, 147 (2008)

Helliwell, R. A., Phil. Trans. Roy. Soc. London A, **280**, 137 (1975)

Hollweg, J. V., J. Geophys. Res., **111**, doi:10.1029/2006JA011917 (2006)

Holman, G. D., Sui, L., Schwartz, R. A., and Emslie, A. G., Astrophys. J., **595**, L97 (2003)

Hu, Y. Q., Habbal, S. R., and Li, X., J. Geophys. Res., **104**, 24819 (1999)

Hu, Y.Q., Esser, R., and Habbal, S. R., J. Geophys. Res. **105**, 5093 (2000)

Isenberg, P. A., Lee, A. M., and Hollweg, V. J., J. Geophys. Res. **106**, 5649 (2001)

Jockers, K., Astron. Astrophys. **6**, 219 (1970)

Karlický, M., Fárník, F., and S. Krucker, Astron. Astrophys. **419**, 365 (2004)

Kennel, C. F. and Engelmann, F., Phys. Fluids **9**, 2377 (1966)

Klassen, A., Bothmer, V., Mann, G., Reiner, M. J., Krucker, S., Vourlidas, A., and Kunow, H. 2002, Astron. Astrophys, **385**, 1078 (2002)

Klein, K.-L., Krucker, S., Trottet, G., and Hoang, S. 2005, Astron. Astrophys., **431**, 1047, (2005)

Kohl, J. L., Noci, G., Antonucci, E., Tondello, G., Huber, M.C.E., Cranmer, R., Strachan, L., Panasyuk, A. V., Gardner, L. D., Romollo, M., Fineschi, S., Dobrzycka, D., Raymond, J. C., Nicolosi, P., Siegmund, O.H.W., Sparado, D., Benna, C., Ciaravella, A., Giordano, S., Habbal, S. R, Karovska, M., Li, X., Martin, R., Michels, J. G., Mondigliani, A., Naletto, G., O´Neal, R. H., Pernechele, C., Poletto, G., Smith, P. L., and Suleiman, R. M., Astrophys. J. **501**, L121 (1998)

Kosugi, T., Ishiguro, M., and Shibasaki, K., Publ. Astron. Soc. Japan, **38**, 1 (1986)

Krucker, S., Larson, D., and Lin, R. P., Astrophys. J., **519**, 864 (1999)

Krucker, S., Kontar, E. P., Christe, S., and Lin, R. P., **663**, L109, doi: 10.1086/519373 (2007)

Kuijpers, J., Solar Phys., **44**, 173 (1975)

Ladreiter, H. P., Astrohpys. J., **370**, 419 (1991)

Landi, S., and Pantellini, F., Astron. Astrophys. **400**, 769 (2003)

Leamon, R. J., Smith, C. W., Ness, N. F., Matthaeus, W. H., and Wong, H. K., J. Geophys. Res., **103**, 4775 (1998)

Lie-Svendsen, Ø., Hansteen, V. H., and Leer, E., J. Geophys. Res. **102**, 4701 (1997)

Lie-Svendsen, Ø, and Leer, E., J. Geophys. Res. **105**, 35 (2000)

Lin, N., Kellogg, P. J., MacDowall, R. J., Scime, E. E., Balogh, A., Forsyth, R. J., McComas, D. J., and Phillips, J. L., J. Geophys. Res., **103**, 12023 (1998)

Lin, R. P., Space Sci. Rev. **16**, 189 (1974)

Lin, R. P., Levedahl, W. K., Lotko, W., Gurnett D. A., and Scarf, F. L., Astrophys. J., **308**, 954 (1986)

Lin, R. P., Anderson, K. A., Ashford, S., Carlson, C., Curtis, D., Ergun, R., Larson, D., McFadden, J., McCarthy, M., Parks, G. K., Rème, H., Bosqued, J. M., Coutelier, J., Cotin, F., D'Uston, C., Wenzel, K.-P., Sanderson, T. R., Henrion, J., Ronnet, J. C., Paschmann, G. 1995, Space Sci. Rev., **71**, 125 (1995)

Lin, R. P., Space Sci. Rev., **86**, 61 (1998)

Lin, R. P., Dennis, B. R., Hurford, G. J., and 63 co-authors, Solar Phys. **210**, 3 (2002)

Lin, R. P., Krucker, S., Hurford, G. J., Smith, D. M., Hudson, H. S., Holman, G. D., Schwartz, R. A., Dennis, B. R., Share, G. H., Murphy, R. J., Emslie, A. G., Johns-Krull, C., and Vilmer, N., Astrophys. J., **595**, L69 (2003)

Ljepojevic, N. N. and Burgess, A., Proc. R. Soc. Lond. A, **428**, 71 (1990)

Maksimovic, M., Pierrard, V., and Riley, P., Geophys. Res. Lett. **24**, 1151 (1997)

Maksimovic, M., Zouganelis, I., Chaufray, J.-Y., Issautier, K., Scime, E. F., Littleton, J. E., Marsch, E., McComas, D. J., Salem, C., Lin, R. P., and Elliott, H., J. Geophys. Res. **110**, 9104 (2005)

Mangeney, A., Salem, C., Veltri, P. L., and Cecconi, B., *Intermittency in the Solar Wind Turbulence and the Haar Wavelet Transform*, Sheffield Space Plasma Meeting: Multipoint Measurements versus Theory, ESA SP-492, 53 (2001)

Mann, G., Karlický, M., and Motschmann, U., Solar Phys., **110**, 381 (1987)

Mann, G., Baumgaertel, K., Chernov, G. P., and Karlický, M., Solar Phys., **120**, 383 (1989)

Mann, G., Aurass, H., Voigt, and W., Paschke, J., Proc. First SOHO Workshop, ESA SP-348, 129 (1992)

Mann, G., Classen, T., and Aurass, H., Astron. Astrophys. **295**, 775 (1995)

Marsch, E., Nonlinear Proc. in Geophys., **5**, 111 (1998)

Marsch, E., Nonlinear Proc. Geophys., **9**, 69 (2001)

Marsch, E. and Tu, C.-Y., J. Geophys. Res. **106**, 227 (2001)

Marsch, E., Living Reviews in Solar Phys. **3** (2006)

Matsuda, Y., Smith, G. R., J. Comp. Phys., **100**, 229 (1992)

Matthaeus, W. H., Goldstein, M. L., and Roberts, D. A., J. Geophys. Res., **95**, 20673 (1990)

Melrose, D. B., Plasma Astrophysics, Gordon and Breach, New York (1980)

Melrose, D. B., Dulk, G. A., Astropys. J., **259**, 844 (1982)

Melrose, D. B., Hewitt, R. G., and Dulk, G. A., J. Geophys. Res., **89**, 897 (1984)

Melrose, D. B., Instabilities in Space and Laboratory Plasmas, Cambridge University Press, Cambridge (1986)

Miteva, R., Mann, G., Vocks, C., and Aurass, H., Astron. Astrophys., **461**, 1127, doi: 10.1051/0004-6361:20053736 (2007)

Montgomery, D. C. and Tidman, D. A., Plasma Kinetic Theory, McGraw-Hill, New York (1964)

Moran, T., Gopalswamy, N., Dammasch, I. E., and Wilhelm, K., Astron. Astrophys., **378**, 1037 (2001)

Nelson, G. J. and Melrose, D. B., in *Solar Radiophysic*, Ed. D. J. McLean and N. R. Labrum, Cambridge Univ Press, Cambridge (1985)

Nieves-Chinchilla, T. and Viñas, A. F., J. Geophys. Res. **113**, doi: 10.1029/2007JA012703 (2008)

Ofman, L., J. Geophys. Res. **109**, 7102 (2004)

Omidi, N., Gurnett, D. A., and Wu, C. S., J. Geophys. Res., **89**, 883 (1984)

Owens, M. J., Crooker, N. U., and Schwadron, N. A., J. Geophys. Res. **113**, 11104 (2008)

Pagel, C., Gary, S. P., de Koning, C. A., Skoug, R. M., and Steinberg, J. T., J. Geophys. Res. **112**, 4103 (2007)

Parker, E. N., Astrophys. J. **128**, 664 (1958)

Pierrard, V., Maksimovic, M., and Lemaire, J., J. Geophys. Res. **104**, 17021 (1999)

Pierrard, V., Maksimovic, M., and Lemaire. J., J. Geophys. Res. **106**, 29305 (2001)

Pierrard, V., Lazar, M., and Schlickeiser, R., Solar Phys. **269**, 421, doi: 10.1007/s11207-010-9700-7 (2011)

Pilipp, W. G., Miggenrieder, H., Montgomery, M. D., Mühlhäuser, K. H., Rosenbauer, H., and Schwenn, R., J. Geophys. Res. **92**, 1075 (1987)

Roberts, B., Solar Phys., **193**, 139 (2000)

Rosenbauer, H., Schwenn, R., Marsch, E., Meyer, B., Miggenrieder, H., Montgomery, M. D., Mühlhäuser, K. H., Pilipp, W., Voges, W., and Zink, S. M., J. Geophys. Zeitschrift Geophysik, **42**, 561 (1977)

Sakurai, T., Solar Phys., **76**, 301 (1982)

Salem, C., PhD thesis, Univ. Paris (2000)

Scharer, J. E., and Trivelpiece, A. W., Phys. Fluids, **10**, 591 (1967)

Schlickeiser, R., Cosmic Ray Astrophysics, Springer, Berlin (2002)

Schwenn, R., Space Sc. Rev. **44**, 139 (1986)

Scudder, J. D., Astrophys. J. **398**, 299 (1992a)

Scudder, J. D., Astrophys. J. **398**, 319 (1992b)

Seehafer, N., Solar Phys., **58**, 215 (1978)

Spitzer, L. and Härm, R., Phys. Rev. **89**, 977 (1953)

Štverák, Š., Maksimovic, M., Trávníček, P. M., Marsch, E., Fazakerley, A. N., and Scime, E. F., J. Geophys. Res. **114**, 5104 (2009)

Suzuki, S. and Dulk, G. A., in *Solar Radio Physics*, Ed. D. J. McLean & N. R. Labrum, Cambridge University Press, Cambridge (1985)

Thejappa, G., Goldstein, M. L., MacDowall, R. J., Papadopoulos, K., and Stone, R. G., J. Geophys. Res., **104**, 28279 (1999)

Tu, C. Y., and Marsch, E., Solar Phys., **171**, 363 (1997)

Vocks, C., Astrophys. J. **568**, 1017 (2002)

Vocks, C. and Marsch, E., Astrophys. J. **568**, 1030 (2002)

Vocks, C. and Mann, G., Astrophys. J. **593**, 1134 (2003)

Vocks, C. and Mann, G., Astron. Astrophys., **419**, 763 (2004)

Vocks, C., Salem, C. Lin, R. P., and Mann, G., Astrophys. J. **627**, 540 (2005)

Vocks, C. and Mann, G., Astron. Astrophys., **452**, 331 (2006)

Vocks, C., Mann, G., and Rausche, G., Astron. Astrophys., **480**, 527 (2008)

Vocks, C. and Mann, G., Astron. Astrophys. **502**, 325 (2009)

Vocks, C., Space Sci. Rev., accepted, doi: 10.1007/s11214-011-9749-0 (2011)

Warmuth, A., Mann, G., in *Space Weather*, Ed. K. Scherer, H. Fichtner, B. Heber, U. Mall, Lecture Notes in Physics **656**, 49, Springer, Berlin (2004)

Warmuth, A., Mann, G., and Aurass, H., Astron. Astrophys. **494**, 677, (2009)

Wu, C. S. and Freund, H. P., Astrophys. J., **213**, 575 (1977)

Wu, C. S. and Lee, L. C., Astrophys. J., **230**, 621 (1979)

Xiao, F., Thorne, R. M., Gurnett, D. A., and Williams, D. J., Geophys. Res. Lett., **30**, SSC 3-1, doi: 10.1029/2003GL017123 (2003)

Yang, H. Q. and Przekwas, A. J., J. Comp. Phys., **102**, 139 (1992)

Zouganelis, I., Maksimovic, M., Meyer-Vernet, N., Lamy, H., and Issauthier, K., Astrophys. J. **606**, 542 (2004)

# Acknowledgements

I would like to thank the directors of the Leibniz-Institut für Astrophysik Potsdam (AIP), Prof. M. Steinmetz and Prof. K. G. Strassmeier, for giving me the opportunity to prepare the work presented in this thesis, and for bridging gaps between the funding periods of different projects.

I would like to express my special gratitude to Prof. G. Mann for his strong support, his continued interest in my work, and for many fruitful discussions, without which writing this thesis would not have been possible.

I thank all current and former colleagues at the solar radio astronomy group at AIP, i.e. Dr. H. Aurass, Dr. S. Braune, F. Breitling, Dr. H.-T. Claßen, Dr. A. Klassen, D. Lehmann, Dr. R. Miteva, Dr. H. Önel, Dr. G. Rausche, Dr. J. Rendtel, and Dr. A. Warmuth for many contributions to my work.

Finally, I would like to thank all my friends at AIP, of whom I cannot provide a comprehensive list here, for a great work environment.

The financial support by Deutsches Zentrum für Luft- und Raumfahrt (DLR), the Max-Planck-Institute for Solar System Research, the Deutsche Forschungsgemeinschaft (DFG), and the Land Brandenburg during my postdoc time is gratefully acknowledged.